GROWTH, FABRICATION, AND CHARACTERIZATION OF III-NITRIDE SEMICONDUCTORS FOR HIGH-PERFORMANCE ULTRAVIOLET AVALANCHE PHOTODIODES BY METALORGANIC CHEMICAL VAPOR DEPOSITION

A Ph.D Dissertation
Presented to
The Academic Faculty

by

Mi-Hee Ji

In Partial Fulfillment
of the Requirements for the Degree
Doctor of Philosophy in the
School of Electrical and Computer Engineering

Georgia Institute of Technology
May 2018

GROWTH, FABRICATION, AND CHARACTERIZATION OF III-NITRIDE SEMICONDUCTORS FOR HIGH-PERFORMANCE ULTRAVIOLET AVALANCHE PHOTODIODES BY METALORGANIC CHEMICAL VAPOR DEPOSITION

Approved by:

Dr. Russell D. Dupuis, Advisor
School of Electrical and Computer Engineering
Georgia Institute of Technology

Dr. Rao R. Tummala
School of Electrical and Computer Engineering
Georgia Institute of Technology

Dr. Shyh-Chiang Shen
School of Electrical and Computer Engineering
Georgia Institute of Technology

Dr. Jae-Hyun Ryou
Department of Mechanical Engineering
University of Houston

Dr. P. Douglas Yoder
School of Electrical and Computer Engineering
Georgia Institute of Technology

Date Approved: March 23, 2018

ACKNOWLEDGEMENTS

I would like to express my deepest gratitude to all those who have helped me along the way in making this dissertation possible. First and foremost, I would to thank my advisor, Professor Russell D. Dupuis, for his guidance and for providing me with the valuable opportunity to perform this research. I am very proud of being one of his students and I am honored to have studied in his Advance Materials and Devices Group (AMDG) at Georgia Institute of Technology.

I would also like to thank to my committee members, Dr. Shyh-Chiang Shen, Dr. P. Douglas Yoder, Dr. Rao R. Tummla, Dr. Jae-Hyun Ryou, for the valuable comments and suggestions. I have learned much from them, and it was a great honor to have your names on my dissertation.

I am also grateful to my past and current colleagues in AMDG: Dr. Zachery Lochner, Dr. Jae-Hyun Ryou, Dr. Jeomoh Kim, Dr. Xiaohang Li, Dr. Theeradetch Detchprohm, Kevin Liu, Hoon Jeong, Marzieh Bakhtiary Noodeh for their help and cooperation in this research. I was lucky to have the members of Dr. Shen's research group including Dr. Yun Zhang, Dr. Yi-Che Lee, Dr. Tsung-Ting Kao, Dr. Chen-Yin Wang, Oliver Moreno. I would especially like to thank to Dr. Theeradetch Detchprohm and Dr. Jeomoh Kim for being great mentors for many years of personal, professional, and technical guidance.

Finally, I would like to thank my entire family for their everlasting love and support. Especially, I will never be able to thank my parents enough for providing me

with everything I needed to be the person I am today. I am grateful to my loving husband, Young Seuk Kim, who has always inspired and encouraged me with patience and unconditional support.

TABLE OF CONTENTS

LIST OF TABLES

LIST OF FIGURES

CHAPTER 1. INTRODUCTION

III-nitride compound semiconductors, including gallium nitride (GaN), aluminum nitride (AlN), indium nitride (InN), their ternary and quaternary alloys, have recently attracted great attention as the most promising electronics and optoelectronic devices. By adjusting the direct bandgap energy of III-nitride materials, they can cover a wide spectral range from infrared (1772 nm) to deep-ultraviolet (200 nm) and are useful for optoelectronic devices such as light-emitting diodes (LEDs), photodiodes (PDs), and avalanche photodiodes (APDs). Unlike conventional semiconductors such as silicon (Si), indium phosphide (InP), and arsenide (GaAs), the wide and direct bandgap III-nitride materials provide high breakdown field, high electron drift velocity, and high thermal conductivity as well as structure, chemical, thermal stability, which make III-nitride materials suitable for device operating at high temperature and in harsh environments. Thanks to these advantageous properties, III-nitride-based semiconductors are well-suited for numerous applications in solid-state lighting, military systems, high-density optical storage, imaging systems, medical equipment, and space research.

This dissertation will discuss III-nitride-based ultraviolet avalanche photodiodes (UV-APDs): $Al_{0.05}Ga_{0.95}N$ *p-i-n* UV-APDs with high avalanche gain, 4×4 GaN *p-i-n* UV-APDs arrays with large detection area, GaN *p-i-p-i-n* separate absorption and multiplication (SAM) UV-APDs. Following a brief introduction to the III-nitride material properties and epitaxial growth system, the development history and motivations of UV photodiodes (PDs) and technical difficulties to achieve high-performance UV-APDs are summarized. Experimental approaches to solve these technical challenges will then be

discussed, including the results obtained. Finally, the summary of work completed will be proposed.

1.1 III-nitride Materials Properties

The common crystal structure of III-nitride materials can exist three different crystallographic phases of wurtzite, zinc-blende, and rock-salt structures [1]. Recently, the growth of metastable zinc-blende structure has been reported because of their advantageous properties of higher carrier mobility and easier cleaving for laser diodes (LDs) processing [2, 3]. However, the (001) crystal planes of cubic substrates such as Si, MgO, and GaAs were used to stabilize and grow thin films of the zinc-blende structure. Also, the rock-salt structure can only remain stable at very high pressures. Therefore, under ambient conditions, most III-nitride materials have a wurtzite structure because of its higher thermodynamic stability than the zinc-blende or rock-salt structures.

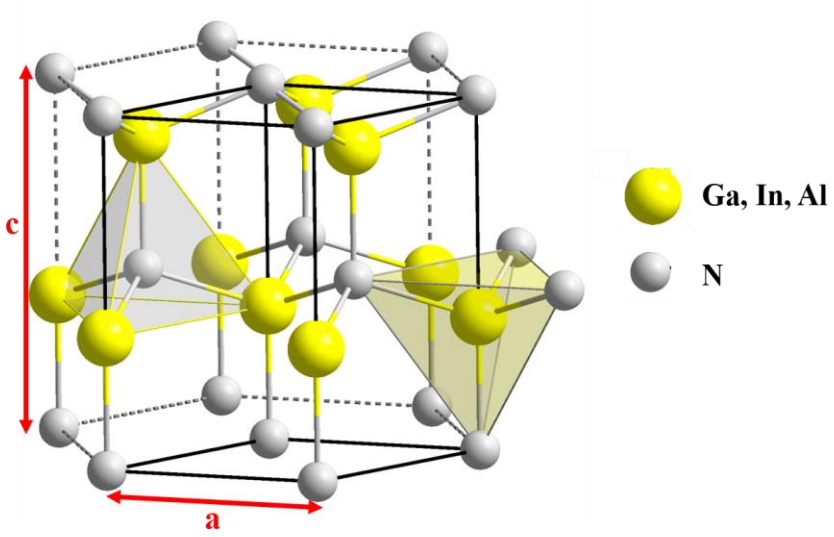

Figure 1.1 The unit cell of the hexagonal wurtzite structure of III-nitride semiconductors.

The wurtzite structure of III-nitride materials consists of two interpenetrating hexagonal close-packed (HCP) sublattices, which contain six atoms of each type, offset along the *c*-axis by 3/8 of the cell height. The wurtzite structure has a hexagonal unit cell and thus two lattice constants, *a* and *c*, as shown in Figure 1.1. For the ideal wurtzite structure, the lattice parameters are *c/a*=1.633. However, due to the electronegativity difference between the Group III and Group V atoms, the *c/a* ratio for AlN, GaN, and InN are 1.600, 1.626, and 1.616, respectively. The differences in the electronegativity create a dipole, resulting in polarization charge along the *c*-axis. The space group for the wurtzite structure is $P6_3mc$ (C^4_{6v}). In addition, specific important parameters related to structural, electronic, optical, and thermal properties are listed in Table 1.1 and Table 1.2.

Table 1.1. Lattice constant values for wurtzite III-nitride semiconductors [1].

Binary alloy	*a* (Å)	*c* (Å)
InN	3.548	5.760
GaN	3.189	5.185
AlN	3.112	4.982

Table 1.2 Important material properties of binary III-nitride compound semiconductors [4].

Binary alloy	InN	AlN	GaN
Bandgap [eV]	0.6~0.7 (direct)	6.2 (direct)	3.39 (direct)
Crystal structure (stable phase)	wurtzite	wurtzite	wurtzite
Thermal expansion ($\Delta a/a$) [10^{-6}/K]	4	4.2	5.59
Thermal expansion ($\Delta c/c$) [10^{-6}/K]	3	5.3	3.17
Thermal conductivity (κ) [W/cm·K]	0.8±0.2	2	1.3
Refractive index	2.93	2.15±0.05	2.33

The strong and large ionic bonding component in III-nitride materials are created by nitrogen atoms that attribute to different lattice constants and bandgap energies. The bonding energy of GaN, AlN, and InN are 8.96 eV, 11.52 eV, and 7.72 eV, respectively. Therefore, III-nitride semiconductors are a promising candidate for photonic- and electronic applications, operating in high-power and high-temperature environments because of the tightly bonded structures with their strong bonding energies.

One of the notable properties of the wurtzite III-nitride alloys is the large- and direct-bandgap. In general, the photons with an energy greater than the bandgap energy

are absorbed by semiconductor materials, creating an electron-hole pair (EHP) while the photons with an energy smaller than the bandgap energy are not absorbed. In the case of the photons with the energy less than the bandgap, the materials are transparent. The bandgap energy (E_g) is directly related to the wavelength (λ) of the energy of a photon according to the equation:

$$E_g = \frac{h \cdot c}{\lambda} \tag{1.1}$$

where h is the Plank's constant and c is the speed of the light in free space.

The bandgap energy (E_g) for InN, GaN, and AlN are 0.78±0.05 eV, 3.52±0.1 eV, and 6.1±0.1 eV, respectively, at room temperature [1, 5, 6]. As shown in Figure 1.2, therefore, the bandgap energy can cover from the deep-UV region (λ=200 nm; E_g: 6.2 eV) to the infrared region (λ=1770 nm; E_g: 0.7 eV) by adjusting the composition of each binary component in the AlGaN, InGaN, AlInN, ternary or AlInGaN quaternary alloys. The bandgap energy of ternary alloys can be determined by the composition and bandgap energies of each alloy using Vegard's law.

$$E_{g,Al_x Ga_{1-x}N}(x) = x \cdot E_{g,AlN} + (1-x) \cdot E_{g,GaN} + bx(1-x) \tag{1.2}$$

$$a_{Al_x Ga_{1-x}N}(x) = x \cdot a_{AlN} + (1-x) \cdot a_{GaN} + bx(1-x) \tag{1.3}$$

where E_g is the bandgap energy, x is the % alloy composition, a is the lattice parameter, and b is the bowing parameter specific to each compound and obtained by experimental methods [7, 8].

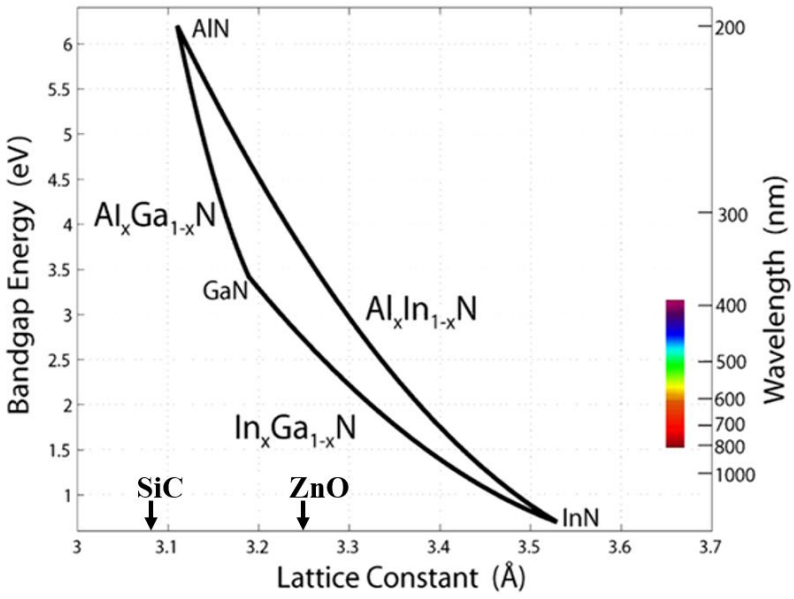

Figure 1.2 Bandgap energy vs. lattice constant of III-nitride materials.

1.2 Metalorganic Chemical Vapor Deposition

The metalorganic chemical vapor deposition (MOCVD) process for the growth of III-nitride compound semiconductor materials was pioneered in 1968 by Manasevit who successfully demonstrated the epitaxial of GaAs [9]. The AlGaAs/GaAs solar cells and quantum-well injection layer as the first practical devices were grown using MOCVD by Dupuis *et al.*, in 1977 and 1978 [10, 11]. The breakthrough was established in the late

1980's by Ammono *et al.*, who grew the first high-quality GaN thin films by MOCVD using AlN buffer layer [12] and successfully achieved Mg-doped GaN by the low-energy electron beam irradiation (LEEBI) treatment [13]. Recently, the metalorganic chemical vapor deposition (MOCVD) technique have been widely employed to produce III-nitride compound semiconductor devices such as laser diodes (LDs), light emitting diodes (LEDs), avalanche photodiodes (APDs), high-electron-mobility transistors (HEMTs), and solar cells, due to its versatility.

In the MOCVD process, two or more materials in the gaseous phase are introduced into a chamber and pyrolyzed in an H_2 or N_2 ambient to chemically react with each other and form a solid material deposited on the heated wafer surface. The metalorganic (or alkyl) precursors that are either solid or liquid form at 300K are contained in an all-welded stainless-steel container, commonly called "bubbler", and carrier gas is passed (or bubbled) through the liquid (or over the solid), transporting MO precursor molecules into the growth chamber. For the MOCVD growth of III-nitride materials, trimethylgallium ($Ga(CH_3)_3$, TMGa), triethylgallium ($Ga(C_2H_5)_3$, TEGa), trimethylaluminum ($Al(CH_3)_3$, TMAl), and trimethylindium ($In(CH_3)_3$, TMIn) are commonly used for Group III precursors and ammonia (NH_3) is used for Group V hydride precursors. Inert carrier gases, hydrogen (H_2) and nitrogen (N_2), are used to mix with the Group III and Group V precursors and carry the precursors to the reaction chamber. Diluted silane (SiH_4) and bis-cyclopentadienyl magnesium ($Mg(C_5H_5)_2$, Cp_2Mg) are used as *n*- and *p*-type dopant precursors, respectively. The chemical reaction employing metalorganic and hydride precursors to form III-nitride epitaxial layer can be represented by the following equation:

$$R_3M\ (g) + EH_3\ (g) \rightarrow ME\ (s) + 3RH \uparrow (g) \quad (1.4)$$

where R is the alkyl group of CH_3 or C_2H_5, M is the Group III metal atom such as Ga, Al, or In, E is the Group V atom such as N, and H is hydrogen. The chemical reactions occurring in the MOCVD growth process are extremely complicated and include a series of gas-phase and surface reactions, which can be categorized into four processes: gas input, pyrolysis, diffusion, and surface reaction. Then, any by-products formed during the epitaxial growth are pumped away with the carrier gases.

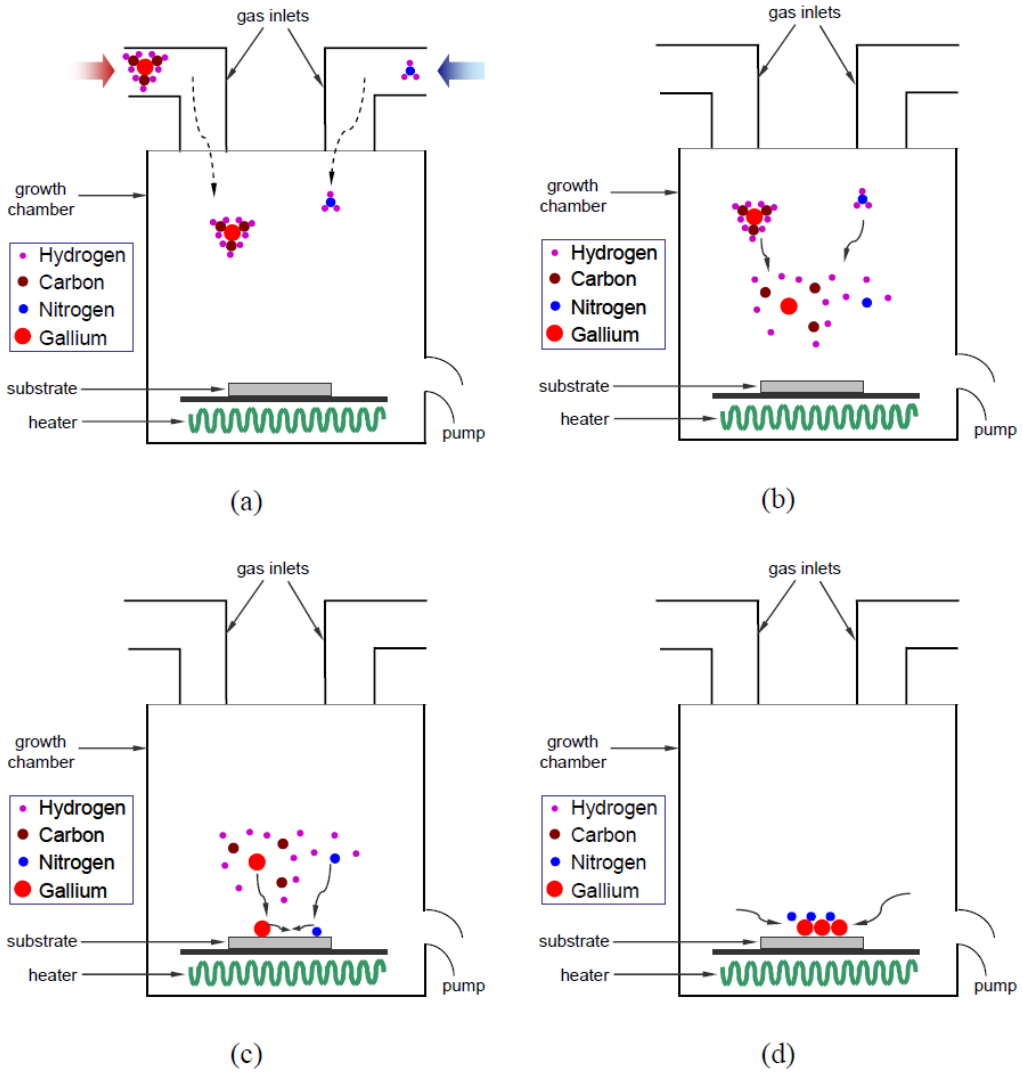

Figure 1.3 Schematic illustration of MOCVD epitaxial growth process (a) gas input (b) pyrolysis (c) diffusion (d) surface reaction.

The MOCVD reactor system used in this study is an Aixtron 6×2” rotating disk reactor with close-coupled showerhead (CCS^{TM}) geometry. The CCS technology can provide growth uniformity, resulting from the complete intermixed uniform distribution of gas phases. The temperature gradients within the chamber are controlled by the three-

zone heater system for maximizing temperature uniformity. A basic diagram of this MOCVD system is presented in Figure 1.4.

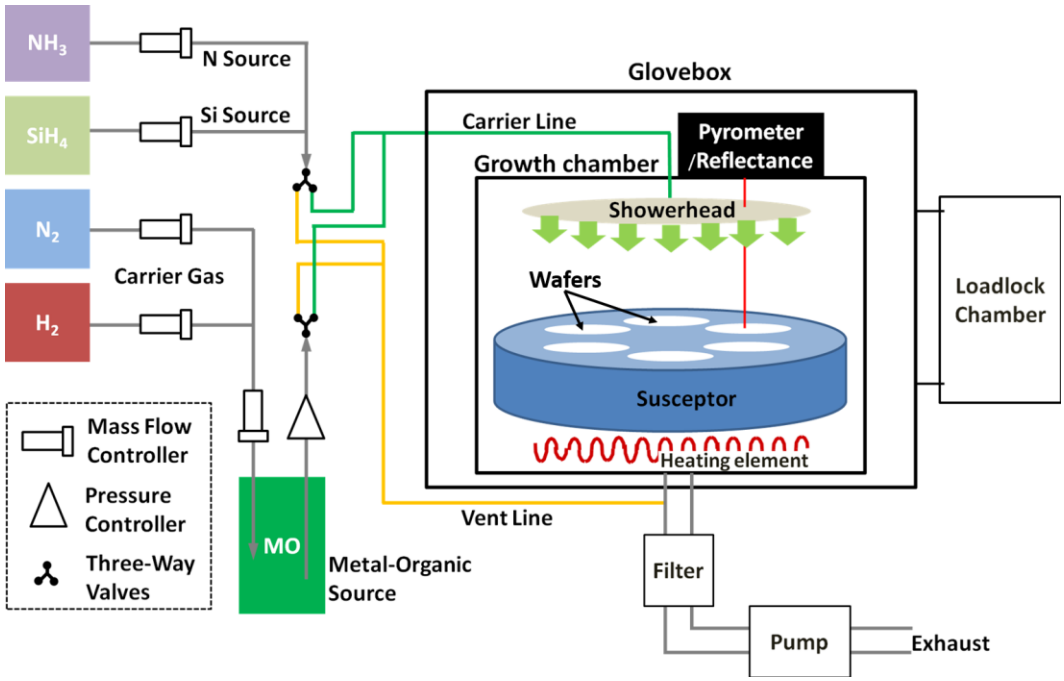

Figure 1.4 Basic diagram of the MOCVD reactor system.

1.3 Motivations for III-nitride Avalanche Photodiodes

The ultraviolet (UV) spectral region is commonly classified by electromagnetic radiation with a wavelength range between λ~10 nm (X-rays) and λ~400 nm (violet), and it can be divided into three spectral bands: UVA for λ=400 nm~320 nm, UVB for λ=320 nm~280 nm, UVC for λ=280 nm~shorter. The Earth's atmosphere strongly absorbs UV radiation which directly comes from the Sun. However, the ozone layer and gases, such as oxygen and CO_2, strongly absorb UV photons with a wavelength shorter than 290 nm. As the

result of this absorption, there is no significant energy at the Earth's surface in the spectral range shorter than 290 nm, contributed by the Sun. Thus, UV photodetectors that respond in this region are called solar-blind photodetectors. In a similar way, UV photodetectors with a spectral response shorter than 400 nm, which cannot detect visible light, are defined as visible-blind photodetectors.

The detection of UV radiation has become of great importance in numerous applications, including military systems, flame sensors, bio-agent detection, imaging systems, optical communication systems, and space research [14, 15, 16, 17, 18, 19, 20]. Conventionally, photomultiplier tubes (PMTs) and UV-enhanced Si photodetectors are used for these detection applications requiring fast response, high sensitivity, and low noise. Even though PMTs offer high sensitivity in UV detection with high optical gain > 10^6, they are required to operate at the high voltage of 1-2 kV, and the photocathode must be cooled down to reduce the dark current [21, 22]. In addition, expensive optical filters must be needed to block visible solar radiation which results in high background noise, making them costly, bulky, and fragile. Compared to PMTs, UV-enhanced Si photodetectors with narrow bandgap energy (1.12 eV) offer several advantages that they can be fabricated into very small or large devices, and integrated with other Si-based devices using mature and advanced Si processing technology. However, they have high dark current and reliability issues caused by the degradation at Si/SiO_2 interface after long-term exposure and also require expensive filters for visible- and solar-blind operation like PMTs. The commercial UV-enhanced Si avalanche photodiode (APD) by Hamamatsu shows a gain of 50 at λ=420 nm with spectral response range from λ=320 nm to λ=1000 nm [23]. As a replacement for conventional PMTs or Si APDs, UV

photodiodes (PDs) and avalanche photodiodes (APDs) based on wide-bandgap (WBG) semiconductors such as III-nitrides or SiC have generated a lot of interest for the reliable UV detectors because of their inherent properties of enhanced radiation hardness, intrinsic visible-blindness, thermal and chemical stability.

1.3.1 SiC Avalanche Photodiodes

Early studies of SiC-based APDs have been reported demonstrating low dark current, low multiplication noise and good visible blind performance owing to the relative maturity of this material and widely disparate ionization coefficients for electrons and holes [24, 25, 26, 27]. The high-quality passivation layer that consists of a thin thermal oxide layer capped by 300 nm of plasma-enhanced chemical vapor deposition SiO_2 and available high-quality SiC substrates result in reduced leakage current from side wall as well as surface [28]. By applying a recessed-window structure, 4H-SiC APDs with a low dark current of 0.18 $\mu A/cm^2$, maximum avalanche gain over 10^6, and a peak responsivity of 136 mA/W at λ=262 nm has been achieved by Prof. Campbell's group at the University of Virginia [29]. Recently, 4H-SiC separated absorption charge multiplication (SACM) UV-APDs with a low breakdown voltage and 4H-SiC *p-i-n* UV-APDs with *p*-layer formed by Al implantation have been reported to improve the performance of SiC APDs for UV detection [30, 31]. For detection in the solar-blind region, however, external filters should be required because of the indirect nature of the SiC bandgap.

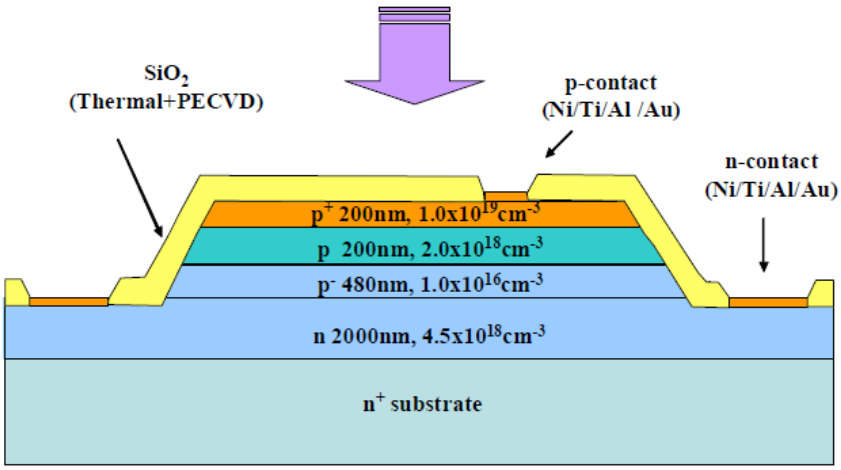

Figure 1.5 Schematic cross section of a typical SiC-based *p-i-n* APD structure [32].

1.3.2 III-nitride Photodiodes

The most important UV semiconductor photodetectors based on III-nitride materials are categorized into four fundamental modes: photoconductors, metal-semiconductor-metal (MSM) detectors, Schottky barrier diodes, and *p-n* photodiodes. As shown in Figure 1.6 (a), photoconductors have the simplest form among the III-nitride photodetectors and comprise an absorbing semiconductor layer with two ohmic contacts at each end. The photogenerated electrons and holes are collected by opposite contacts. The first GaN UV photoconductors grown on a sapphire substrate using an AlN buffer layer, which exhibited a responsivity of 2,000 A/W at λ=365 nm under a 5 V bias, was demonstrated by Khan *et al.* [33]. The development of $Al_xGa_{1-x}N$ photoconductors with a high responsivity (>100 A/W) was also reported [34 , 35]. Especially, persistent photoconductivity that the conductivity continues for minutes to hours after the removal of optical excitation has been reported for all of the III-nitride-based photoconductors

[36, 37, 38, 39]. Because of the combination of strong persistent photoconductivity, sublinear power response, and low UV/visible rejection, the use of III-nitride photoconductors is limited for many applications.

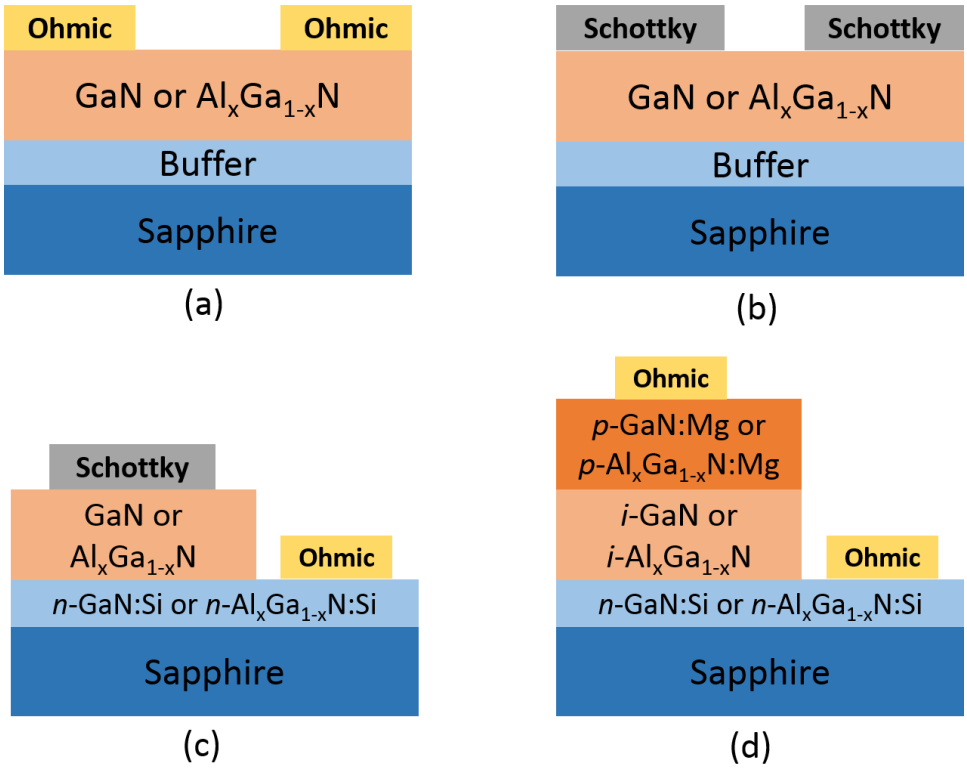

Figure 1.6 Schematic structures of (a) photoconductors, (b) MSM photodetectors, (c) Schottky barrier photodiodes, and (d) PIN photodiodes.

Schottky-barrier-based photodiodes such as Schottky barrier (metal-semiconductor) and metal-semiconductor-metal (MSM) photodiodes offer the attractive advantages of fast response speed and large bandwidth capability [40, 41]. Figure 1.6 (b)

shows the schematic structure of an MSM PD that is made by forming two interdigitated Schottky-barrier contact on the semiconductor surface. And, as shown in Figure 1.6 (c), a Schottky barrier PD is made by forming a Schottky-barrier contact on the surface of the semiconductor absorbing layer. The ohmic contact is formed on the same absorbing layer where the Schottky-barrier contact is formed or on a conduction layer underneath the absorbing layer. In particular, MSM-PDs present better performance over other photovoltaic detectors, including fabrication simplicity, suitability for integration with FET preamplifier circuits, no *p*-type doping and mesa etching requirement, and low capacitance, that allow them to be used for solar-blind photodetectors. However, the potential limiting factors for MSM-PDs are the shadowing of the optical active region by interdigitated electrodes and the relatively large dark current that exist for the performance of these devices. In recent advances, MSM-PDs with a reduced dark current density of $\sim 1.4\times10^{-9}$ A/cm^2 and an avalanche gain of more than 1,100 under 365 nm UV illumination have been reported by F. Xie *et al*. [42]. Although back-illuminated and semi-transparent Schottky contacts were employed to overcome light blocking issue [43, 44, 45, 46], it still makes them less suitable for high-sensitivity UV detection.

The epitaxial structure of *p*-*i*-*n* photodiodes consists of a relatively thick intrinsic layer sandwiched between heavily doped *n*- and *p*-type layers with ohmic contacts formed on the surface of *n*- and *p*-type layers, as shown in Figure 1.6 (d). Owing to the APD's attractive performance characteristics of lower dark current density, higher responsivity, higher detectivity, higher internal gain, and radiation-hardened, they have become useful for a wide range of applications. Moreover, as shown in Figure 1.7, APDs utilize the impact ionization process to create a number of photogenerated electron-hole

pairs, a process that offers larger internal gain and higher detection sensitivity than that of *p-n* photodiodes.

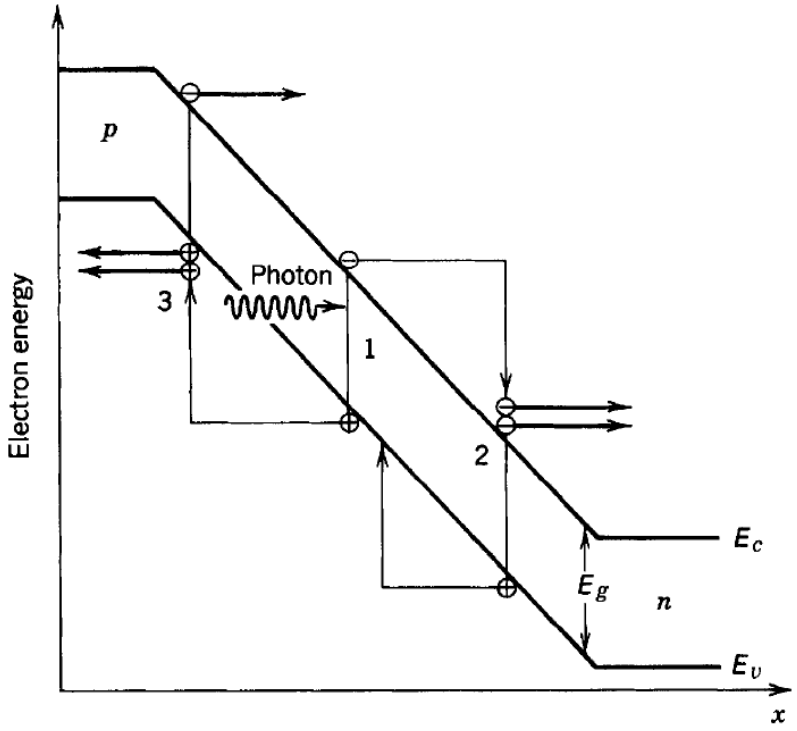

Figure 1.7 Schematic representation of the multiplication process in an APD [47].

The common technical challenges involved in improved material quality, device structure design, fabrication process development including mesa etching and the passivation layer to achieve high-performance III-nitride-based UV-APDs. However, the realization of high-quality of III-nitride-based *p-i-n* UV-APDs has been hampered by high densities of defects and dislocations with defect density of 10^8~10^9 cm^{-2} originating from heteroepitaxial layers grown on lattice-mismatched substrates such as sapphire or

SiC, resulting in larger dark current density, device size limitations, low yield, and non-uniformity of devices in an array format [48]. The lattice constant mismatch between sapphire and GaN substrate is significant at around 14%. These high defects can lead to a premature microplasma breakdown before the electric field in the depletion region can reach the bulk avalanche breakdown field [49, 85]. Also, for the conventional front-contact device structures, *n*-type layer plays an important role in reducing the current crowding towards the edge of the mesa because of etching damage, and it may potentially lead to high leakage current and device failure by premature breakdown. Although a high doing and low resistivity in an *n*-type layer can be obtained relatively easily, achieving reasonable *p*-type doing in the III-nitride material system is still challenging because the activation energy of Mg acceptor in GaN is assumed to be ~160 meV and it increases with increasing Al composition [50, 51, 52, 53].

Because of the relative ease of growth, most of the early (Al)GaN-based APDs were designed for front-illuminated operation including *p*-*i*-*n* photodiodes [54], *p*-*i*-*n* APDs in linear operation [55, 56], separate absorption and multiplication (SAM) APDs [57]. For the front-illumination devices, a thick GaN buffer layer or *n*-type layer can be grown on a sapphire substrate, which helps to reduce the number of dislocation densities of the devices. Therefore, improvement of the material quality of device structures plays an important role to enhance the performance of III-nitride UV-APDs, especially for arrays.

Recently, to address these technological challenges, (Al)GaN-based UV-APDs grown on high-quality bulk or "free-standing" III-nitride substrates with low dislocation density less than 10^6 cm^{-2} have been successfully demonstrated with not only extremely

low dark current and high avalanche gain [58, 59, 60, 61, 62] but also Geiger-mode operation [63, 64, 65]. Moreover, the back-illuminated (Al)GaN *p-i-n* UV-APDs [66, 67] and separate absorption and multiplication (SAM) UV-APDs [68, 69, 70, 71, 72, 73, 74, 75] have been investigated for achieving high maximum gain and low multiplication noise, due to higher hole ionization coefficient [76, 77]. However, native substrates or thick GaN/sapphire templates to grow UV-APD structure with superior crystalline quality cannot be used in the back-illumination without additional processing steps due to strong UV-light absorption by thick *n*-type GaN layer or native substrates.

1.4 Scope of this Dissertation

This thesis will discuss the MOCVD growth, fabrication, and device characterization of III-nitride-based ultraviolet avalanche photodiodes (UV-APDs). In Chapter 1, a brief introduction to the III-nitride material properties and epitaxial growth system, the development history of UV photodiodes (PDs), the motivations for III-nitride-based UV-APDs, and technical difficulties to achieve high-performance UV-APDs are summarized. In Chapter 2, the characterization methods of epitaxial layers and devices used in this study will be presented in detail. Chapter 3 reports on the growth, fabrication, and device characterization of $Al_{0.05}Ga_{0.95}N$ *p-i-n* UV-APDs grown on free-standing GaN and sapphire substrates. In Chapter 4, the GaN *p-i-n* 4×4 UV-APD arrays with large detection area will be reported. Chapter 5 focused on the demonstration of front-illuminated GaN *p-i-p-i-n* separation absorption and multiplication (SAM) UV-

APDs with large detection areas by employing impact-ionization engineering. Finally, the summary of work performed in this dissertation will be provided in Chapter 6.

CHAPTER 2. MATERIAL AND DEVICE CHARACTERIZATION

2.1 Introduction

Several analysis and characterization techniques are utilized to measure the electrical- and optical properties of the devices and quality of epitaxial layer structure in the research on III-nitride semiconductor materials. This chapter will describe material characterization techniques of X-ray diffraction, photoluminescence, atomic force microscopy, scanning electron microscopy, and device characterization techniques of Hall-effect measurement, responsivity, transmission line measurement.

2.2 Material Characterizations

2.2.1 X-ray Diffraction

The X-ray diffraction (XRD) is a powerful *ex-situ* analytical techniques for the characterization of crystalline materials. The XRD measurement is commonly used to determine the structural properties such as crystalline perfection, alloy composition, uniformity, the thickness of thin films or multilayers, and built-in strain and relaxation because of the advantages of convenient and non-destructive characterization [78]. The fundamental principle of XRD is based on Bragg's law:

$$n\lambda = 2d_{hkl}\sin\theta_B \tag{2.1}$$

where n is an integer determined by the order given, λ is the wavelength of X-rays, d_{hkl} is the spacing between the planes in the atomic lattice, and θ_B is the Bragg's angle. For a cubic crystal ($a=b=c$), the lattice spacing of the plane ($h\ k\ l$) is described by the following equation:

$$\frac{1}{d_{hkl}^2} = \frac{h^2 + k^2 + l^2}{a^2} \tag{2.2}$$

For a hexagonal lattice, the lattice spacing is expressed by the following equation:

$$\frac{1}{d_{hkl}^2} = \frac{4}{3}\left(\frac{h^2 + k^2 + l^2}{a^2}\right) + \frac{l^2}{c^2} \tag{2.3}$$

where a and c are lattice constants of the plane, and h, k, and l are the Miller indices of the plane of interest.

The rocking curves (ω-scan) are primarily used XRD scan to determine the relative crystalline quality of different samples by comparing full width half maximum (FWHM) or linewidth of this broadened peak. In the ω-scan, the detector is kept at a fixed angle with respect to the primary beam (2θ) while the sample is rotated or rocked across the ω axis, perpendicular to the sample surface as shown in Figure 2.1. The

limitation of the rocking curve is limited angular range of only ~1º so the information of large mismatched layers cannot be collected in a single scan. The large mismatched layer can be characterized by the alternative technique of the *ω-2θ* scan. The detector moves at a twice angular rotation rate of the sample (*ω*) so that the measured diffraction angle always remains *2θ* with respect to the incident beam angle. Thus, diffraction peaks are narrower and do not overlap between layers in the diffraction spectrum.

All XRD results presented in this dissertation are performed by using Philips X'Pert® MRD (Material Research Diffractometer) high-resolution (0.0001°) X-ray diffractometer as shown in Figure 2.1.

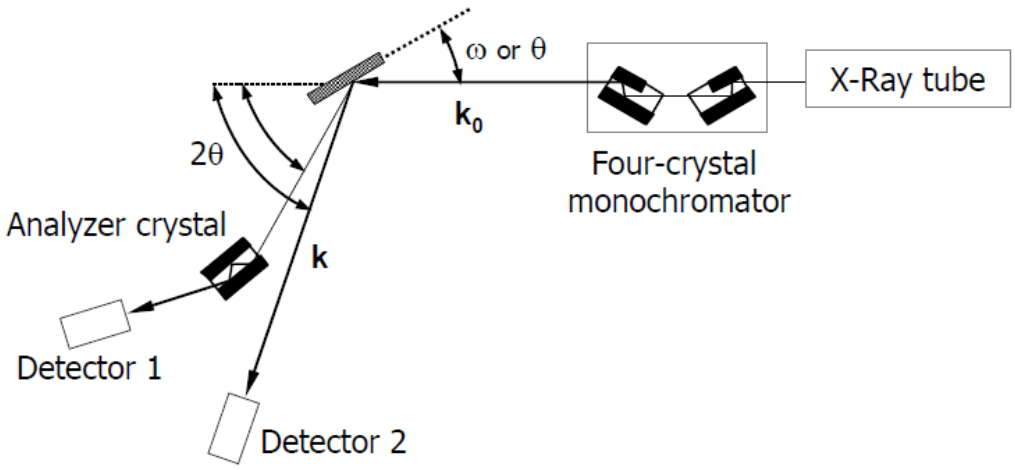

Figure 2.1 Schematic diagram of a typical configuration of an X-ray diffractometer.

2.2.2 Photoluminescence

Photoluminescence (PL) is the spontaneous emission spectrum of light from a direct bandgap semiconductor material under optical excitation by a laser. The PL

measurement system is a powerful tool to determine the band gap energy of material and material quality, allowing contactless and non-destructive characterization. When the photon energy of incident beam higher than the bandgap energy of the material is absorbed, the electron-hole pairs are created and recombined via radiative recombination process by emitting light at the energy of the bandgap. The emitted photons are collected and analyzed by detectors, simple relationship between the energy of a photon and the corresponding wavelength of that photon is described by the following equation.

$$E_g = h\nu = \frac{hc}{\lambda} = \frac{1249.8}{\lambda} \tag{2.4}$$

where E_g is the bandgap energy of the semiconductor materials in eV, h is Planck's constant, ν is the frequency of light, c is the speed of light, and λ is the wavelength in nm. In addition to the determination of the bandgap energy of semiconductor materials, the PL spectrum analysis can lead to evaluate material quality related to specific defects and impurities.

The Accent Optical Technologies RPM-2000 system equipped with the 266 nm Q-switched Nd:YAG laser as an excitation source is used for measuring photoluminescence characteristics in this study.

2.2.3 Atomic Force Microscopy

Atomic force microscopy (AFM), which was first developed in 1986 by Binning, Quate, and Gerber [79], is useful non-destructive measurement technique to provide three-dimensional surface topographies, growth mode, and defect density as a type of scanning probe microscopy (SPM). Figure 2.2 shows a schematic drawing of the simple operation of the AFM measurement system. As shown in Figure 2.2, the AFM consists of a sharp tip mounted at the end of a flexible cantilever that scans over the sample surface by raster scanning. As the tip approaches close proximity to the surface to be analyzed, the attractive or repulsive forces between the tip and the surface can be detected by measuring the deflection of the cantilever.

There are three AFM basic operating modes that are contact mode, non-contact mode, and tapping mode. In contact mode, the overall forces are repulsive between the tip and the surface, and the deflection of the cantilever is kept constant. The tip is also dragged across the sample surface potentially resulting in surface damages, tip breakage or distorted image data influenced by frictional and adhesive forces. In contrast, the overall forces between the tip and the sample are attractive in the non-contact mode. The tip does not touch the sample surface and is oscillated at the resonance frequency, and the amplitude of the oscillation is kept constant. Therefore, low resolution image is obtained by non-contact mode and it can be hampered by the contaminant layer, which interferes with the oscillation of the cantilever. The tapping mode takes advantage of contact mode and non-contact mode described above. The tapping mode provides higher resolution minimizing sample damages, eliminating frictional forces by intermittently touching or tapping the surface, and oscillating with sufficient amplitude.

The AFM measurement system used in this study is Veeco Dimension 3100 scanning probe microscope, operating in the tapping mode.

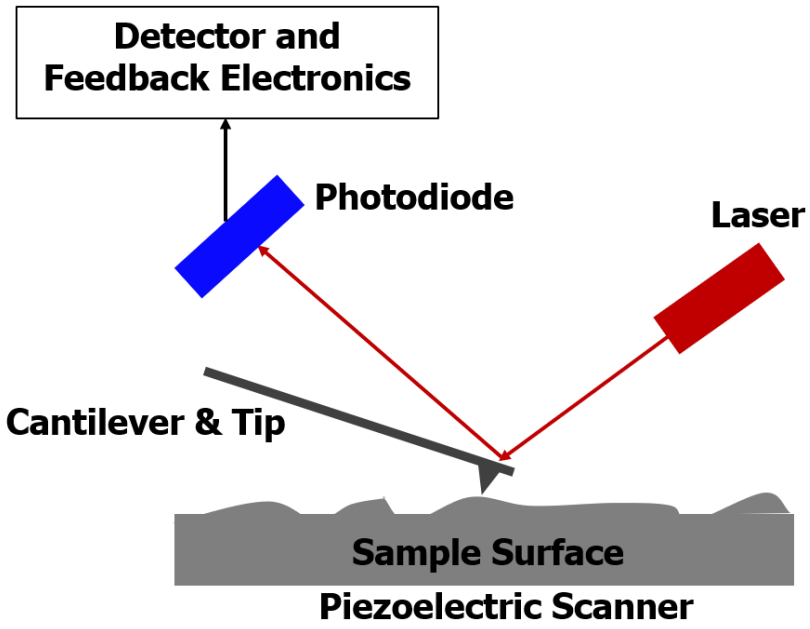

Figure 2.2 Schematic diagram of atomic force microscope.

2.2.4 Scanning Electron Microscopy

Scanning electron microscopy (SEM) is most widely used to observe surface topography, morphology, composition, and fabricated devices, which used accelerated electrons as the source of illumination radiation. As shown in Figure 2.3, the electron source located at the top of an SEM column that generates a beam of electrons. The beam accelerated by the anode is focused as a fine point on the sample surface by the lens and scanned in a rectangular raster pattern across the sample surface. When the sample

surface is bombarded by fast-moving primary electrons with high energy, secondary electrons, backscattered electrons, and X-rays are released from the sample surface. The emitted secondary electrons with low energy are collected by secondary electron detectors and converted into a various signal that is transferred to the screen to produce high-resolution images of the sample. Over other electron microscopes such as transmission electron microscopy (TEM), SEM can characterize large and bulky samples without elaborate sample preparation steps. However, the electron microscopes must be utilized under the high vacuum to prevent electrical discharge from electron beams and to enable electrons to travel in straight lines.

The SEM images used in this study are taken from Hitachi S-4700 FE-SEM that is a cold field emission high-resolution SEM.

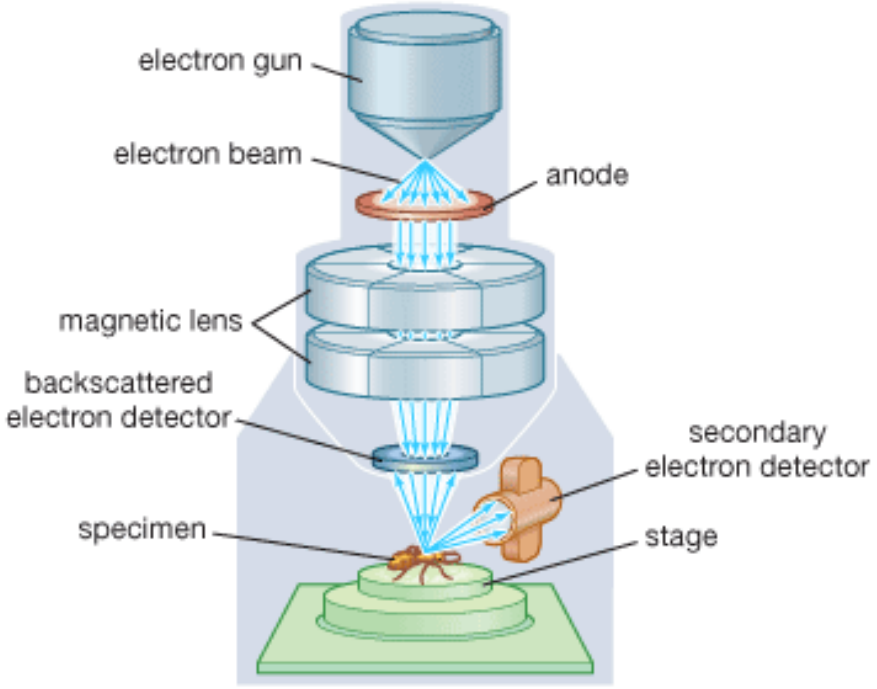

Figure 2.3 Schematic illustration of a scanning electron microscopy column [80].

2.3 Device Characterizations

2.3.1 Hall-Effect Measurement

The Hall-effect measurement, which was proposed by L. J. Van der Pauw in 1958 [81], is a simple characterization technique commonly used for determination of electrical properties of semiconductors such as the resistivity of the material, the mobility of the majority carrier, carrier type, and carrier concentration. To estimate the resistivity on an arbitrarily shaped sample from the Hall-effect measurement using van-der-Pauw model, the following conditions are required: 1) the contacts are at the boundary, 2) the contacts are negligibly small, and 3) the samples are uniformly doped and thick. An approximately 1×1 cm^2 square sample with indium eutectic and Ni/Ag/Ni/Au metal

stacks for *n*- and *p*-type contact layers, respectively, is prepared in this study, as shown in Figure 2.4.

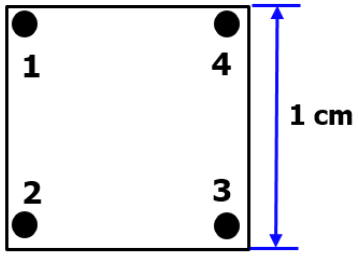

Figure 2.4 A typical hall sample; a variation on Van der Pauw Geometry.

According to van der Pauw method, the resistivity is given by

$$\rho = 2.2666t\left(\frac{V_{43}}{I_{12}} + \frac{V_{23}}{I_{14}}\right)F \tag{2.5}$$

where *t* is the sample thickness, *I* is the applied current, *V* is the measured voltage, and *F* is a correction factor based on sample symmetry (that are unity for perfect squares).

The Hall effect can be observed when an electrical current flows through a sample placed in a magnetic field, which produces a transverse voltage that is perpendicular to the electrical current and the magnetic field [82]. In case of van der Pauw Hall measurement, the Hall coefficient (R_H) is defined as

$$R_H = \frac{V_H \cdot t}{I \cdot B} \tag{2.6}$$

where V_H is the Hall voltage, t is the sample thickness, I is the applied current, and B is the applied magnetic field. Carrier concentration and mobility of the sample can be obtained from the Hall coefficient by following equations:

$$n = \frac{1}{-qR_H} \qquad p = \frac{1}{qR_H} \tag{2.7}$$

$$\mu = \frac{R_H}{\rho} \tag{2.8}$$

An Ecopia HMS-3000 Hall-effect measurement system is used in this study to perform the Hall-effect measurements.

2.3.2 Responsivity

The responsivity (R) and the quantum efficiency (η) are widely measured to evaluate the optical detector detection efficacy. The responsivity, which has a unit of amperes per watt (A/W), is defined as the ratio of photocurrent (I_{ph}) to optical power (W_{ph}) at a specified wavelength from the photodiode. The external quantum efficiency

(EQE) is the ratio of the number of carriers of photocurrent to the number of photons illuminated.

$$R = \frac{I_{ph}}{W_{ph}} \text{ [A/W]} \tag{2.9}$$

$$\eta = \frac{I_{ph}/q}{W_{ph}/h\nu} = \frac{I_{ph}}{W_{ph}} \cdot \frac{h\nu}{q} \tag{2.10}$$

where I_{ph} is the detected photocurrent of the photodiode, W_{ph} is the incident optical intensity, h is the Planck's constant, ν is the photon frequency, and q is the electric charge. In addition, the responsivity is related to the quantum efficiency depending on the wavelength the responsivity by

$$R = \frac{\eta q}{h\nu} = \frac{\eta q \lambda}{1.24} \tag{2.11}$$

where λ is the optical wavelength in μm.

Figure 2.5 shows a schematic drawing of the spectral response measurement system for this study [83]. To minimize the effect of environmental noise, an on-wafer DC probe station in a Faraday cage is used for the characterization of the fabricated UV-APDs. As shown in Figure 2.5, the Newport Apex Illuminator with a 150 W Oriel xenon lamp, which can provide light illumination from 200 nm to 2400 nm, is used as the light

source. An optical chopper system is attached to the output window on the Newport Apex Illuminator to modulate the illumination light with a frequency of 100 Hz. Then the modulated illumination light goes into the 1200 l/mm holographic grating (Newport 74162) in Cornerstone 260 ¼-m monochromator system to select single-wavelength optical signals. After the wavelength selection, the modulated single-wavelength light is coupled into UV fibers with 50- and 100-μm-diameter using a one-inch UV focus lens. The other end of the UV fiber is located on top of the fabricated UV-APDs under testing as close to the devices as possible. A calibrated Si-enhanced UV detector by Hamamatsu Inc. S2281-04 is used for optical power monitoring. An SRS 830 lock-in amplifier and an HP VEE program are used to detect the UV-APDs photocurrent and control the equipment for obtaining data, respectively. A Keithley Model 4200 Semiconductor Characterization System is used to apply constant voltages. The monochromator and the lock-in amplifier are controlled by a computer with a GPIB interface.

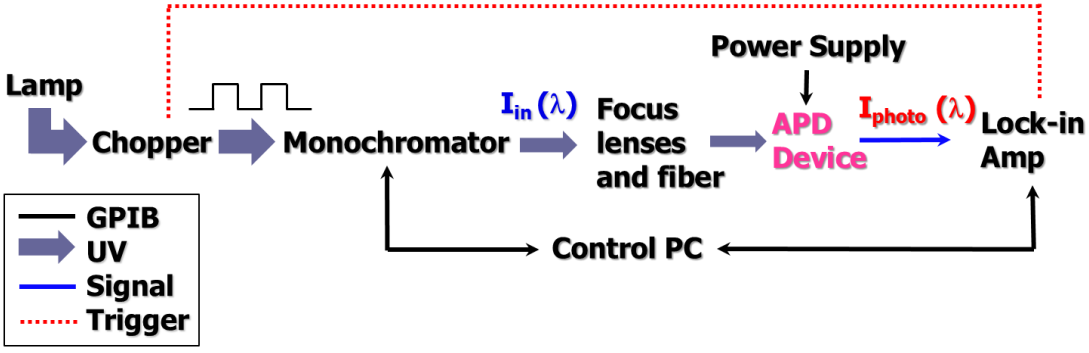

Figure 2.5 The schematics of the spectral response measurement system.

2.3.3 Transmission Line Measurement

The transmission-line measurement (TLM) is most commonly used to determine the contact resistance between metal and semiconductor as well as sheet resistance of the semiconductor layer because of its simplicity and accuracy. The TLM patterns require additional mesa etching to confine the current flow to the area between metal pads and to reduce the fringe effect. After the mesa definition, metal pads with various spacing is deposited on the top of the mesa as shown in Figure 2.6.

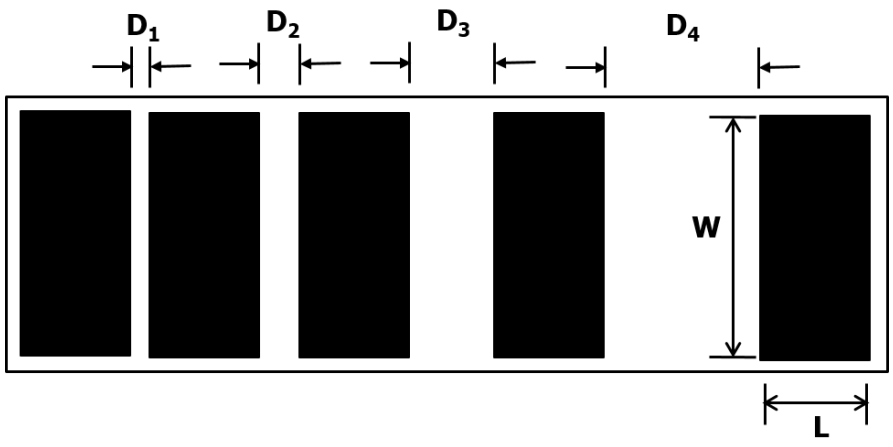

Figure 2.6 A typical transmission-line measurement (TLM) pattern showing the semiconductor mesa with metal pads.

The parameters used in the measurement and calculations are shown in Figure 2.6. D_x is the spacing between metal pads (μm), W is the width of a rectangular metal pad (μm), and L is the length of a rectangular metal pad (μm). As shown in Figure 2.7, the

contact resistance (R_c) and sheet resistance (R_s) can be extrapolated from the plot of measured resistance as a function of the spacing of metal pads.

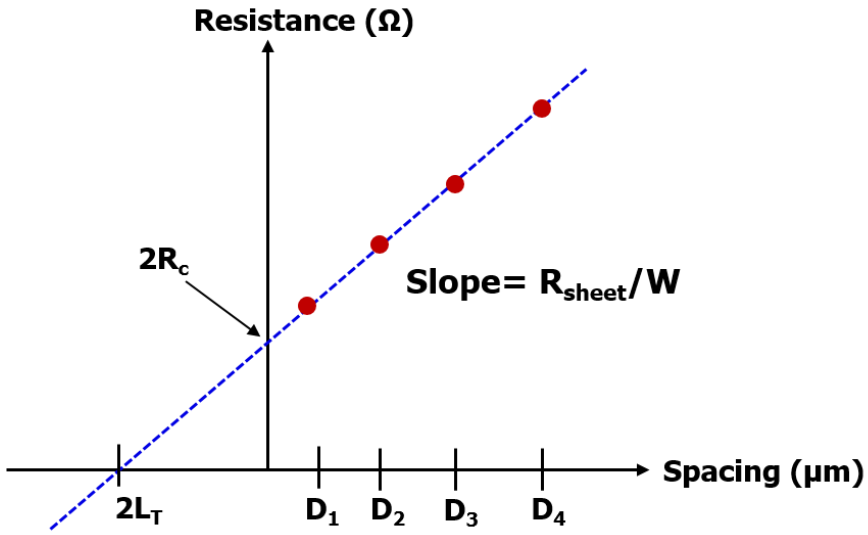

Figure 2.7 Plot of measured resistance as a function of a spacing between the metal pads.

The sheet resistance of the semiconductor can be calculated from the slope using the following equation:

$$R_s = Slope \cdot W \tag{2.12}$$

The intercepts with the *x*-axis and *y*-axis of the fitted line in Figure 2.7 are twice the transfer length, $2L_T$, and twice the contact resistance, $2R_C$, respectively. The transfer length is defined as the distance from the edge of the metal pad to the point that the contact voltage is 1/*e* of its maximum value, which is known as effective contact length. Then, the specific contact resistance that is related to the quality and the reliability of the devices can be calculated by following equations:

$$L_T = \frac{R_C}{R_S} = \sqrt{\frac{\rho_C}{R_S}} \tag{2.13}$$

$$R_c = \frac{R_s \cdot L_T}{W} \tag{2.14}$$

$$\rho_c = L_T \cdot W \cdot R_c \tag{2.15}$$

CHAPTER 3. ENHANCEMENT OF III-NITRIDE ULTRAVIOLET AVALANCHE PHOTODIODES

3.1 Introduction

As discussed above, the difficulty in growing high-quality AlGaN layers by strained heteroepitaxy hinders the realization of high-performance ultraviolet avalanche photodiodes (UV-APDs) based on wide-bandgap AlGaN materials. The lattice mismatch and difference thermal expansion coefficients between foreign substrates and epitaxial layers lead to the cracking and/or bowing of material structures and other strain-induced defects. In particular, the high density of crystalline defects, mainly threading dislocations, of AlGaN layers in an active region results in high leakage currents, disturbed electric field distributions, and premature microplasma breakdown prior to reaching avalanche breakdown [84, 85], which causes detrimental effects on device performance and reliability in the APDs. In addition, *n*- and *p*-type AlGaN layers have limited doping efficiency [86, 87, 88]. The development of a low-resistivity *n*-AlGaN:Si layer is important for achieving high-performance UV-APDs because the low resistivity of the *n*-AlGaN layer can reduce current crowding towards the edge of the mesa, which causes the potential premature microplasma breakdown of devices.

The use of low-dislocation-density GaN substrates has been reported for GaN *p*–*i*–*n* UV-APDs via the growth of homoepitaxial GaN layers, resulting in more significantly reduced leakage currents and higher optical gains than those in the case of growth on the sapphire substrate [59, 61, 89]. In the case of AlGaN UV-APDs, the effects

of threading dislocations on the performance characteristics of UV-APDs are expected to be significant, but they have not been systematically explored.

In this chapter, we report on the growth, fabrication, and device characterization of high-performance $Al_xGa_{1-x}N$ *p-i-n* UV-APDs with strain management in *n*-type layers grown on free-standing (FS) GaN and sapphire substrates to address technological issues associated with crystalline defects and crack formation in $Al_xGa_{1-x}N$ UV-APDs and reliability.

3.2 Design, Epitaxial Growth, and Device Fabrication

The epitaxial growth of $Al_{0.05}Ga_{0.95}N$ *p-i-n* UV-APDs was carried out by metalorganic chemical vapor deposition (MOCVD) in a Thomas Swan reactor system with a 6×2″ closed-coupled showerhead (CCS) growth chamber. For a native GaN substrate, an *n*-type FS-GaN substrate made from a thick film grown by hydride vapor phase epitaxy (HVPE) with a threading dislocation density lower than 5.0×10^6 cm^{-2}, was used. A GaN/sapphire template, grown on a *c*-plane sapphire substrate and composed of low- and high-temperature GaN buffer layers, followed by an approximately 3-μm-thick layer of unintentionally doped GaN, was used for the $Al_{0.05}Ga_{0.95}N$ *p-i-n* UV-APDs on a sapphire substrate. The dislocation density of the GaN/sapphire template was estimated to be $\sim5.4\times10^8$ cm^{-2} from the full-widths at half maximum (FWHMs) of the (002) and (102) X-ray diffraction (XRD) rocking curves [90]. Trimethylaluminum ($Al(CH_3)_3$, TMAl), trimethylgallium ($Ga(CH_3)_3$, TMGa), and ammonia (NH_3) were used as precursors. Bis-cyclopentadienyl magnesium ($Mg(C_6H_6)_2$, Cp_2Mg) and diluted silane

(SiH_4) were used as *p*- and *n*-type dopant precursors, respectively. Atomic-force microscopy (AFM), scanning electron microcopy (SEM), and X-ray diffraction (XRD) were employed to characterize the surface and crystalline quality of the epitaxial layer and device structures. XRD and photoluminescence (PL) were also used to evaluate the mole fraction of Al in the $Al_xGa_{1-x}N$ layers. Hall-effect measurements were also carried out for the *p*-$Al_{0.05}Ga_{0.95}N$:Mg, *n*-$Al_{0.02}Ga_{0.98}N$:Si, and *n*-GaN layers under various growth conditions in order to measure the electrical properties.

For a top-illuminated $Al_{0.05}Ga_{0.95}N$ *p-i-n* UV-APD structure, shown in Figure 3.1, the epitaxial layer structure of UV-APDs on FS-GaN substrate and GaN/sapphire template consisted a 0.45-µm-thick *n*-GaN:Si layer (n~4×10^{18} cm^{-3}), followed by a 0.15-µm-thick *n*-$Al_{0.02}Ga_{0.98}N$:Si layer (n~4×10^{18} cm^{-3}) for the step grading, a 0.3-µm-thick unintentionally doped $Al_{0.05}Ga_{0.95}N$ drift region, a 0.1-µm-thick *p*-$Al_{0.05}Ga_{0.95}N$:Mg layer (p~5×10^{17} cm^{-3}), and topped with a heavily doped 0.02-µm-thick *p*-$Al_{0.05}Ga_{0.95}N$:Mg^{++} ([Mg]~1×10^{20} cm^{-3}) contact layer. For the strain management and the crack-free growth of $Al_xGa_{1-x}N$ *p–i–n* UV-APD structures, step-graded layers from the *n*-GaN:Si to *n*-$Al_{0.02}Ga_{0.98}N$:Si layers were introduced instead of a thick *n*-$Al_{0.05}Ga_{0.95}N$:Si layer.

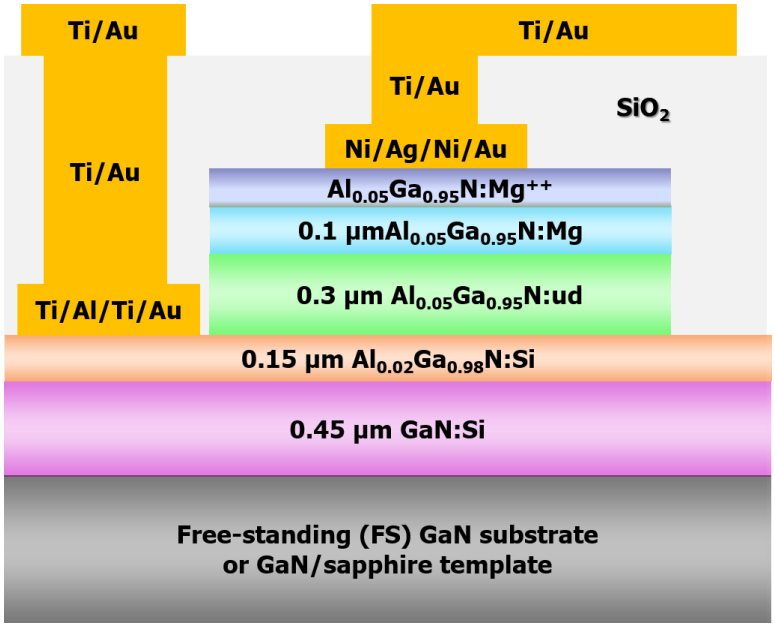

Figure 3.1 Schematic the cross-sectional structure of $Al_xGa_{1-x}N$ *p-i-n* UV-APD grown on free-standing (FS)-GaN substrate and GaN/sapphire template.

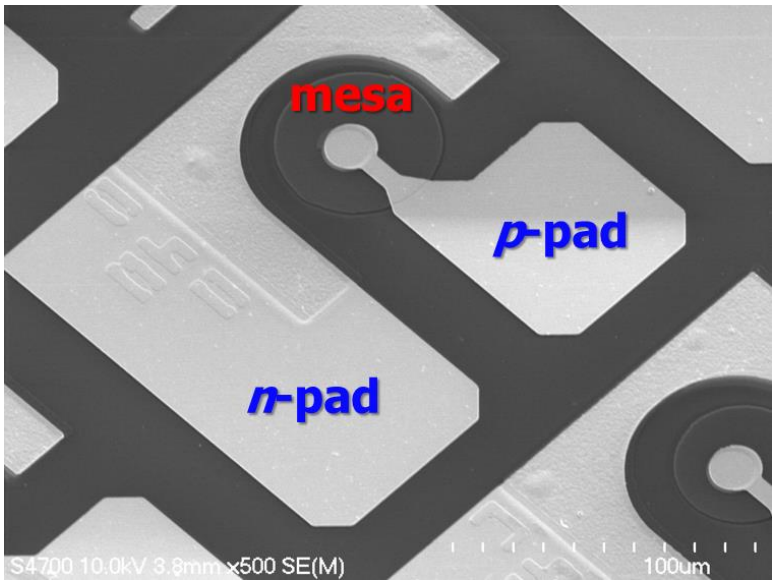

Figure 3.2 Scanning electron microscopy (SEM) image of fabricated $Al_xGa_{1-x}N$ *p-i-n* UV-APDs with bonding pads.

X-ray diffraction ω-2θ scans near a GaN (004) diffraction peak are shown in Figure 3.3. Although both AlGaN *p-i-n* UV-APDs on FS-GaN substrate and GaN/sapphire template were grown under the same growth conditions, XRD peaks corresponding to each layer in their epitaxial layer structures slightly differed, which can be attributed to the difference in actual substrate surface temperatures caused by the thermal conductivities of the different substrates and the strain/bowing status of the growing surface depending on the substrate used [91].

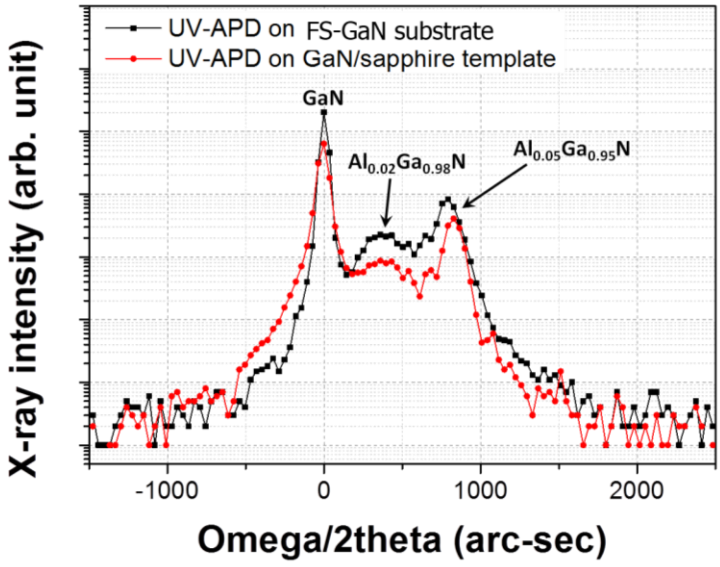

Figure 3.3 HR-XRD ω-2θ scan results of (004) diffraction for the AlGaN *p-i-n* UV-APDs on FS-GaN substrate and GaN/sapphire template.

The doping calibration of *n*- and *p*-type in the $Al_xGa_{1-x}N$ layers were performed for AlGaN *p-i-n* UV-APDs. For the optimization of *n*- and *p*-type $Al_xGa_{1-x}N$ layers, we modified the SiH_4 flow rates for the *n*-type AlGaN layer, and the growth rate and

precursors for the *p*-type AlGaN layer. The Hall-effect measurement results, plotted in Figure 3.4 and Figure 3.5, show that the reduced bulk and sheet resistivity of the *n*-AlGaN:Si layer ($x \leq 0.05$) with an increasing SiH_4 flow rates. Also, while the electron concentration linearly increases within the range of the SiH_4 flow rates controlled in this study, the electron mobility decreases.

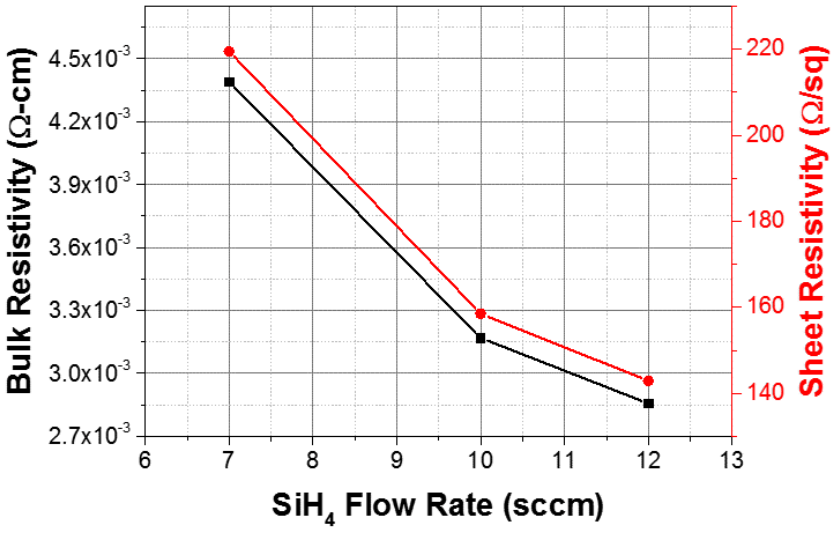

Figure 3.4 Bulk and sheet resistivity of the *n*-$Al_xGa_{1-x}N$:Si layer ($x \leq 0.05$) with various SiH_4 flow rates measured by the Hall-effect measurement.

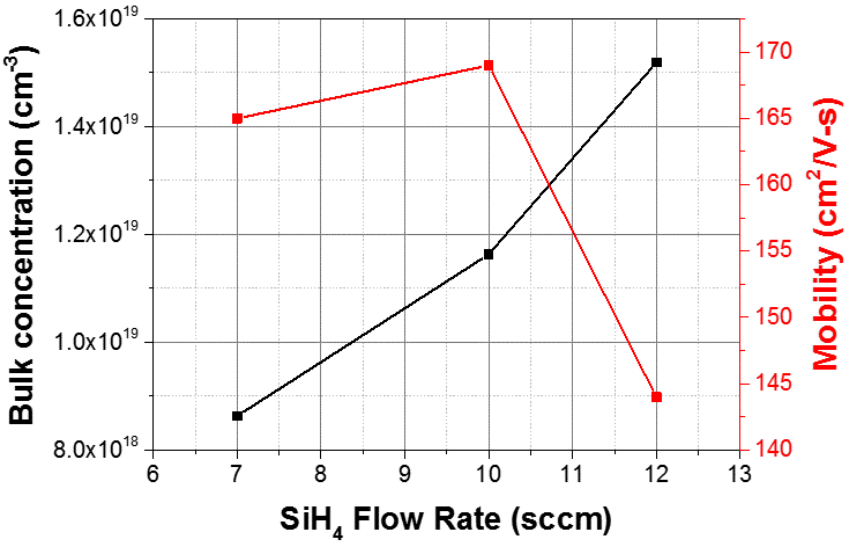

Figure 3.5 Free-electron concentration and mobility of the *n*-$Al_xGa_{1-x}N$:Si layer ($x \leq 0.05$) with various SiH_4 flow rates measured by the Hall-effect measurement.

The optimization of *p*-$Al_xGa_{1-x}N$:Mg layer was also performed, which improved the performance of the AlGaN *p-i-n* UV-APDs. The *p*-type electrical properties were studied with respect to the Al mole fraction ($0.05<x<0.1$) in the *p*-$Al_xGa_{1-x}N$:Mg layer. The growth rate of the *p*-$Al_xGa_{1-x}N$:Mg layer slightly changed from 1.0 μm/h to 0.8 μm/h for higher and lower Al compositions, respectively, by controlling group-III and group-V precursors to achieve a corresponding Al mole fraction and Mg doping efficiency. The Hall measurements of the *p*-$Al_xGa_{1-x}N$:Mg layers with various Al mole fractions were also performed to characterize the *p*-type electrical properties, as shown in Figure 3.6. Both bulk and sheet resistivity are relatively low in the case of the *p*-$Al_xGa_{1-x}N$:Mg layers with lower Al mole fractions but increase as the Al mole fraction increase. The increase in the resistivity of the *p*-$Al_xGa_{1-x}N$:Mg layer with an increasing Al mole fraction

possibly originated from increased Mg activation energy at the higher Al mole fraction and reduced Mg incorporation at the higher growth rate [92, 93, 94]. In turn, because of the limited free-hole concentration and mobility, which depended on the Al composition, the resistivity of the *p*-$Al_xGa_{1-x}N$:Mg layer increases as the Al mole fraction increases.

As a result, the optimized free-electron concentration of the *n*-$Al_xGa_{1-x}N$:Si layer ($x \leq 0.05$) is estimated at n~4.0×10^{18} with a mobility value of μ_n~226 cm^2/V-s. The optimized free-hole concentration of the *p*-$Al_{0.05}Ga_{0.95}N$:Mg layer is measured at p~5.1×10^{17} with a mobility value of μ_p~7 cm^2/V-s, resulting in a resistivity of 1.7 Ω·cm at room temperature.

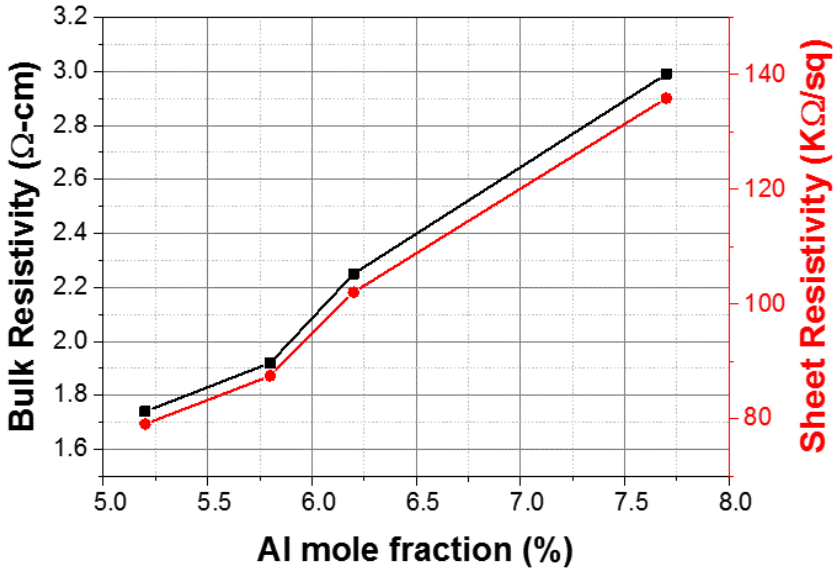

Figure 3.6 Bulk and sheet resistivity of the *p*-$Al_{0.05}Ga_{0.95}N$:Mg layer with different Al mole fraction measured by the Hall-effect measurement.

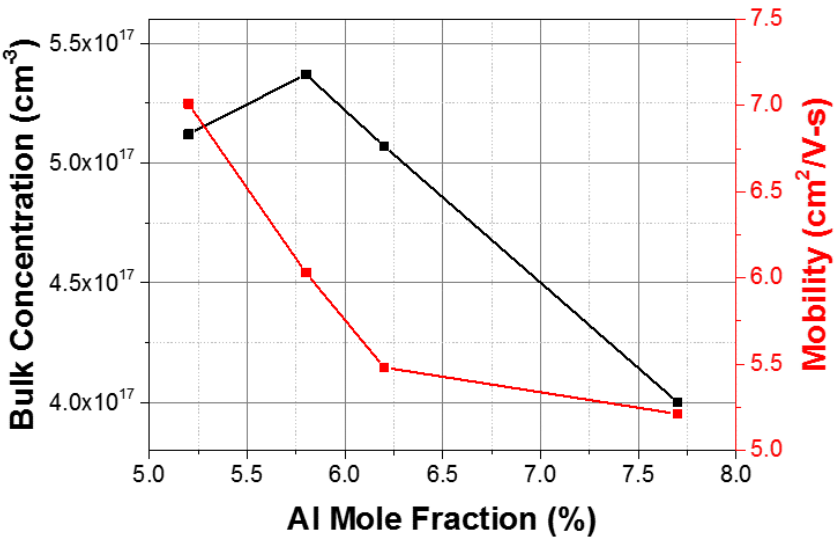

Figure 3.7 Free-electron concentration and mobility of the *p*-$Al_{0.05}Ga_{0.95}N$:Mg layer with different Al mole fraction measured by the Hall-effect measurement.

For the fabrication of top-illuminated devices, we formed circular mesas with sizes varying from 30- to 70-μm-diameter by inductively-coupled plasma reactive-ion etching (ICP-RIE) using a $Cl_2/BCl_3/Ar$ carrier gas mixture. Ti/Al/Ti/Au and Ni/Ag/Ni/Au metal stacks were deposited by electron-beam evaporation and annealed by rapid thermal annealing (RTA) system for the *n*- and *p*-type ohmic contacts, respectively. In order to optimize annealing conditions for ohmic contact behavior, and *n*- and *p*-type AlGaN layers were annealed at various temperatures. The optimized annealing conditions for *n*- and *p*-type AlGaN layers were at 700℃ for 1 min under N_2 ambient and at 450℃ for 1 min under compressed dry air (CDA), respectively. The fabricated devices were then passivated by depositing a layer of SiO_2 using plasma-enhanced chemical vapor deposition (PECVD) by accessing via-holes formed by a subsequent dry etching process. Finally, thick Ti/Au metal stacks for use as metal interconnects and bonding pads were

deposited by electron-beam evaporation. Figure 3.8 shows the fabrication process flow of $Al_{0.05}Ga_{0.95}N$ *p-i-n* UV-APDs.

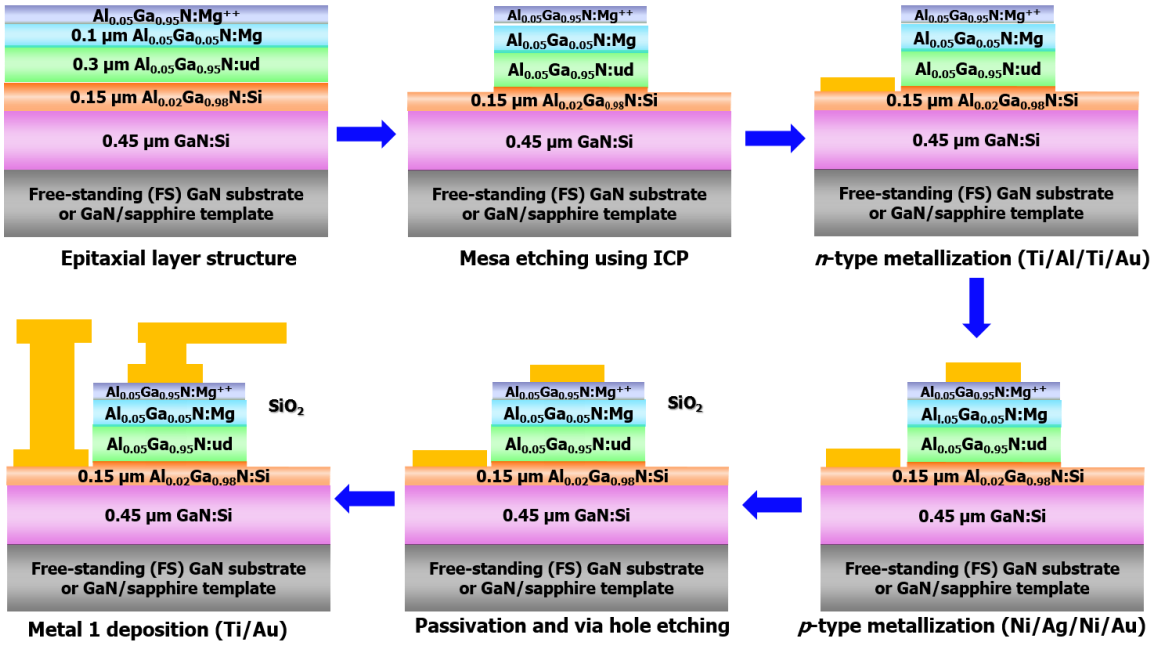

Figure 3.8 The fabrication process flow of $Al_{0.05}Ga_{0.95}N$ *p-i-n* UV-APDs.

Moreover, the effect of ohmic contact using *p*-GaN:Mg^{++} and *p*-$Al_{0.05}Ga_{0.95}N$:Mg^{++} capping layers on the top of *p*-$Al_{0.05}Ga_{0.95}N$:Mg layer were investigated. As shown in Figure 3.9 and Figure 3.10, no significant differences in the values of the R_{sh} and R_c are observed, indicating that the UV-APDs having different *p*-type contact layers have similar electrical properties in the *p*-type layers.

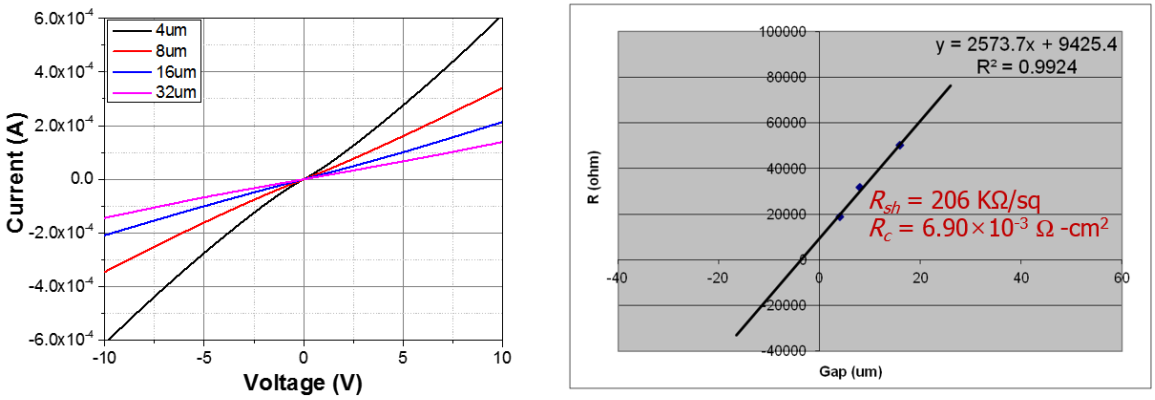

Figure 3.9 *p*-TLM result of UV-APDs with *p*-$Al_{0.05}Ga_{0.95}N$:Mg^{++} contact layer.

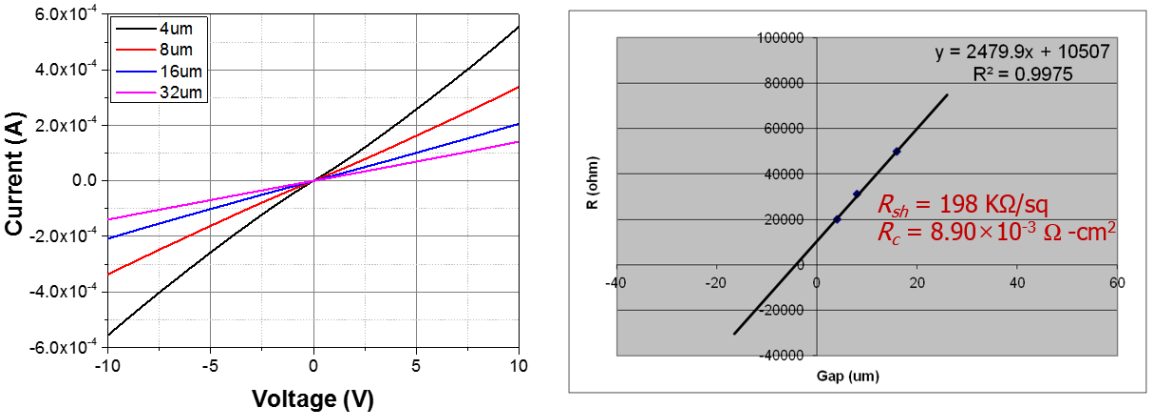

Figure 3.10 *p*-TLM result of UV-APDs with *p*-GaN:Mg^{++} contact layer.

3.3 Comparison of $Al_{0.05}Ga_{0.95}N$ *p-i-n* Ultraviolet Avalanche Photodiodes Grown on Free-Standing GaN Substrate and GaN/sapphire Template

The microscopic surface properties of the AlGaN *p-i-n* UV-APD epitaxial structures grown on the FS-GaN substrate and the GaN/sapphire template were characterized by AFM measurement. Figure 3.11 shows plots of the surface morphology and the corresponding root-mean-square (RMS) surface roughness of the structures with various AFM scan sizes. The RMS surface roughnesses of 1×1, 5×5, and 20×20 μm^2 scans with a height scale of 10 nm are ~0.11, ~0.28, and ~2.27 nm for the structure grown on the FS-GaN substrate and ~0.14, ~0.34, and ~2.33 nm for the structure grown on the GaN/sapphire template, respectively. Both UV-APD epitaxial structures have similar RMS roughness and well-developed atomic step-flow morphologies. However, the surface of the epitaxial layer grown on the GaN/sapphire template shows dislocation-related surface features that are not observed in that grown on the FS-GaN substrate, as shown in the AFM surface images (5×5 μm^2 scan) in Figure 3.12 and Figure 3.13. The density of the surface features of the structure on the GaN/sapphire template is estimated to be $\sim 7.6 \times 10^7$ cm^{-2}. The improved surface property of the structure grown on the FS-GaN substrate is believed to be a result of epitaxial growth on the low-dislocation-density substrate.

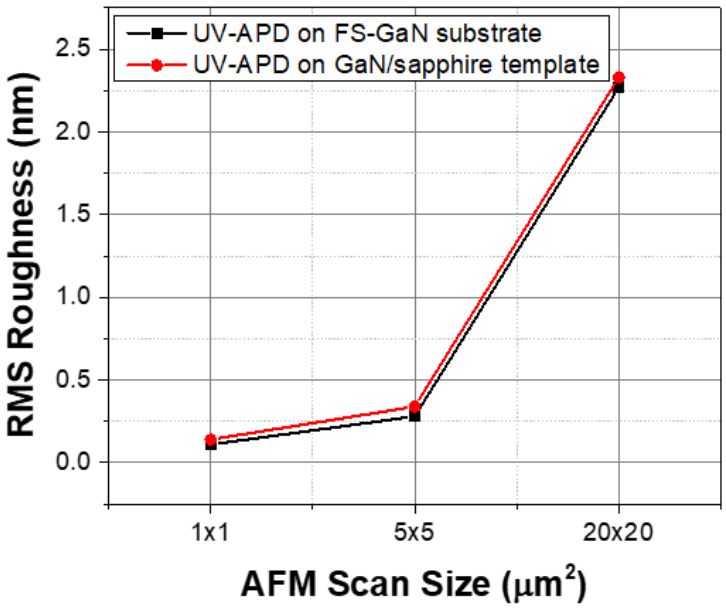

Figure 3.11 AFM RMS roughness of $Al_{0.05}Ga_{0.95}N$ *p–i–n* UV-APDs grown on a FS-GaN substrate (black squares) and a GaN/sapphire template (red circles) with different AFM scan areas.

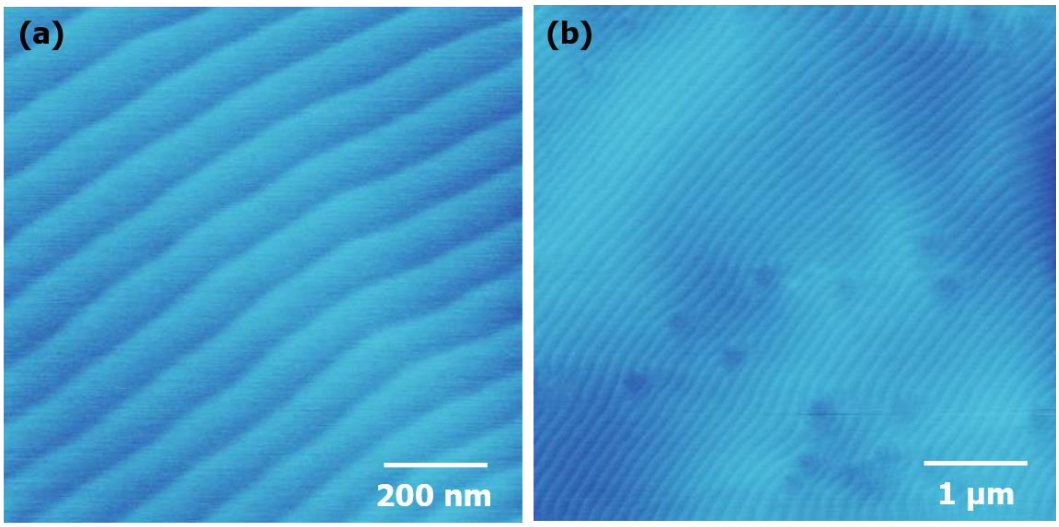

Figure 3.12 AFM microscopic surface morphology of AlGaN *p-i-n* UV-APDs grown on a GaN/sapphire template: (a) with 1×1 μm^2 scan with z-height scale of 5 nm; (b) with 5×5 μm^2 scan with z-height scale of 10 nm.

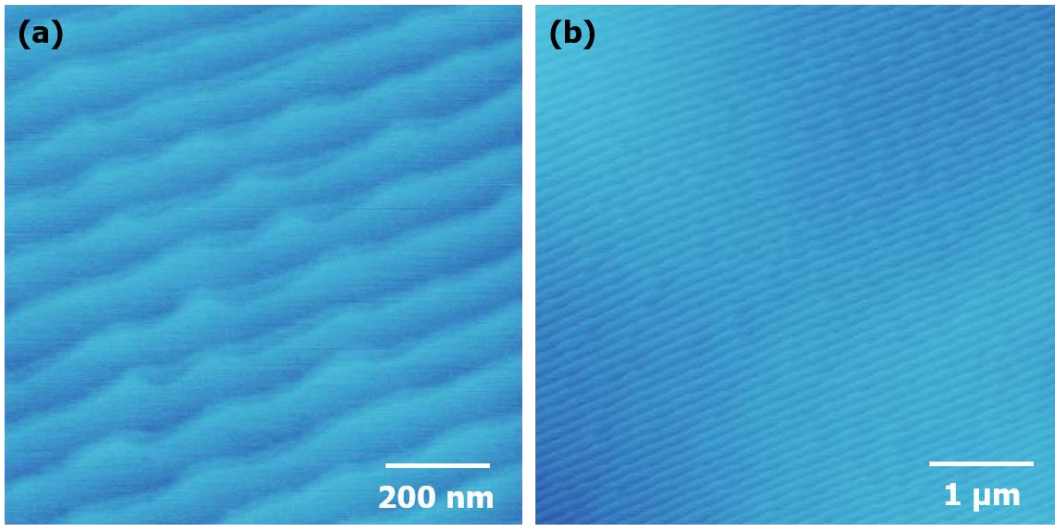

Figure 3.13 AFM microscopic surface morphology of AlGaN *p-i-n* UV-APDs grown on a FS-GaN substrate: (a) with 1×1 μm^2 scan with z-height scale of 5 nm; (b) with 5×5 μm^2 scan with z-height scale of 10 nm.

Current-voltage (*I*–*V*) characteristics were measured using a Keithley 4200 semiconductor characterization system. In Figure 3.14, the breakdown voltages (V_{BR}) and dark-current densities of $Al_{0.05}Ga_{0.95}N$ *p*-*i*-*n* UV-APDs grown on the FS-GaN substrate and the GaN/sapphire template are compared under various mesa sizes. The V_{BR} values derived from the onset point of reverse breakdown measured without UV illumination and averaged dark-current densities taken from the reverse bias (V_R) at 0 V<V_{BR} were used for the plot. For the area-dependent V_{BR}, UV-APDs grown on the same substrate show a relatively constant V_{BR} regardless of the device sizes: The V_{BR} values range from 95 to 100 V for the UV-APDs on the FS-GaN substrate and from 87 to 89 V for those on the GaN/sapphire template. Since all the UV-APDs grown on the FS-GaN substrate and the GaN/sapphire template share nearly the same growth conditions, the difference in V_{BR} might be attributed mostly to the defect-related crystalline quality of the UV-APDs. The dark current densities are significantly lower for the UV-APDs on the FS-GaN substrate than for those on the GaN/sapphire template. When device sizes are small (areas less than 1,500 μm^2), the difference is approximately one order of magnitude. When device sizes are large (areas larger than 2,500 μm^2), the difference is about a factor of 2 or 3, as the dark-current density of the UV-APDs on the FS-GaN substrate increases with the device sizes. As dislocations in the device increase the dark-current density by a trap-assisted tunneling current at a certain reverse bias and produce premature microplasmas prior to the onset point of avalanche breakdown, the use of the FS-GaN substrate with a low dislocation density was responsible for the low dark current density and constant breakdown voltage of the UV-APDs.

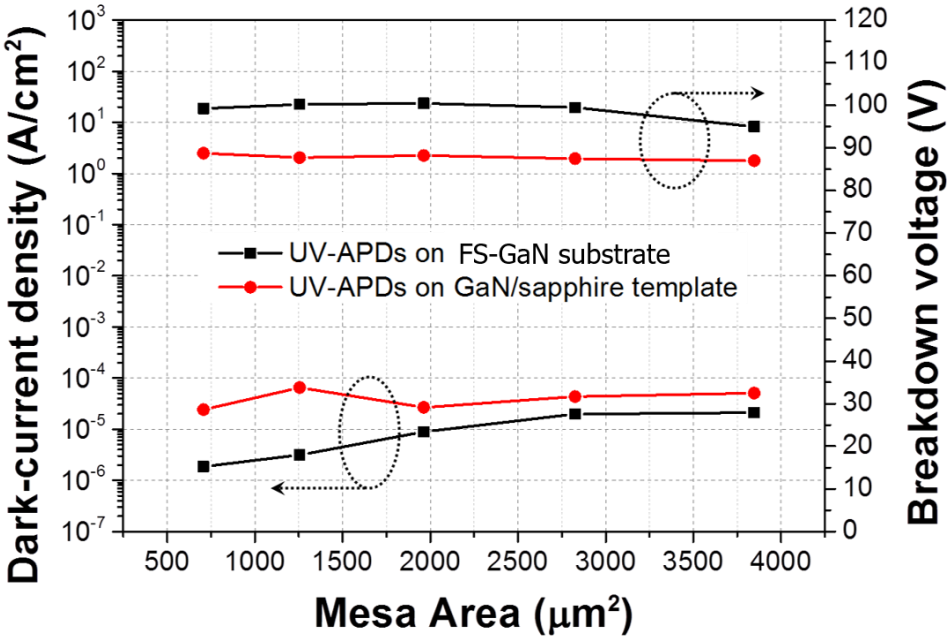

Figure 3.14 Area-dependent dark-current densities and breakdown voltages of $Al_{0.05}Ga_{0.95}N$ *p–i–n* UV-APDs grown on a FS-GaN substrate and a GaN/sapphire template.

In addition to the dislocation-related dark-current density in the epitaxial structure, the increment in the dark-current density according to the mesa size in the UV-APDs also revealed that surface leakage along the mesa sidewall may have led to the increase in the dark-current density. The differences in the dark current density according to the mesa sizes in each dark-current plot are 1.92×10^{-5} and 2.67×10^{-5} A/cm^2 for the UV-APDs grown on the FS-GaN substrate and the GaN/sapphire template, respectively. The small changes in the dark-current density with respect to the mesa sizes in each plot indicated low surface leakage current despite the sharp mesa sidewall profile applied in this study. The low etch damage of the mesa definition and high-quality dielectric

passivation during the fabrication process possibly contributed to reducing the leakage current through the mesa sidewall surfaces.

Figure 3.15 (a) and (b) show the reverse-biased *I*–*V* characteristics of a 40-μm-diameter (corresponding to a mesa area of 1,256 μm^2) $Al_{0.05}Ga_{0.95}N$ *p*-*i*-*n* UV-APD grown on the FS-GaN substrate or the GaN/sapphire template, respectively. In Figure 3.15 (a), the onset point of the V_{BR} of the UV-APD grown on the FS-GaN substrate is ∼100 V, and the dark current increases sharply above the onset point of V_{BR}. Photocurrent distributions based on V_R were obtained by UV light of λ = 280 nm, which illuminated the device from the front surface of the $Al_{0.05}Ga_{0.95}N$ *p*-*i*-*n* UV-APDs. The avalanche gain was calculated by the difference between the photocurrent and the dark current at a V_R normalized by the unity-gain photocurrent taken from the flat regime of the reverse-biased *I*–*V* plot. The avalanche gain is defined as:

$$\text{Avalanche Gain} = \frac{I_{photo} - I_{dark}}{I_{photo(unity)} - I_{dark(unity)}} \tag{3.1}$$

Since the stable current region of the photocurrent at a relatively low V_R depends solely on photon absorption when the dark current related to the leakage current is subtracted from the photocurrent, the relatively flat current region was taken as the unity-gain point. The estimated avalanche gain is about 82 at the onset point of V_{BR} = 100 V and exceeded 5 × 10^5 beyond V_{BR} = 102 V. This sharp increase in the avalanche gain

implies that the device underwent a strong avalanche multiplication process above the onset point of V_{BR}.

Figure 3.15 (b) shows that the dark-current density of the UV-APD grown on the GaN/sapphire template is higher than that of the UV-APD grown on the FS-GaN substrate in the entire reverse-bias regime and increases dramatically even at a low reverse bias. The averaged dark-current densities taken from 0 V < V_R < V_{BR} for each device are ~3.1×10^{-6} and ~6.5×10^{-5} A/cm^2 for the 40-μm-diameter UV-APDs grown on the FS-GaN substrate and the GaN/sapphire template, respectively. The high dislocation density in the active region of the UV-APD grown on the GaN/sapphire template was responsible for the significantly greater dark-current density than that of the UV-APD grown on the FS-GaN substrate. In addition, the photocurrent of the UV-APD grown on the GaN/sapphire template remains flat up to V_R of ~30 V; then it increases exponentially with a reverse bias up to the onset point of V_{BR} of ~87 V, followed by a sharp increase above the onset point of V_{BR} because of the active avalanche multiplication process. The gradually increased photocurrent at V_R > 30 V is attributed to the trap-assisted leakage current promoted in the relatively high reverse-bias regime, indicating the high dislocation density in the active region of the UV-APD grown on the GaN/sapphire template. The calculated avalanche gain of the UV-APD grown on the GaN/sapphire template are ~160 at V_{BR}=88 V and exceeded 2×10^4 at V_{BR}=93 V. From these observed low dark-current densities and the avalanche breakdown with a high avalanche gain measured for the UV-APDs grown on the FS-GaN substrate, we can infer that $Al_{0.05}Ga_{0.95}N$ UV-APDs grown on the FS-GaN substrate can be efficiently used for applications of high-sensitivity UV optical detection.

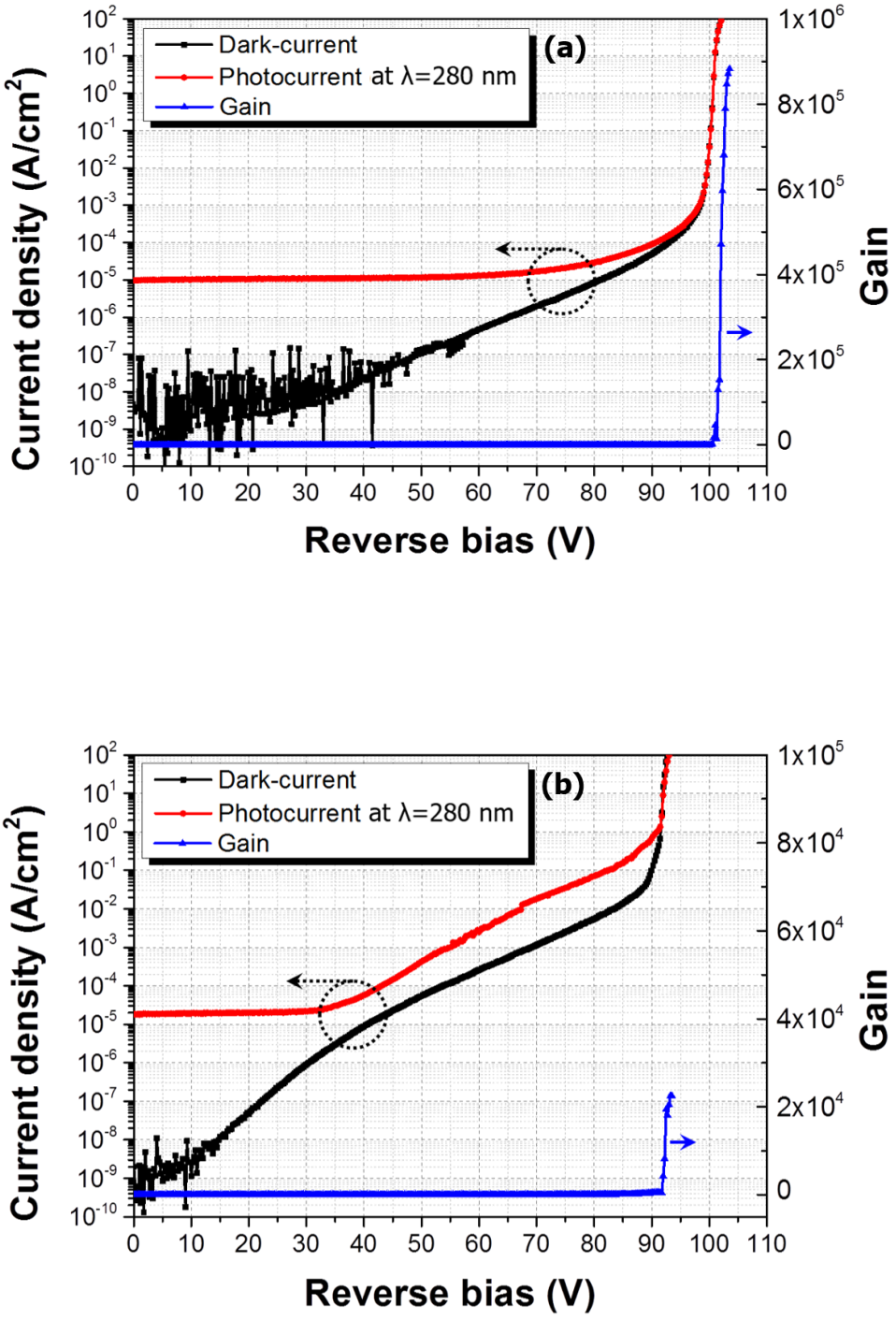

Figure 3.15 Reverse-biased *I–V* characteristics for a 40-µm-diameter (corresponding to 1,256µm^2) $Al_{0.05}Ga_{0.95}N$ *p–i–n* UV-APD grown on (a) a FS-GaN substrate and (b) a GaN/sapphire template.

The onset point of the V_{BR} of the $Al_{0.05}Ga_{0.95}N$ UV-APD grown on the FS-GaN substrate is found at ~95 V, and no premature microplasma breakdown is observed even in the multiple *I*–*V* scans of a large device with V_R up to 90 V. Although UV-APDs grown on the FS-GaN substrate were robust and consistent with the multiple *I*–*V* scans, premature microplasma breakdown was frequently observed during the characterization of UV-APDs grown on the GaN/sapphire template. The compromised performance and reliability of the measured UV-APDs grown on the GaN/sapphire template, compared with those of the UV-APDs grown on the FS-GaN substrate, were attributed to the high defect density in the active region.

3.4 Improvement of High-performance $Al_{0.05}Ga_{0.95}N$ *p-i-n* Ultraviolet Avalanche Photodiodes Grown on Free-Standing GaN Substrate

To investigate the surface and material quality of the $Al_{0.05}Ga_{0.95}N$ *p-i-n* UV-APD structure with respect to the step-graded *n*-type layers, this study involved the preparation of two $Al_{0.05}Ga_{0.95}N$ *p-i-n* UV-APDs grown on GaN/sapphire templates: One had an *n*-$Al_xGa_{1-x}N$:Si layer with a constant Al mole fraction (x=0.05), and the other had step grading in the *n*-$Al_xGa_{1-x}N$:Si layer (x=0, 0.02). At the same time, the total thickness of $Al_xGa_{1-x}N$ and growth conditions for the other layers of the devices were kept identical, as shown in Figure 3.16.

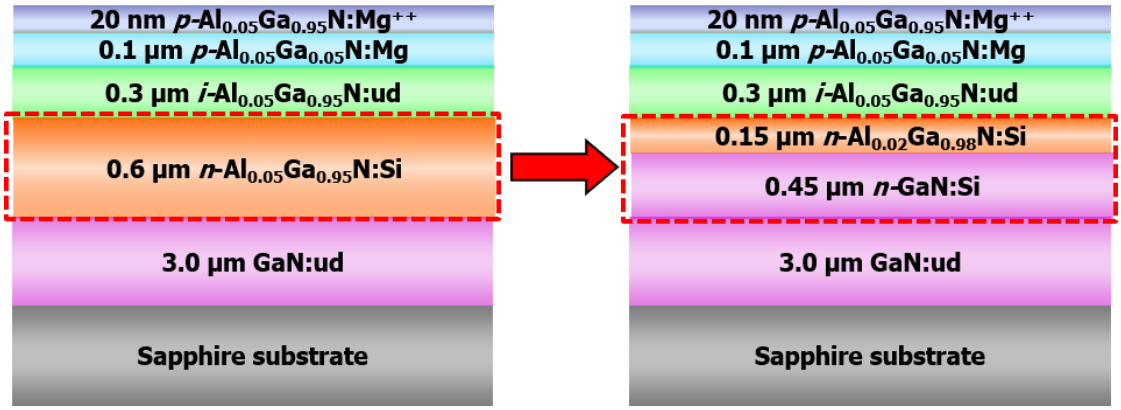

Figure 3.16 Schematic the cross-sectional structure of AlGaN *p-i-n* UV-APD grown on GaN/sapphire templates without and with step grading in *n*-$Al_xGa_{1-x}N$:Si layer.

Figure 3.17 (b) and (c) show the AFM surface images of the UV-APD epitaxial structure with a single *n*-$Al_{0.05}Ga_{0.95}N$:Si layer and step-graded *n*-GaN and *n*-$Al_{0.02}Ga_{0.98}N$ layers, respectively. The RMS surface roughness and the density of surface features for the structure with an *n*-$Al_{0.05}Ga_{0.95}N$:Si layer are ~0.38 nm and ~1.64×10^{8} cm^{-2}, respectively, while those with step-graded *n*-layers are ~0.34 nm and ~7.6×10^{7} cm^{-2}, respectively, as measured from multiple 5×5 μm^2 scans. The surface of the device structure using step-graded *n*-AlGaN:Si layers exhibited improved morphology with lower surface roughness and about half the surface defect density as that of the structure with an *n*-$Al_{0.05}Ga_{0.95}N$ layer.

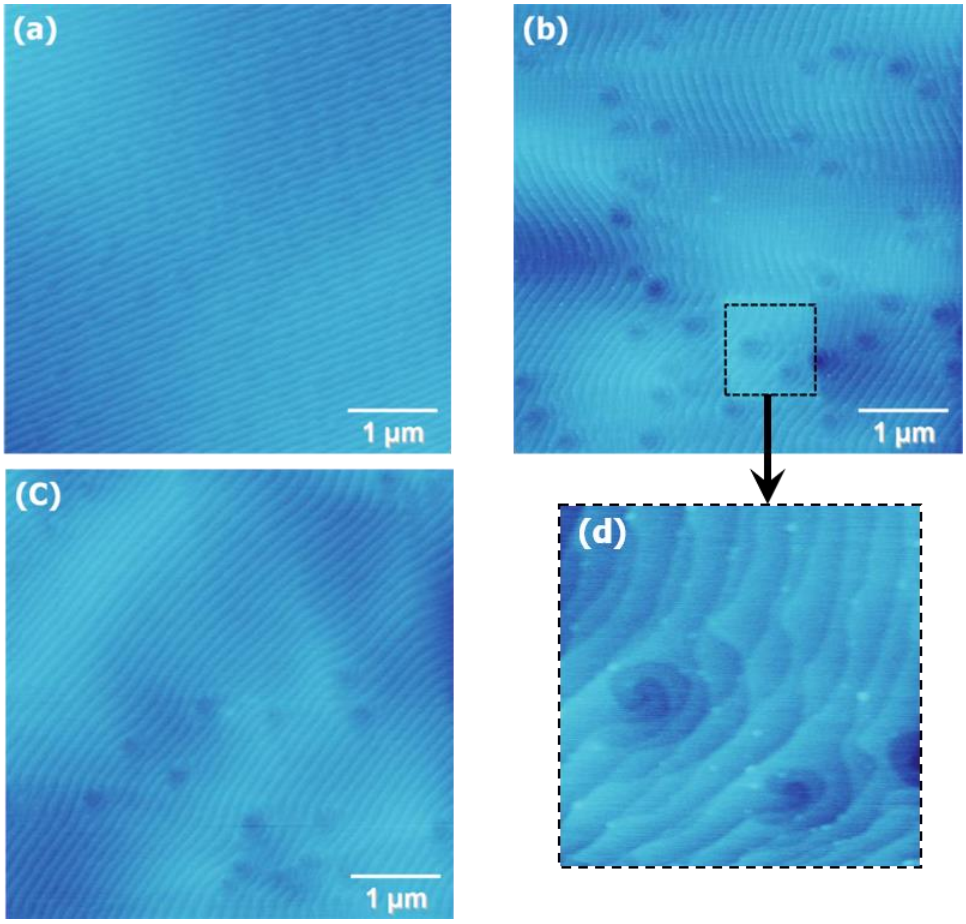

Figure 3.17 AFM surface morphology of $Al_{0.05}Ga_{0.95}N$ *p-i-n* UV-APDs grown on (a) a GaN substrate, (b) a GaN/sapphire template with an *n*-$Al_{0.05}Ga_{0.95}N$:Si layer, (c) a GaN/sapphire template with step-graded *n*-layers (*n*-$Al_{0-0.02}Ga_{1-0.98}N$:Si), and (d) shows an expanded image of the surfaece morphology in the dotted square of (b).

The electric field distribution in the $Al_{0.05}Ga_{0.95}N$ *p-i-n* UV-APD was calculated by a one-dimensional simulation as shown in Figure 3.18 at a reverse bias of V_R=97.5 V that is an onset point of breakdown V_{BR}. The maximum electric field in the device structure is about 3.2 MV/cm at V_{BR}=97.5 V, which is the value in between the reported critical electric field of GaN (2.4~3.3 MV/cm) [66, 95, 96] and that of $Al_{0.22}Ga_{0.78}N$ (3.5

MV/cm) [97]. Considering that the active layer is composed of $Al_{0.05}Ga_{0.95}N$ layer, the electric field of 3.2 MV/cm calculated in this study is consistent with the values reported in literatures for avalanche breakdown multiplication.

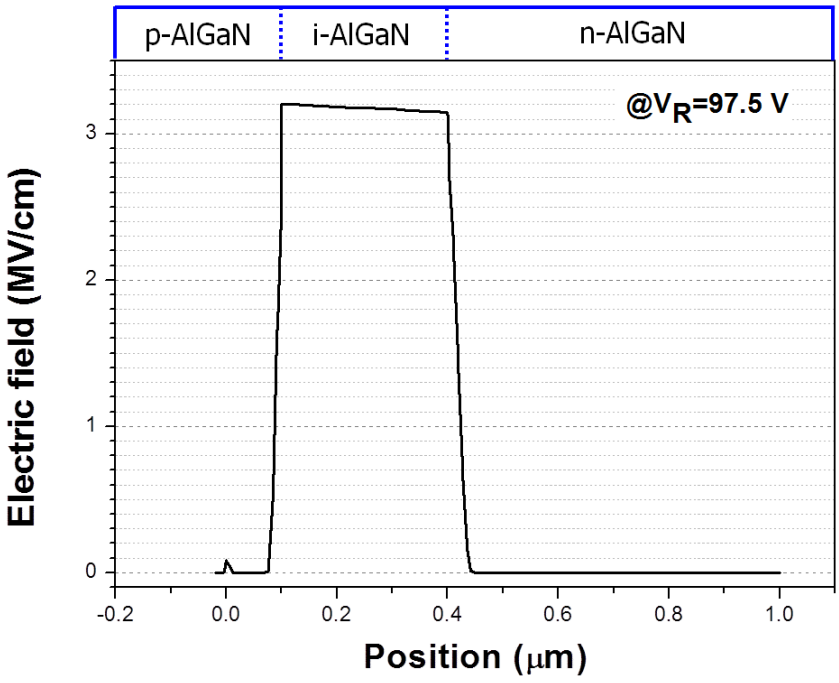

Figure 3.18 The electric field distribution of the $Al_{0.05}Ga_{0.95}N$ *p-i-n* UV-APD at reverse bias of V_R=97.5 V.

In general, the extended depletion region into the *n*- and *p*-$Al_{0.05}Ga_{0.95}N$ layer can drop the critical electric field, so that we need to apply higher reverse bias to have avalanche multiplication in the UV-APD structure. In addition, unintentionally thicker i-$Al_{0.05}Ga_{0.95}N$ layer can decrease the critical electric field as well as the partially expanded depletion region. In this study, even though the nominal thickness of the unintentionally

doped *i*-$Al_{0.05}Ga_{0.95}N$ layer is 300 nm, the actual thickness of the *i*-$Al_{0.05}Ga_{0.95}N$ layer may be different from the nominal value because of an error in thickness measurement using reflectance of certain light source and the Mg memory effect that results in delayed Mg incorporation until certain saturation point of a growth chamber is reached. This Mg memory effect can make gradually increased Mg atom concentration in the *p*-$Al_{0.05}Ga_{0.95}N$ layer near *p*-$Al_{0.05}Ga_{0.95}N$/*i*-$Al_{0.05}Ga_{0.95}N$ junction according to growth conditions, which can act as an additional *i*-$Al_{0.05}Ga_{0.95}N$ region. Thus, these unintentionally increased depletion areas would drop the critical electric field.

As shown in Figure 3.19 (a), under dark condition, the $Al_{0.05}Ga_{0.95}N$ UV-APD with a mesa size of 30-μm-diameter shows very low leakage currents of I_R<1 pA, up to V_R~60 V. For the V_R greater than 60 V, however, the dark-current increases monotonically until the impact ionization process starts to dominate the current flow and reached I_R~7 nA (equivalent to J_R~8×10^{-4} A/cm^2) at V_R=97 V. Beyond this point, the dark-current starts to increase sharply with increasing reverse bias, suggesting the active impact ionization of excess carriers in the multiplication region. With repeated tests, the *I-V* characteristic of each test also showed the consistent breakdown voltage and leakage current behavior. Under the UV-light illumination with a peak wavelength of λ=280 nm, the photocurrent remains constant up to V_R of 60 V and then exhibits an increase over the dark-current background when V_R>60 V (see Figure 3.19 inset). The avalanche gain of the measured device is about 40 at the onset point of breakdown voltage (V_{BR}) of 97.5 V and then rapidly increases with reverse bias. At a V_{BR} =102 V, the avalanche gain reaches at a maximum value of higher than 2×10^6. The significantly increased avalanche gain at

the high-reverse-bias regime indicated that the device experiences a firm avalanche multiplication process.

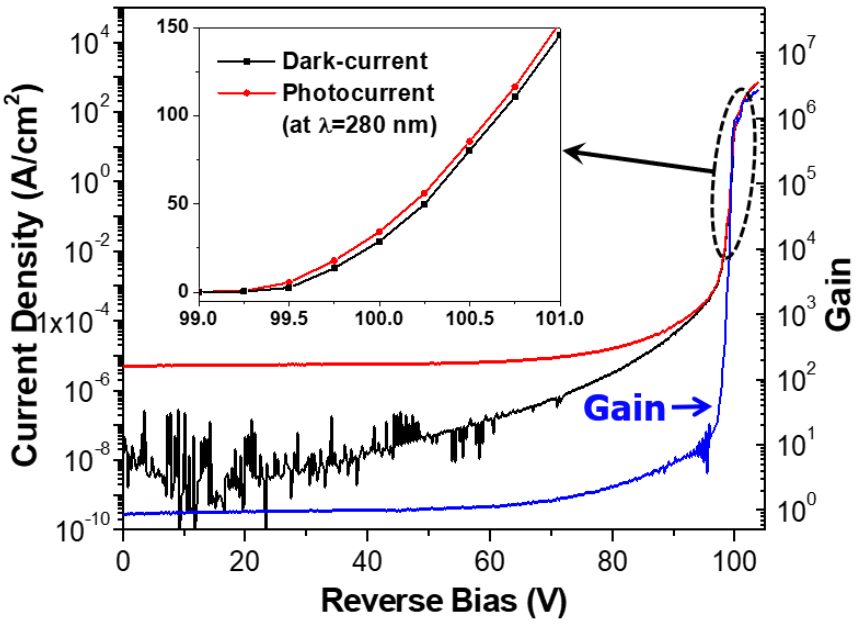

Figure 3.19 Reverse bias *I–V* characteristics of an $Al_{0.05}Ga_{0.95}N$ UV-APD with a mesa diameter of 30 μm with and without UV illumination at λ = 280 nm.

Figure 3.20 presents the comparison of the V_{BR} and the dark-current density of the $Al_{0.05}Ga_{0.95}N$ UV-APDs with different mesa areas. The area-dependent properties of GaN UV-APDs having a similar *p-i-n* epitaxial layer structure grown on a GaN substrate are also plotted for comparison. The values of the V_{BR} and the dark-current densities were derived from the onset point of breakdown and the averaged dark current density at the reverse biases between 0 V and 60 V, respectively. The V_{BR} of the devices with different mesa sizes are in the range of between 94 V and 99 V. The difference in V_{BR} between

$Al_{0.05}Ga_{0.95}N$ and GaN UV-APDs may result from the slightly different thickness of the drift region. Even though the averaged dark-current density increases with the mesa area, the values are maintained less than 5×10^{-7} A/cm^2 for all the mesa areas, which is also similar to those of the GaN UV-APDs [89].

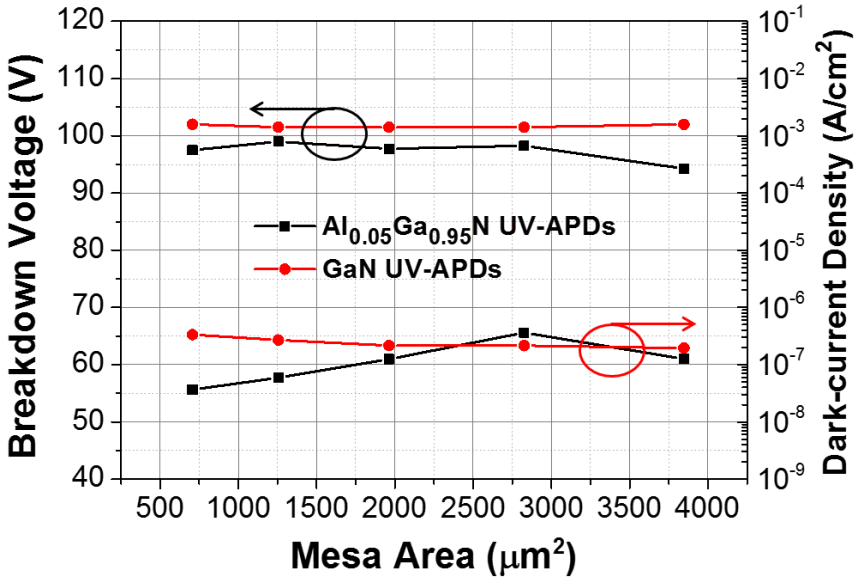

Figure 3.20 Area-dependent breakdown voltages and dark-current densities of $Al_{0.05}Ga_{0.95}N$ UV-APDs compared with GaN UV-APDs, both grown on GaN substrates.

Figure 3.21 shows the photocurrent densities taken from the flat region of the reverse-biased *I-V* plots less than 60 V and the avalanche gain of $Al_{0.05}Ga_{0.95}N$ UV-APDs, as a function of the mesa areas. The unity-gain photocurrent density shows relatively uniform distribution for all measured devices having different mesa sizes. However, the maximum avalanche gains of the devices measured at V_R=102 V exhibits a decreasing

trend from 2×10^6 for the 30-μm-diameter device to 1.5×10^5 for the 60-μm-diameter device and then increases to 1×10^6 for the 70-μm-diameter device, which is an opposite trend from distribution of the dark-current densities according to mesa areas as shown in Figure 3.21, indicating detrimental effect of the leakage current on the avalanche gain. Although the maximum avalanche gain of the devices shows area-dependent behavior, resulting from the different leakage current because of the non-uniform defect density in the various mesa areas, the avalanche gain of greater than 1.5×10^5 regardless of mesa areas is significantly higher than that in the previously reported $Al_{0.05}Ga_{0.95}N$ UV-APDs [58]. The extremely low leakage current before avalanche breakdown and the constant breakdown behavior, followed by the very high avalanche gain for the $Al_{0.05}Ga_{0.95}N$ UV-APDs, are ascribed to the improved crystalline quality of the epitaxial layer with the reduced defect density by inserting the *n*-$Al_xGa_{1-x}N$ step graded layers for strain management and the optimized epitaxial layer structure. Furthermore, the low etch damage of the mesa and the high-quality dielectric passivation also plays an important role in the low leakage current and the stable avalanche breakdown despite the sharp mesa sidewall profile.

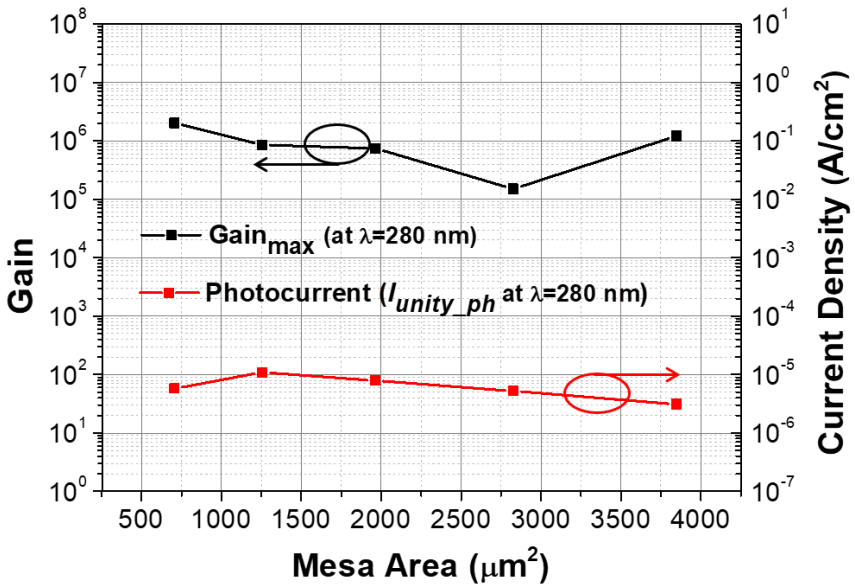

Figure 3.21 Photocurrent densities and avalanche gains of $Al_{0.05}Ga_{0.95}N$ *p-i-n* UV-APDs under UV illumination of λ=280 nm.

As shown in Figure 3.22, the spectral responsivity of a 70-μm-diameter (equivalent mesa area of 3847 μm^2) $Al_{0.05}Ga_{0.95}N$ *p-i-n* UV-APD was also measured under various reverse biases. The zero-biased photocurrent exhibits a peak absorption wavelength at $\lambda \sim 354$ nm that was equivalent to the band gap of the $Al_{0.05}Ga_{0.95}N$ layer. Also, these $Al_{0.05}Ga_{0.95}N$ devices exhibits an absorption cut-off wavelength of $\lambda \sim 370$ nm at zero bias, which is about 10 nm shorter than that of GaN *p–i–n* APDs. As the V_R increased, the peak absorption wavelength shifted slightly to 362 nm owing to the Franz–Keldysh effect in the multiplication layer, and the absorption cut-off wavelength significantly extended into the long-wavelength regime at high reverse biases, indicating that the depletion region extended into the *p*-type layer where the acceptor-state absorption could play a significant role in the broadening and red-shifting of the

absorption spectrum [59]. The device shows a peak responsivity of 43.4 mA/W at 354 nm under zero bias, corresponding to an external quantum efficiency (EQE) of ~16%. However, at V_R=80 V, the peak responsivity increases to 221.8 mA/W at 362 nm, corresponding to an EQE of ~94%. The fully extended depletion region into the *p*- and *n*-type regions, resulting from the increased V_R, may be the origin of the improvement of the photoresponse. In addition, at V_R > 90V, the significant increase in photocurrent is observed owing to the impact ionization as the $Al_{0.05}Ga_{0.95}N$ *p-i-n* UV-APD approaches avalanche multiplication. We note that the front illumination used in this experiment will severely reduce the measured EQE owing to significant absorption in the *p*-$Al_{0.05}Ga_{0.95}N$ layer.

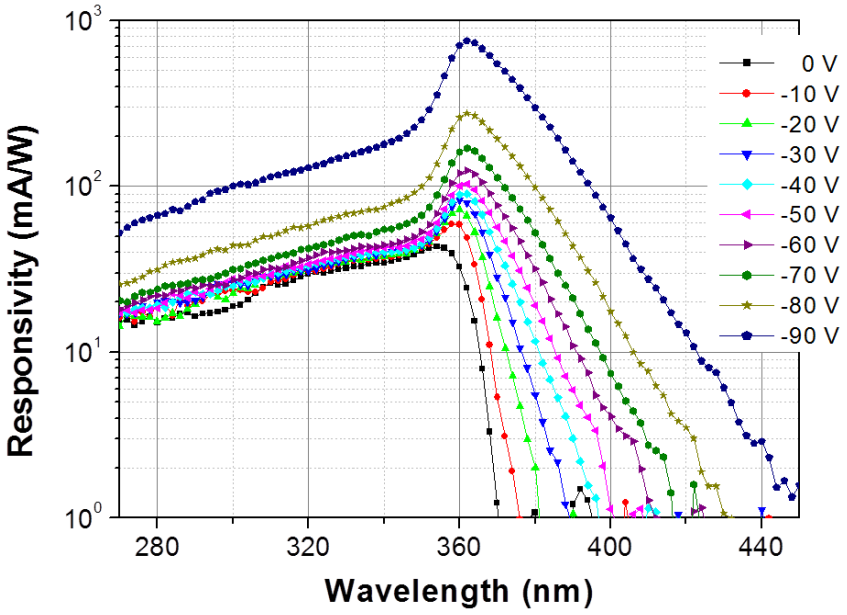

Figure 3.22 Reverse-biased voltage-dependent spectral response of photocurrent for a 70-µm-diameter (corresponding to 3,826 µm^2) $Al_{0.05}Ga_{0.95}N$ *p–i–n* UV-APD grown on a FS-GaN substrate, measured at room temperature.

3.5 Summary

In conclusion, we report on high-performance $Al_{0.05}Ga_{0.95}N$ *p–i–n* UV-APDs grown on a FS-GaN substrate with an avalanche gain higher than 5×10^5. The front-illuminated $Al_{0.05}Ga_{0.95}N$ UV-APDs grown on the FS-GaN substrate with various circular mesa from 30- to 70-μm-diameter showed low dark-current density and constant avalanche breakdown by using a step-graded *n*-type $Al_xGa_{1-x}N$:Si (x=0 and 0.02) layer instead of an *n*-$Al_{0.05}Ga_{0.95}N$:Si layer, while premature microplasma breakdown was frequently observed during the characterization of UV-APDs grown on the GaN/sapphire template. In addition, the avalanche gain of the $Al_{0.05}Ga_{0.95}N$ UV-APD grown on the FS-

GaN substrate was over an order of magnitude higher than that of comparable UV-APDs grown on the GaN/sapphire template. Moreover, a significantly improved photoresponse was observed at a reverse bias higher than 90 V, indicating the contributions of a strong avalanche multiplication process. We believe that the reduced dislocation density in the active layer of $Al_{0.05}Ga_{0.95}N$ UV-APDs grown on the FS-GaN substrate is the dominant origin of the low dark-current density and suppressed microplasma breakdown of $Al_{0.05}Ga_{0.95}N$ *p-i-n* UV-APDs, resulting in the significant improvement of device performance and reliability.

CHAPTER 4. DEMONSTRATION OF III-N ULTRAVIOLET AVALANCHE PHOTODIODE ARRAYS WITH LARGE DETECTION AREA

4.1 Introduction

As mentioned above, GaN *p-i-n* ultraviolet avalanche diode (UV-APD) arrays are well-suited for numerous applications in military systems, bio-aerosol detection, imaging systems, and space research because of the advantageous properties of III-nitride materials. In particular, to improve the collection efficiency and sensitivity for low-level light detection, several industries are promoting UV-APD arrays with a large detection area [98, 99]. The development of large-detection-area UV-APD arrays based on III-nitride materials, however, has been hampered by high dislocation densities originating from heteroepitaxy, resulting in non-uniformity in electrical properties, low yield, and high leakage current as well as the premature microplasma breakdown. Moreover, as the detection area of photodiodes increases, these issues have become more critical [67]. Therefore, achieving the high crystalline quality of epitaxial layer structures with reduced-defect densities as well as optimizing the fabrication processes such as etching and passivation techniques that reduce sidewall leakage current are key to realizing high-performance UV-APD arrays and yielding a larger detector size.

In this chapter, we report on the material growth, device fabrication, and device characterization of 4×4 GaN *p-i-n* UV-APD arrays with a large detection area of 5,625 μm^2 for a single UV-APD element grown on a free-standing (FS) GaN substrate.

4.2 Design, Epitaxial Growth, and Device Fabrication

The epitaxial growth of GaN *p*-*i*-*n* UV-APD arrays was carried out in a metalorganic chemical vapor deposition (MOCVD) reactor system equipped with a close-coupled showerhead growth chamber. The growth was performed on *n*-type Si-doped FS-GaN substrate with a threading dislocation density lower than 5×10^{6} cm^{-2} that were grown by hydride vapor phase epitaxy (HVPE). Trimethylgallium ($Ga(CH_3)_3$, TMGa) and ammonia (NH_3) were used as Groups III and V precursors, respectively. Diluted silane (SiH_4) and bis-cyclopentadienyl magnesium ($Mg(C_5H_5)_2$, Cp_2Mg) were used as *n*- and *p*-type dopant precursors, respectively. As shown in Figure 4.1, the epitaxial layer structure of the GaN *p*-*i*-*n* UV-APD arrays consisted of a 2.3-μm-thick *n*-GaN:Si layer ($n\sim4\times10^{18}$ cm^{-3}), followed by a 0.28-μm-thick unintentionally doped GaN drift region ($n\sim2\times10^{16}$ cm^{-3}), and a 0.1-μm-thick *p*-GaN:Mg layer ($p\sim1\times10^{18}$ cm^{-3}). Finally, a 15-nm-thick heavily-doped *p*-GaN:Mg^{++} layer ($[Mg]\sim1\times10^{20}$ cm^{-3}) was grown and formed an ohmic contact layer. To achieve improved crystalline quality and doping properties, the growth and doping parameters for each epitaxial layer of the GaN *p*-*i*-*n* UV-APD arrays were carefully optimized. X-ray diffraction (XRD), atomic-force microscopy (AFM), and Nomarski microscopy were used to characterize the surface morphology and crystalline quality of the epitaxial layer structure of GaN *p*-*i*-*n* UV-APD arrays on the FS-GaN substrate.

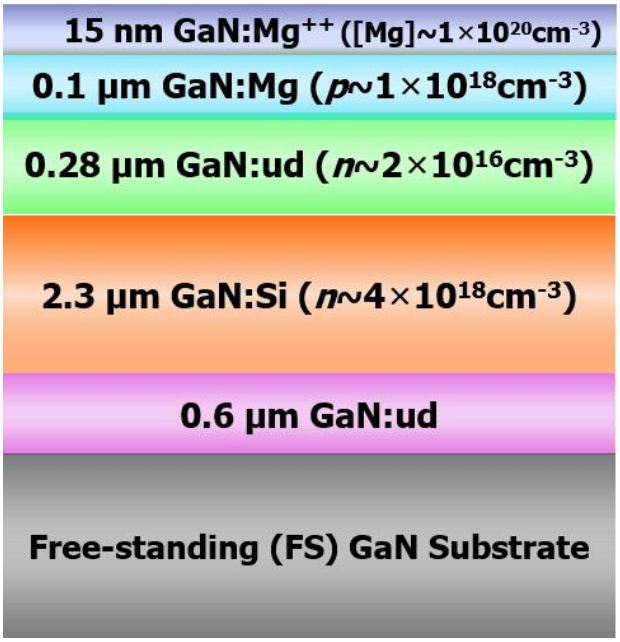

Figure 4.1 The epitaxial structure of GaN *p-i-n* UV-APD arrays grown on a free-standing (FS)-GaN substrate.

For the fabrication of top-illuminated GaN *p-i-n* UV-APD arrays, each element of the UV-APD arrays was patterned into a 75×75 μm^2 square mesa by low-damage inductively coupled plasma reactive-ion etching (ICP-RIE) using a $Cl_2/BCl_3/Ar$ carrier gas mixture. In this study, no attempt was made to fabricate tapered-mesa or double-mesa side-wall profiles that would further minimize leakage currents [100]. After mesa definition, Ti/Al/Ti/Au and Ni/Ag/Ni/Au metal stacks were deposited by electron-beam evaporation, followed by rapid thermal annealing (RTA) under optimized conditions on *n*- and *p*-type layers, respectively. A SiO_2 passivation layer was deposited on the UV-APD arrays using plasma-enhanced chemical vapor deposition (PECVD). This layer was selectively removed by subsequent ICP-RIE etching for accessing via holes. The passivation layer is indispensable for UV-APD arrays because it reduces the leakage

current through the mesa side-walls and prevents devices from undergoing premature breakdown under reverse bias. Finally, thick Ti/Au metal stacks were evaporated, forming interconnects and wire-bonding pads.

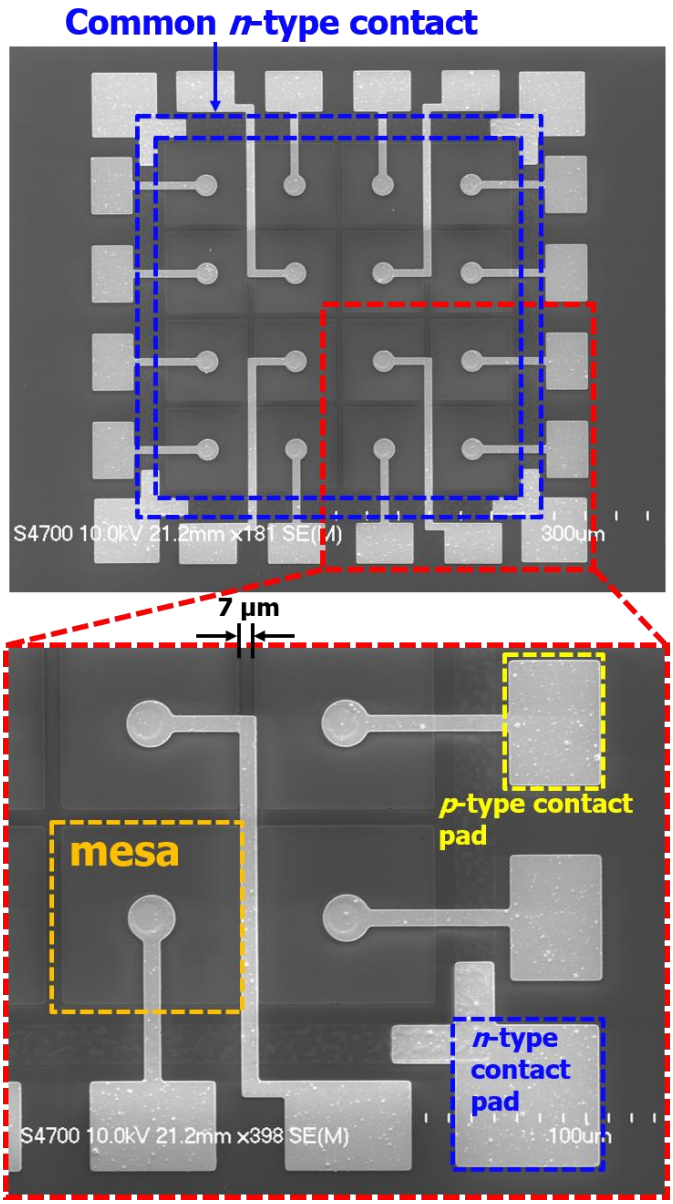

Figure 4.2 Top-view of the SEM image of a 4×4 GaN *p-i-n* UV-APD array with a mesa size of 75×75 μm^2 grown on a FS-GaN substrate.

Figure 4.2 shows a top-view SEM image of the fabricated front-illuminated 4×4 GaN *p*-*i*-*n* UV-APD array. The GaN *p*-*i*-*n* UV-APD array consisted of 16 individual GaN UV-APDs, four square wire-bonding pads for *n*-type contacts at each corner connected to a common *n*-type contact around the periphery of the UV-APD array, and 16 rectangular wire-bonding pads for *p*-type contact layers along each side of the UV-APD array. The gap between adjacent UV-APDs was 7 μm.

To investigate the electrical properties of the *n*- and *p*-type layers, the transmission line measurements (TLM) were used for *n*-GaN and *p*-GaN layers. In the TLM measurement results of both *n*- and *p*-type layers, the measured *I*-*V* curves showed a good linearity without a noticeable Schottky barrier, indicating that the contacts between the metal pads and the semiconductor layer have good Ohmic characteristics. The values of the R_{sh} and R_c are 15 Ω/□ and 6.90×10^{-5} Ω-cm^2 for *n*-type contact layer, and 68K Ω/□ and 7.04×10^{-4} Ω-cm^2 for *p*-type contact layer, respectively.

4.3 Device Characterization of Individual Ultraviolet Avalanche Photodiodes with a Large Detection Area

Figure 4.3 and Figure 4.4 show the reverse bias current-voltage (*I*-*V*) characteristics of individual UV-APDs simultaneously grown with UV-APD arrays and fabricated into independent devices with various mesa sizes and shapes. A Keithley Model 4200 Semiconductor Characterization System with a 150 W Oriel xenon lamp equipped with a monochromator system operating at a peak emission wavelength of

λ=280 nm was used to measure the dark current, the photocurrent, and the avalanche gain.

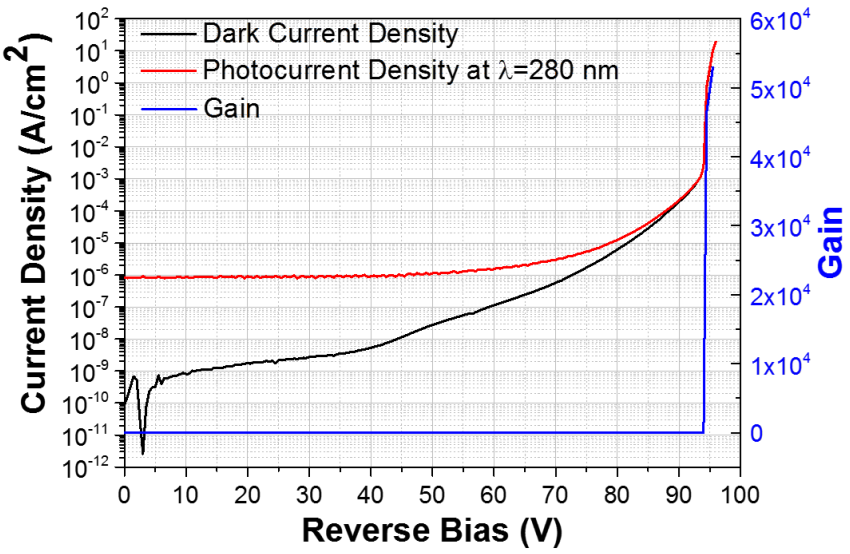

Figure 4.3 Reverse bias *I-V* characteristics of a single GaN *p-i-n* UV-APD with a large detection area of 7,850 μm^2 (a 100 μm-diameter circular mesa).

In Figure 4.3, the single UV-APD with a large detection area of 7,850 μm^2 (a 100 μm-diameter circular mesa) exhibits a very low dark current density of J_{R_Dark}<5.3×10^{-9} A/cm^2 up to a reverse bias of V_R=40 V. The dark current of the single UV-APD increased until the impact ionization effect started to impact the current flow and a reached current density of J_{R_Dark}=2.3×10^{-3} A/cm^2 at V_R=94 V, where the avalanche breakdown took place. Beyond this voltage, the dark current density increases sharply with reverse bias, suggesting active impact ionization under the high electric field in the multiplication

region. Under UV illumination at λ=280 nm, the photocurrent density is around J_{R_Photo}=1.1×10^{-6} A/cm^2 and remains constant approximately up to V_R=50 V. However, the photocurrent density increases gradually with reverse bias and then shows a sharp increase at V_R>94 V, behavior that is similar to that of the dark current density change according to reverse bias. The single UV-APD in Figure 4.3 shows an avalanche gain of around 36 at the onset point at a breakdown voltage of V_{BR}=94 V and then quickly reached an avalanche gain higher than 5.2×10^4 at V_{BR}>95.5 V.

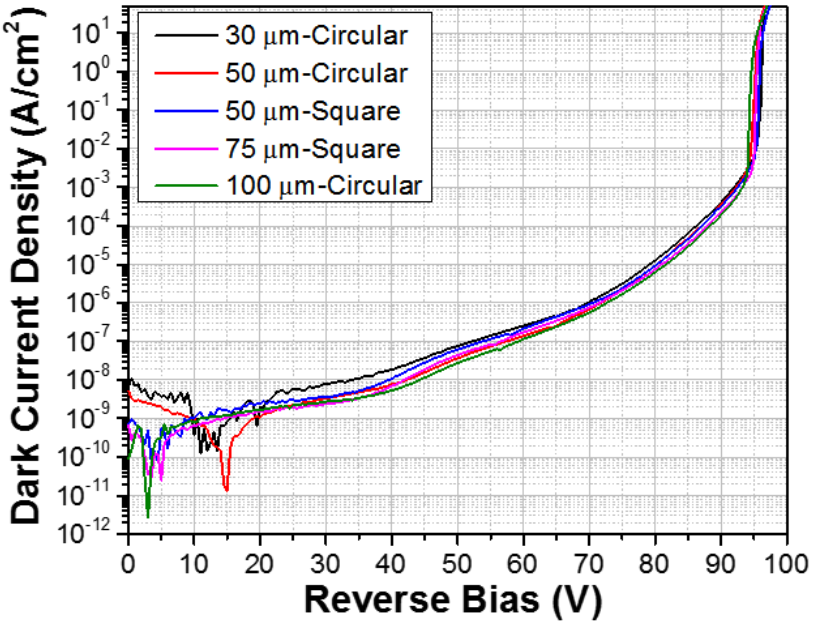

Figure 4.4 Reverse bias *I-V* characteristics of independent UV-APDs with various mesa sizes and shapes under the dark current condition.

The independent devices shown in Figure 4.4, fabricated with different mesa sizes and shapes for investigating the effect of the mesa area on device properties, exhibit almost identical reverse bias *I-V* characteristics in terms of dark leakage current and breakdown voltages. The onset points of the V_{BR} of the independent devices with various mesa sizes and shapes were in the range of onset points of V_{BR}=95.1±0.7 V.

4.4 Uniformity and Reliability of 4×4 GaN Ultraviolet Avalanche Photodiode Arrays

The uniformity of the UV-APD array, shown in Figure 4.5, was characterized by means of comparing the leakage currents of individual devices in the 4×4 GaN UV-APD array. Under the dark condition, shown in Figure 4.5 (a), the UV-APD array exhibit a uniform distribution of relatively low leakage current densities among all of the integrated UV-APDs except for two of them. The uniformity of device performance in the 4×4 GaN UV-APD array was described by means of a standard deviation. The average dark current density of the UV-APD array was lower than J_{R_Dark}=(6.5±1.8)×10^{-7} A/cm^2 at 50% of the average onset point of V_{BR}. The leakage currents of the two UV-APDs were higher than those of the other devices in the UV-APD array, possibly resulting from either the non-uniform distribution of crystalline defects in the UV-APD array or the leakage of current through the sidewall of the UV-APDs. In addition, the average onset point of the V_{BR} of the 16 devices was 95.9 V with a standard deviation of 0.6 V.

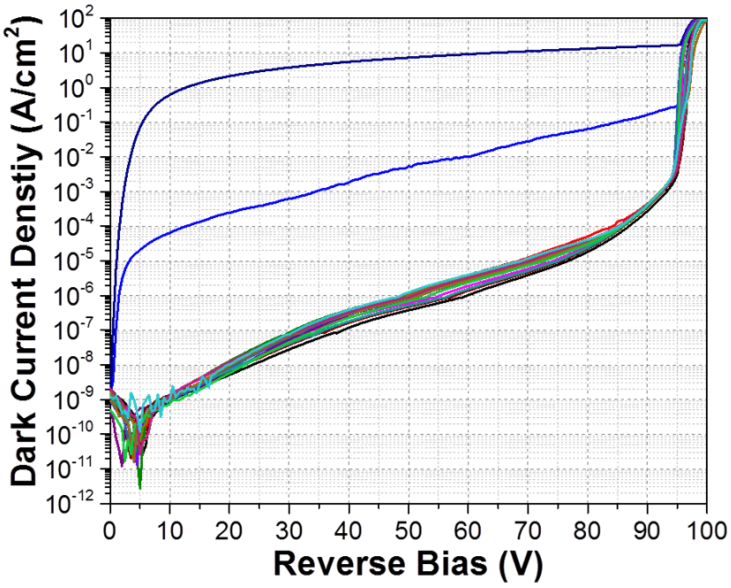

(a)

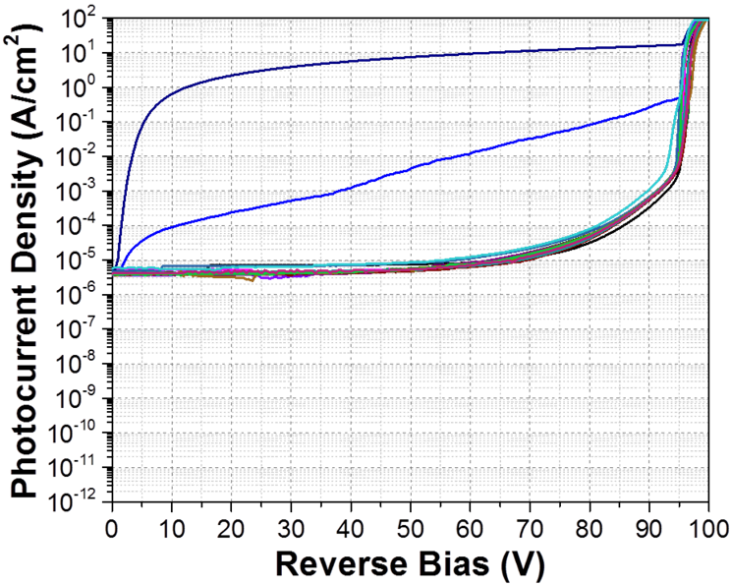

(b)

Figure 4.5 Reverse bias *I-V* characteristics of 16 devices on a 4×4 GaN *p-i-n* UV-APD array with a mesa size of 75×75 μm^2 under (a) the dark current condition and (b) UV illumination with a peak wavelength of λ=280 nm.

Under UV-light illumination with a peak wavelength of λ=280 nm, shown in Figure 4.5 (b), 14 devices in the UV-APD array exhibit uniform photocurrent distributions. The average photocurrent density was lower than J_{R_Photo}=(5.7±1.1)×10^{-6} A/cm^2 up to V_R=50V, where the photocurrent density remained flat and then gradually increased with reverse bias. The identical reverse bias *I-V* characteristics among the individual UV-APDs in the array indicate that the electrical properties of the UV-APDs were uniform and stable despite the relatively large device area. We believe that the uniform electrical properties of the UV-APD array related to the low-defect-density of the epitaxial structure and the low plasma-induced etch damage during mesa formation as well as the high-quality of sidewall dielectric passivation.

In Figure 4.6, the onset points of V_{BR} and gains at the onset points of V_{BR} are plotted for each 16 individual UV-APD in the 4×4 UV-APD array. The differences of the gain and the V_{BR} properties among 16 individual UV-APDs may have originated from their slight differences in thicknesses, the doping of the multiplication layer, and/or from the non-uniform distribution of crystalline defects in the bulk substrates. Based on other reports of the uniformity of APD arrays [99, 101, 102], however, we believe that these differences between the V_{BR} performance of independent devices and that of the devices in the array are negligible, and the gain performance of UV-APDs in the array is relatively uniform as well as the distribution of dark current and the photocurrent.

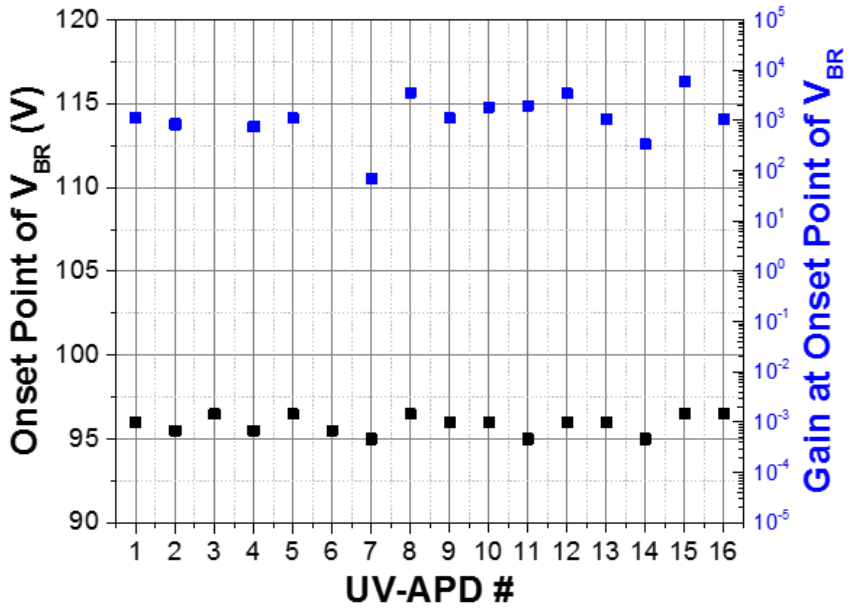

Figure 4.6 The onset points of V_{BR} and the gains at the onset points of the V_{BR} mapping of independent UV-APDs in the 4×4 UV-APD array.

In addition to the confirmation of the uniformity of the devices in the UV-APD array, multiple reverse-bias *I-V* scans were performed for the selected devices along the diagonal of the 4×4 UV-APD array, starting from the left top (#1) to the right bottom (#4), to confirm the reliability of the UV-APD array. As shown in Figure 4.7, the four devices selected in the UV-APD array show almost the same J_{R_Dark} and consistent V_{BR} after four scans of the reverse bias *I-V*. The average J_{R_Dark} before the onset point of V_{BR} was measured to be lower than $(2.6\pm0.6)\times10^{-7}$ A/cm^2 at 50% of the average onset point of $V_{BR,}$ and the V_{BR} was observed at the 96.3±0.2 V for all measured UV-APDs. The stable and reliable electrical properties of the measured UV-APDs originate from the suppressed mesa-sidewall leakage currents and the local junction breakdown. The sophisticated device fabrication process, including passivation and dry etching

techniques, and the low dislocation density of the epitaxial structure were responsible for the superior performance of the UV-APD array.

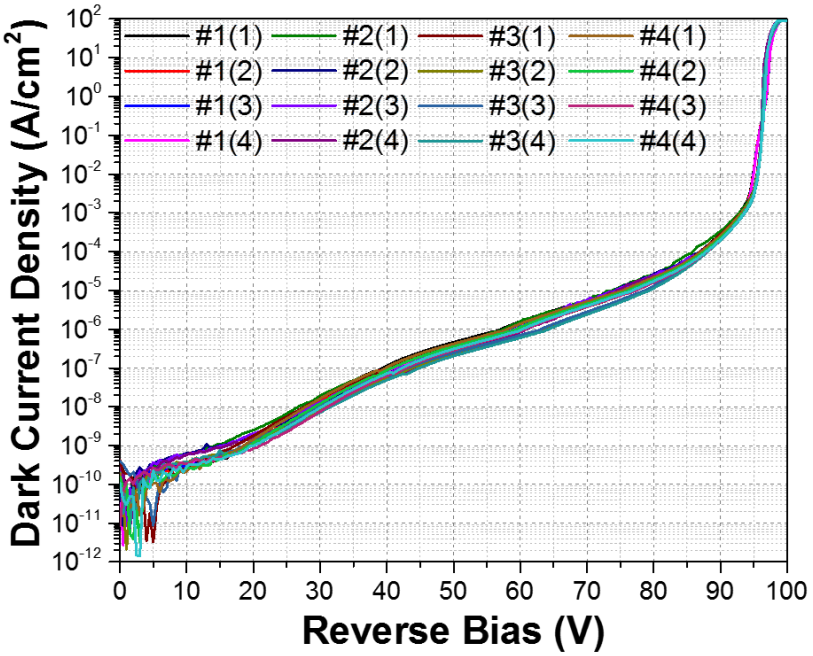

Figure 4.7 Repetition of the reverse bias *I-V* characteristics of the selected four devices in the 4×4 GaN *p-i-n* UV-APD array.

Figure 4.8 shows the bias-dependent spectral response of a selected device in the 4×4 UV-APD array. At zero bias, the measured device in the UV-APD array exhibit a peak responsivity of 142 mA/W at λ=366 nm, corresponding to an external quantum efficiency (EQE) of 48%, with an absorption edge at λ=390 nm. At a reverse bias of 90 V, however, the peak responsivity increases to 908 mA/W at λ=378 nm. The shift in the peak absorption wavelength from 366 nm to 378 nm with an increasing amplitude of the

reverse bias may have been related to the Franz-Keldysh effect [59]. In addition, the significantly broadened absorption edge into the blue band with increasing reverse bias indicated the extension of the depletion region into the doped layers as the electric field increased. The significant increase in the responsivity at a reverse bias higher than V_R=90 V was a result of carrier impact ionization as the UV-APD reached avalanche multiplication.

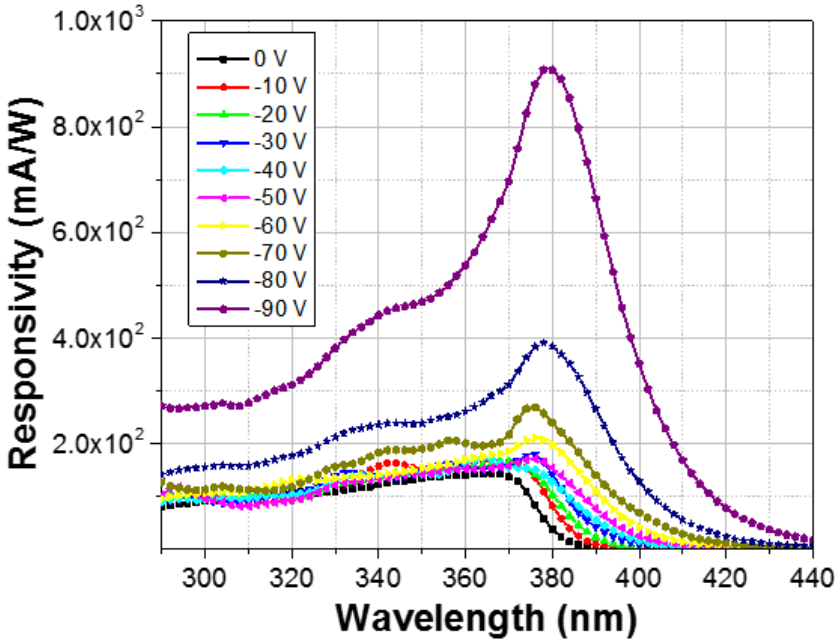

(a)

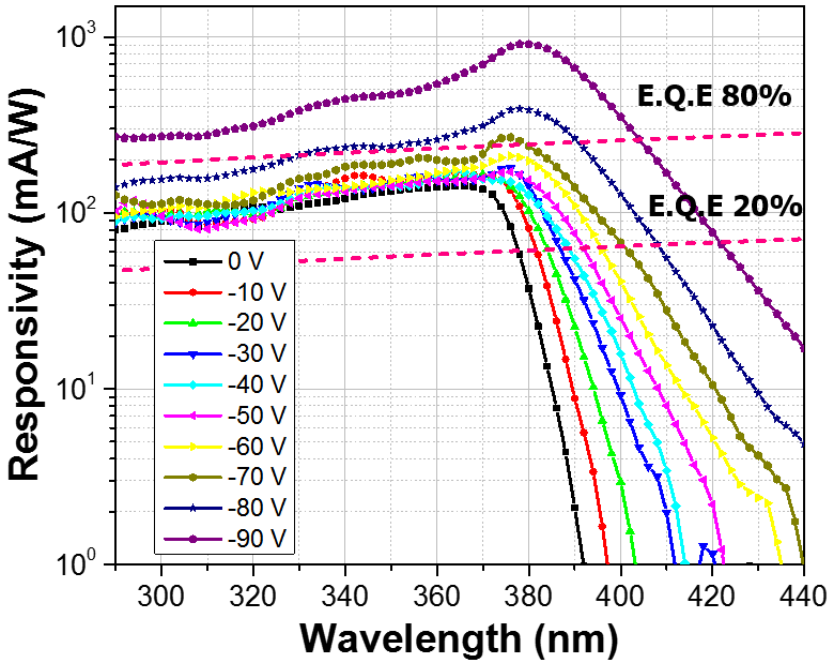

(b)

Figure 4.8 Voltage-dependent spectral response of the photocurrent for a GaN *p-i-n* UV-APD in the 4×4 UV-APD array at room temperature; (a) linear scale, and (b) log scale.

4.5 Summary

We have demonstrated 4×4 GaN *p-i-n* ultraviolet (UV) avalanche photodiodes (APDs) arrays with large detection area grown by MOCVD on the free-standing (FS) GaN substrates with a dislocation density lower than 5×10^{6} cm^{-2}. Optimized growth and doping parameters of the epitaxial *p-i-n* structure and a sophisticated UV-APD array fabrication process were applied to minimize both bulk and surface leakage currents, resulting in improved device performance and reliability. The onset points of avalanche

breakdown voltages of 16 devices in a UV-APD array were observed at a reverse bias of V_R=95.9±0.6 V without premature junction breakdown or microplasma formation. In addition, the UV-APD array showed a relatively uniform and stable leakage current distribution among UV-APDs; the dark leakage current densities were below $(6.5\pm1.8)\times10^{-7}$A/cm^2 at the V_R = 48 V which was 50 % of the average onset point of V_{BR} for all devices in the UV-APD array. Moreover, the reliable device performance of the devices in the UV-APD array was confirmed by multiple reverse-bias *I*-*V* scans. The spectral responsivity of a selected UV-APD significantly increased to 5,485 mA/W at λ = 378 nm at V_{BR} = 95 V for which the avalanche gain was higher than 5×10^4, indicating that strong carrier impact ionization was occurring in the GaN UV-APD with a large detection area.

CHAPTER 5. DEMONSTRATION OF P-I-P-I-N SEPARATE ABSORPTION AND MULTIPLICATION ULTRAVIOLET AVALANCHE PHOTODIODES

5.1 Introduction

As described above, wide-bandgap III-nitride-based avalanche photodiodes (APDs) are promising candidates for optical detection in the ultraviolet (UV) spectral region because of their potential capabilities of low dark-current density, large optical gain, small size, and low operating voltage as well as the possibility of Geiger-mode operation [60] [103][104]. In addition, III-nitride materials provide an intrinsic adjustable detection capability by controlling the bandgap energy and have excellent structural, chemical, and thermal stability suitable for harsh environments. Compared to photomultiplier tubes (PMTs), which are bulky and fragile, and Si-based photodiodes, which require optical filters for solar-blind detection, GaN-based UV-APDs are well suited to numerous applications in military systems, medical systems, imaging systems, and space research. However, if GaN-based UV-APDs are to be used as alternatives to PMTs and Si-based photodiodes, they require high sensitivity, large internal gain, and Geiger-mode operation with stable avalanche breakdown characteristics.

Recently, a number of studies have investigated back-illuminated GaN *p-i-n* APDs and separate absorption and multiplication (SAM) APDs grown on sapphire substrates to achieve low multiplication noise and high maximum gain because of a higher hole ionization coefficient [66] [72] [76] [77]. However, the major issue for the

realization of high-performance back-illuminated GaN UV-APDs is the limitation of the availability of UV-transparent substrates. Moreover, because of strong UV-light absorption in the thick *n*-type GaN layer below the active region as well as in GaN native substrates, native substrates or thick GaN/sapphire templates with low dislocation densities cannot be used for back-illuminated UV-APDs without additional processing steps. Therefore, back-illuminated GaN UV-APDs should be grown on $Al_xGa_{1-x}N$ or AlN layers with a thin *n*-type layer on UV-transparent substrates [63] [67] [68]. However, the lattice mismatch and different thermal expansion coefficients between the substrates and the epitaxial layers create high defect densities, including threading dislocations and strain-induced defects, which cause high leakage currents and premature junction breakdown, and eventually degrades the device performance of back-illuminated UV-APDs [65].

In this chapter, we demonstrate front-illuminated GaN *p-i-p-i-n* separation absorption and multiplication (SAM) UV-APDs with large detection areas grown by metalorganic chemical vapor deposition (MOCVD) on bulk GaN substrates with low defect density while achieving superior gain properties and reducing the breakdown voltage by employing impact-ionization engineering.

5.2 Epitaxial Growth and Materials Characterization

The epitaxial growth of GaN *p-i-p-i-n* UV-APDs with separate absorption and multiplication (SAM) regions was carried out by a metalorganic chemical vapor deposition (MOCVD) reactor system equipped with a close-coupled showerhead (CCS)

growth chamber. In addition, *n*-type Si-doped bulk GaN substrates with a threading dislocation density lower than 5×10^4 cm^{-2} were used in this study. Trimethylgallium ($Ga(CH_3)_3$, TMGa), trimethylaluminum ($Al(CH_3)_3$, TMAl), and ammonia (NH_3) were used as Groups III and V precursors. Diluted silane (SiH_4) and bis-cyclopentadienyl magnesium ($Mg(C_5H_5)_2$, Cp_2Mg) were used as *n*- and *p*-type dopant precursors, respectively.

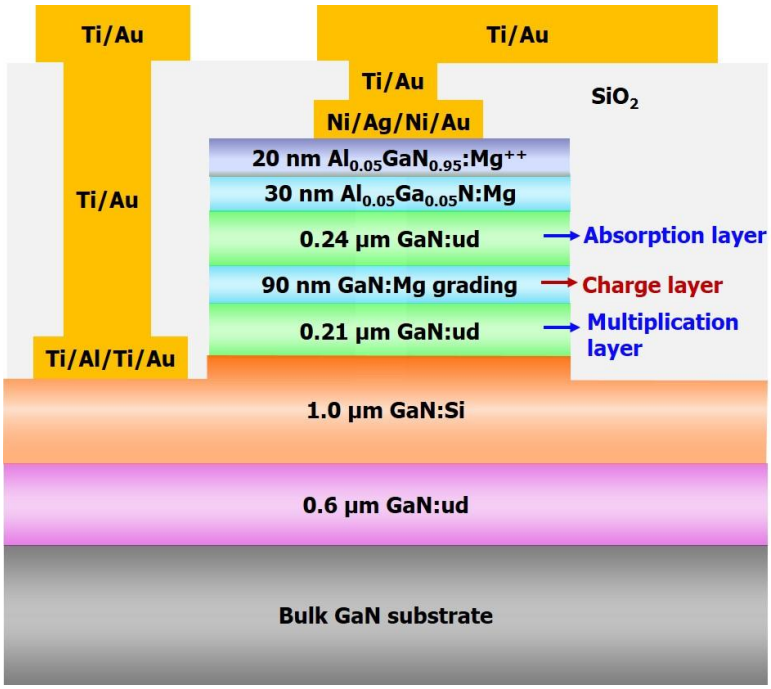

Figure 5.1 Schematic cross-sectional structure of GaN *p-i-p-i-n* SAM-APDs grown on a bulk GaN substrate.

Shown in Figure 5.1 is the schematic cross-sectional structure of the fabricated GaN *p-i-p-i-n* SAM-APDs. The epitaxial layer structure consisted of a 1.0-μm thick *n*-

GaN:Si layer (n~5.0×10^{18} cm^{-3}), a 0.21-μm thick unintentionally doped GaN multiplication layer (n~1.5×10^{16} cm^{-3}), a 90-nm thick *p*-GaN:Mg layer with graded [Mg] up to ~7.5×10^{18} cm^{-3} as the charge layer, a 0.24-μm thick unintentionally doped GaN layer as the absorption layer, which contains a gradually decreasing doping tail of [Mg] to 2.5×10^{17} cm^{-3}, a 30-nm thick *p*-$Al_{0.05}Ga_{0.95}N$:Mg layer ([Mg]~1.0×10^{19} cm^{-3}) and a 20-nm-thick heavily doped *p*-$Al_{0.05}Ga_{0.95}N$:Mg ohmic contact layer ([Mg]~1×10^{20} cm^{-3}). For a front-illuminated electron-initiated multiplication process, the *p*-$Al_{0.05}Ga_{0.95}N$:Mg layer was introduced as a window layer instead of a *p*-GaN:Mg layer to reduce the UV-light absorption in the *p*-type contact layer.

To investigate and confirm the actual doping profile and thickness of each layer, we employed secondary ion mass spectrometry (SIMS) measurement. SIMS depth profile results of Mg, Si, Ga, H, O and C for GaN *p-i-p-i-n* SAM-APDs with logarithmic scale, as function of depth from the sample surface, are shown in Figure 5.2. In addition, to examine surface morphology and crystalline quality of epitaxial layer structure, we used atomic-force microscopy (AFM), Nomarski optical microscopy, scanning electron microscopy (SEM) and X-ray diffraction (XRD). Also, Al mole fractions in $Al_xGa_{1-x}N$ epitaxial layers were determined by XRD measurement as shown in Figure 5.3.

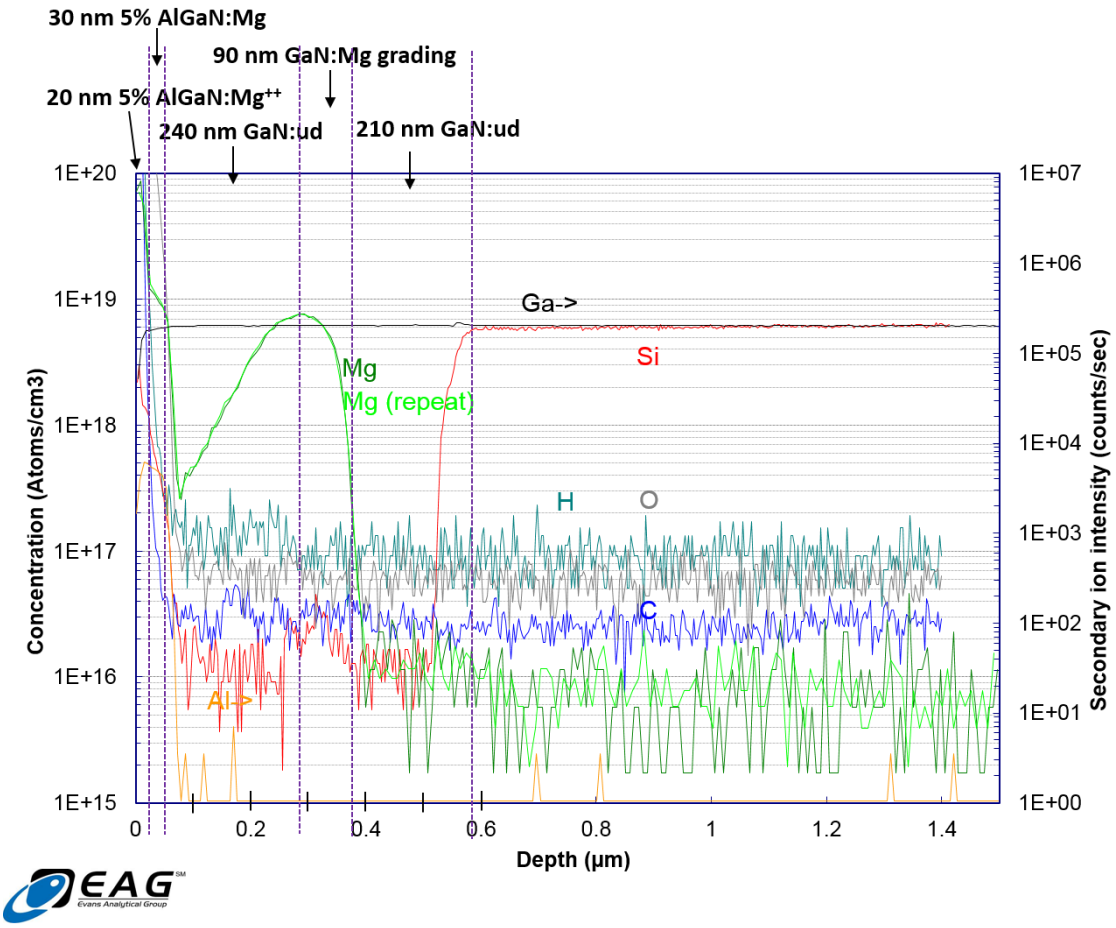

Figure 5.2 Secondary ion mass spectrometry (SIMS) distribution profiles of magnesium (Mg), silicon (Si), gallium (Ga), carbon (C), oxygen (O) for GaN *p-i-p-i-n* SAM-APD structure.

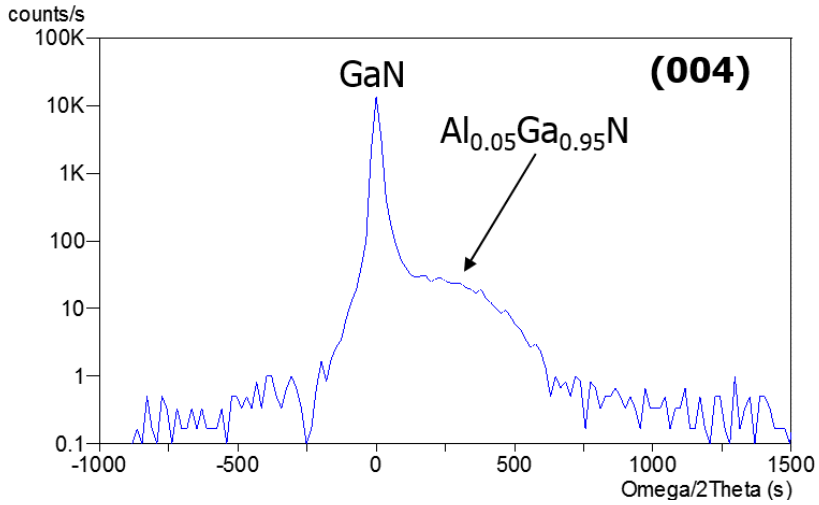

Figure 5.3 XRD ω-2θ scans GaN (004) diffraction condition of GaN *p-i-p-i-n* SAM-APDs with *p*-$Al_{0.05}Ga_{0.95}N$:Mg window layer.

In addition, to measure the electrical properties of *p*-$Al_{0.05}Ga_{0.95}N$:Mg and *n*-GaN:Si layers, we employed the Hall effect system at 300 K. Hall measurement results showed that the free-hole concentration of *p*-$Al_{0.05}Ga_{0.95}N$:Mg was p~4.9×10^{17} cm^{-3} with a mobility of μ_p~7.4 $cm^2/V\cdot s$, resulting in a resistivity of ~1.7 Ω-cm, and the free-electron concentration of the *n*-GaN:Si layer was n~5.0×10^{18} cm^{-3} with a mobility of μ_n~237 $cm^2/V\cdot s$ at room temperature.

The microscopic surface morphology of a GaN *p-i-p-i-n* SAM-APD wafer grown on the bulk GaN substrate and GaN/sapphire template. Figure 5.4 shows the microscopic surface morphology of the GaN *p-i-p-i-n* SAM-APD wafer grown on the bulk GaN substrate. The root-mean-square (RMS) surface roughness values of 1×1 μm^2 and 5×5 μm^2 scans with a height scale of 10 nm are 0.113 and 0.137 nm, respectively. Figure 5.5 shows the microscopic surface morphology of the GaN *p-i-p-i-n* SAM-APD wafer grown

on GaN/sapphire template. The RMS surface roughness values of 1×1 μm^2 and 5×5 μm^2 scans with a height scale of 10 nm are 0.197 and 0.352 nm, respectively. The GaN *p-i-p-i-n* SAM-APD wafer grown on the bulk GaN substrate reveals a smooth surface and a well-developed step-flow morphology without any visible nano-pit or dislocation-induced surface features that are observed in that grown on the GaN/sapphire template. These results indicate that the GaN *p-i-p-i-n* SAM-APDs on the bulk GaN substrate have improved the quality of crystalline.

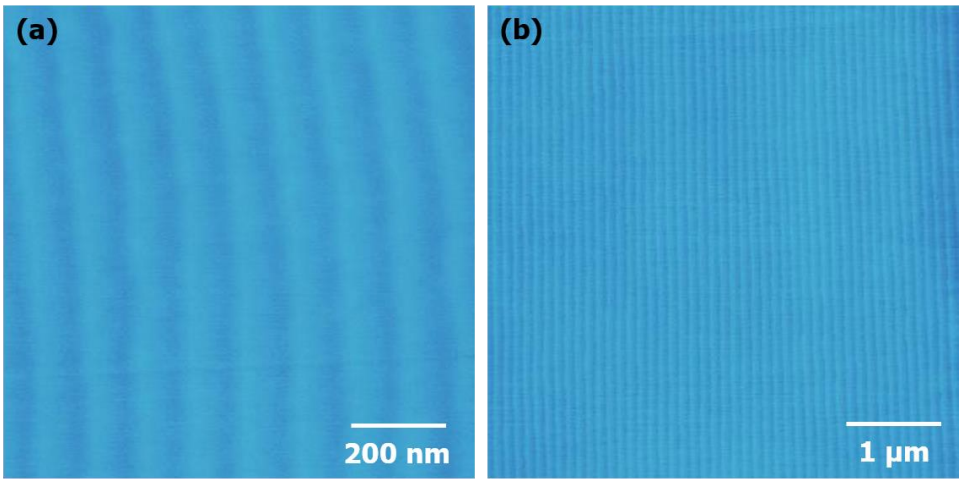

Figure 5.4 AFM microscopic surface morphology of a GaN *p-i-p-i-n* SAM-APD grown on a bulk GaN substrate: (a) with 1×1 μm^2 scan; (b) with 5×5 μm^2 scan with z-height scale of 10 nm.

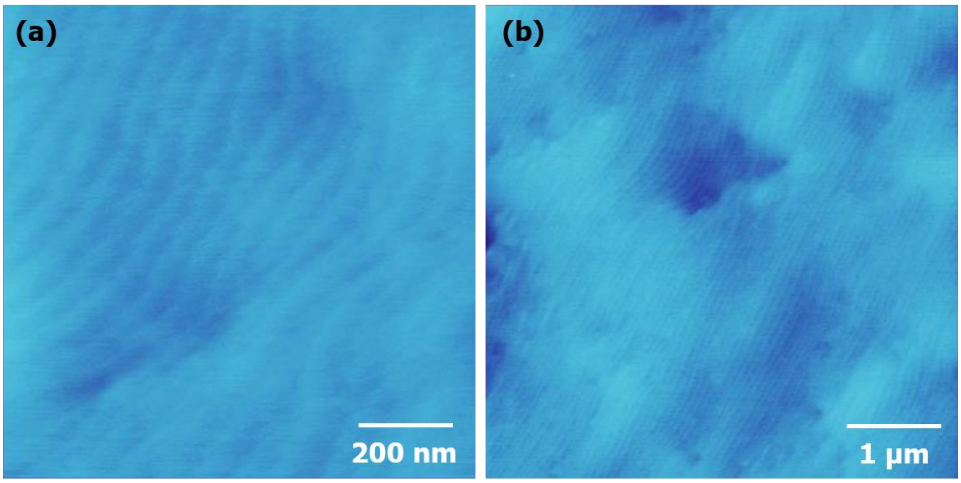

Figure 5.5 AFM microscopic surface morphology of a GaN *p-i-p-i-n* SAM-APD grown on a GaN/sapphire substrate: (a) with 1×1 μm^2 scan; (b) with 5×5 μm^2 scan with z-height scale of 10 nm.

5.3 Device Fabrication and Characterization of GaN *p-i-p-i-n* SAM-APDs

For the fabrication of front-illuminated GaN *p-i-p-i-n* SAM-APDs, the SAM-APDs were defined into various mesa sizes from 1,963 μm^2 to 10,000 μm^2 by low-damage inductively coupled plasma reactive-ion etching (ICP-RIE) in a Cl_2/He carrier gas mixture using Ni etching mask, followed by dipping into HNO_3 to remove the Ni etching mask. For *n*-type ohmic contact layer, Ti/Al/Ti/Au metal stacks were evaporated and annealed at 700 °C for 1 min under N_2 ambient. Also, for *p*-type ohmic contact layer, Ni/Ag/Ni/Au metal stacks were deposited by e-beam evaporator, followed by rapid thermal annealing (RTA) process at 500 °C for 1 min under compressed dry air (CDA). To suppress mesa-sidewall leakage current and prevent premature breakdown under high reverse bias, a SiO_2 passivation layer was applied under plasma-enhanced chemical vapor

deposition (PECVD) by accessing via holes opened by subsequent ICP-RIE etching. Finally, thick Ti/Au metal stacks were evaporated for metal interconnects and bonding pads. Neither tapered mesa nor wet-etching treatment techniques were employed in the GaN *p-i-p-i-n* SAM-APDs.

To investigate the electrical properties of the *n*- and *p*-type layers, the transmission line measurements (TLM) were employed for *n*-GaN and *p*-$Al_{0.05}Ga_{0.95}N$ layers. The current-voltage (*I-V*) measurement results of the TLM patterns are shown in Figure 5.6. In the TLM measurement results of both *n*- and *p*-type layers, the measured *I-V* curves show a good linearity without a noticeable Schottky barrier, indicating that the contacts between the metal pads and the semiconductor layer have good ohmic characteristics. The values of the R_{sh} and R_c are 30 Ω/□ and 4.02×10^{-5} Ω-cm^2 for *n*-type contact layer, and 76K Ω/□ and 2.29×10^{-3} Ω-cm^2 for *p*-type contact layer, respectively.

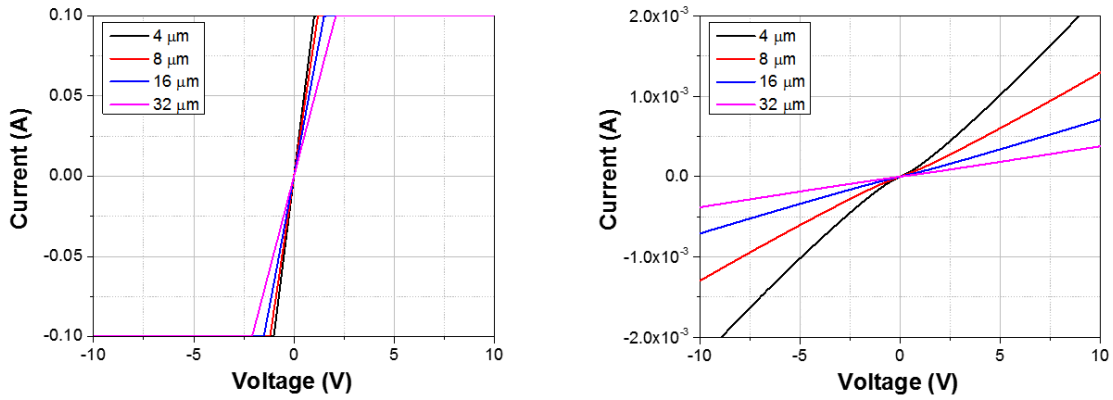

(a) *n*-TLM result (b) *p*-TLM result

Figure 5.6 Transmission line measurements (TLM) *I-V* results for (a) *n*-type GaN layer and (b) *p*-type $Al_{0.05}Ga_{0.95}N$ layer.

The calculated electric field distributions of the GaN *p-i-p-i-n* SAM-APDs at various reverse biases are shown in Figure 5.7. To conduct the simulation, Sentaurus TCAD and obtained relevant parameters used in the simulation by referring to reported papers. The polarization parameters for AlGaN materials were linearly interpolated using an online database for AlN and GaN [105], respectively. The drift-diffusion and Poisson's models were employed in the simulation. The charge layer served as a field-termination layer, which prevented further extension of the electric field from penetrating the lightly *p*-type doped absorption layer caused by the slow turn-off transient of the magnesium dopant source [106]. Moreover, the extension of the depletion region from the absorption layer is impeded by the decreased electric field in the graded *p*-type charge layer, and thus further increased the electric field in the depleted multiplication region. The maximum electric field profile in the multiplication region exceeded 3 MV/cm at the breakdown voltage (V_{BR}) of 80 V, which approximately corresponds to the reported critical breakdown electric field in GaN APDs [66].

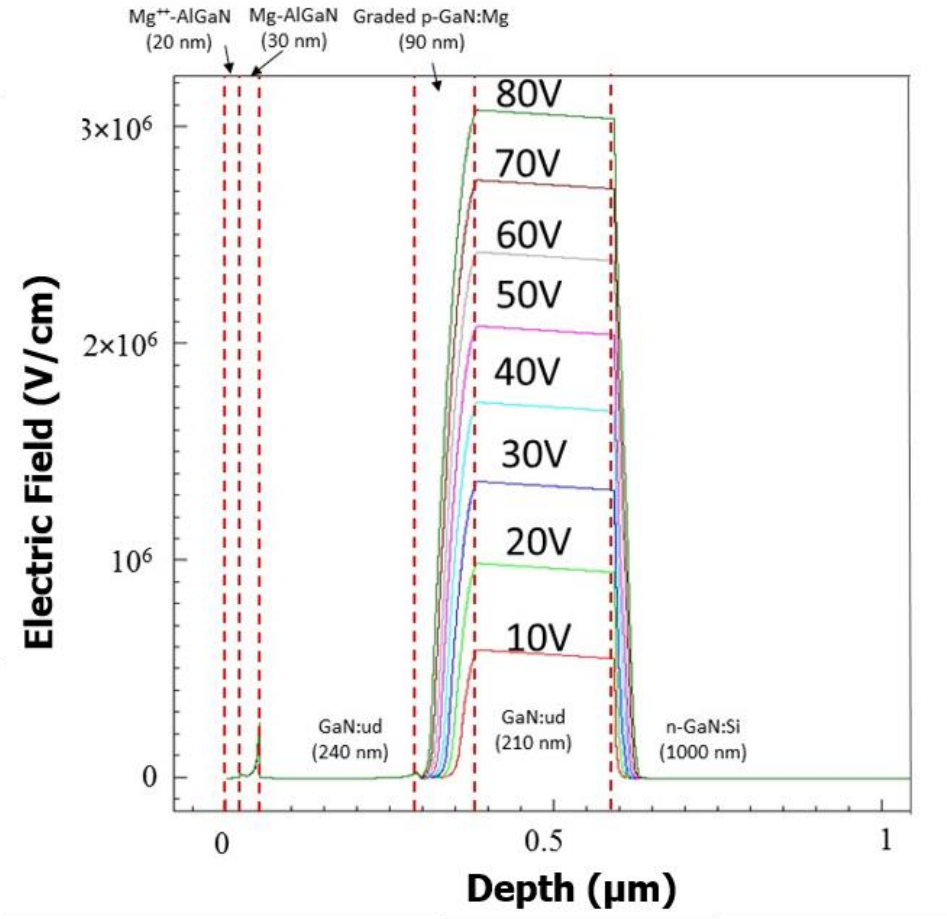

Figure 5.7 Voltage-dependent electric field distribution of a GaN *p-i-p-i-n* SAM-APD.

Figure 5.8 shows the comparison of dark current, photocurrent, gain properties between conventional GaN *p-i-n* UV-APDs and GaN *p-i-p-i-n* SAM-APDs having a mesa diameter of 30 μm on bulk GaN substrates. As shown in Figure 5.8, GaN *p-i-n* UV-APDs with *i*-layer thickness of 280 nm reveal the onset point of breakdown voltage (V_{BR}) of 89.5 V and maximum avalanche gain of 1.0×10^5 at reverse bias (V_R) of 91 V. On the other hands, GaN *p-i-p-i-n* SAM-APDs shows the onset point of V_{BR} of 73.5 V and

maximum avalanche gain of 7.4×10^6 at V_R=76 V. These results implies that GaN *p-i-p-i-n* SAM-APDs with higher gain and lower breakdown voltages are more sensitive and less possibility to lead to device failure by micro-plasma formation than conventional GaN *p-i-n* APDs.

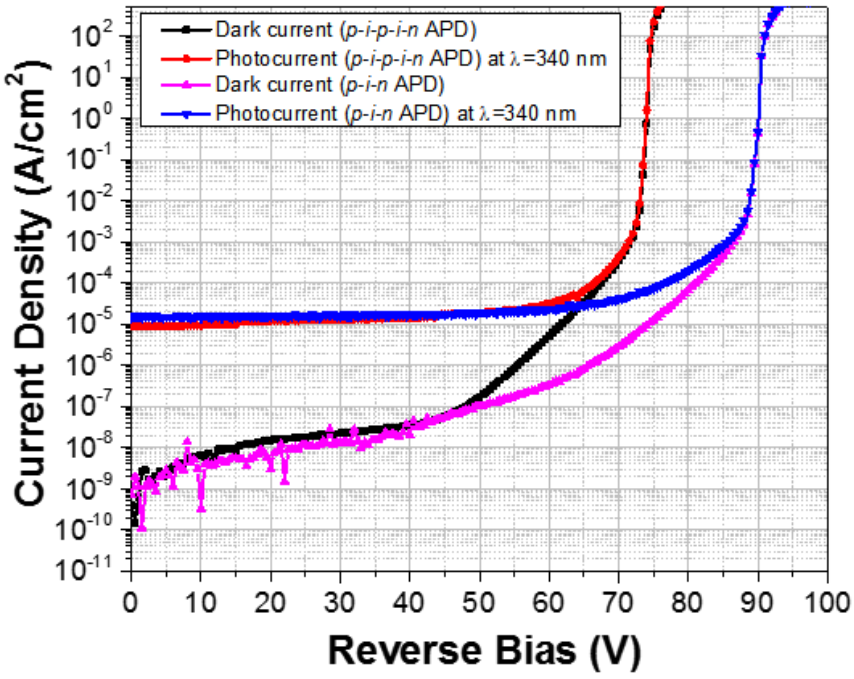

Figure 5.8 The comparison of dark current, photocurrent, gain properties between conventional GaN *p-i-n* UV-APDs and GaN *p-i-p-i-n* SAM-APDs on bulk GaN substrates.

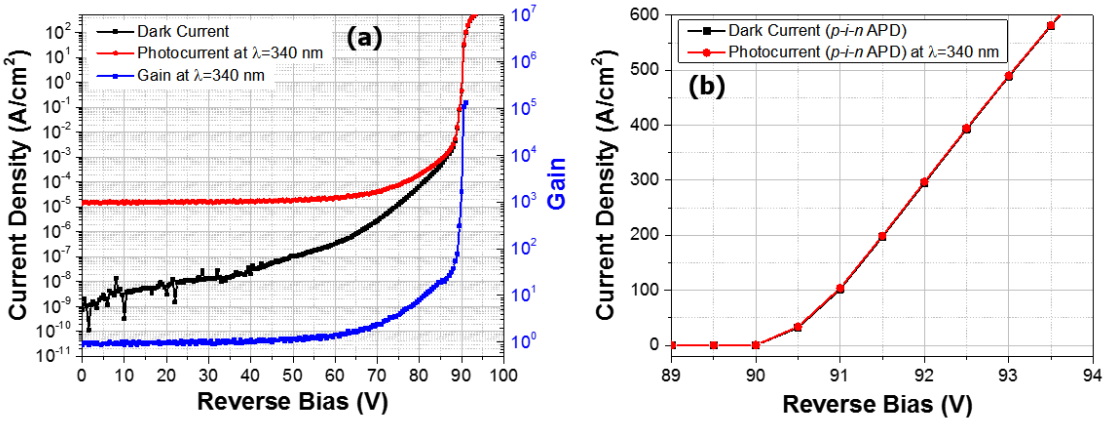

Figure 5.9 (a) Reverse-bias *I-V* characteristics of a GaN *p-i-n* UV-APD with a mesa diameter of 30 μm on bulk GaN sustarate (b) Reverse-bias *I-V* characteristics near avalanche breakdown voltage.

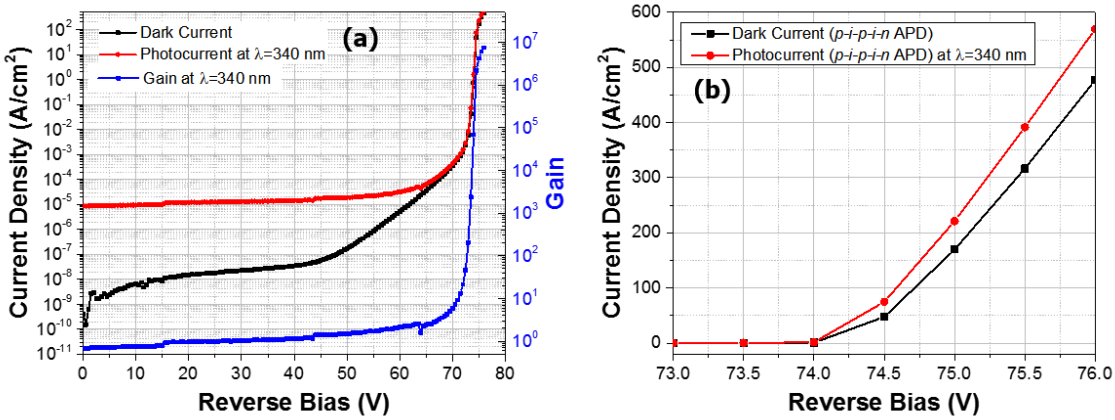

Figure 5.10 (a) Reverse-bias *I-V* characteristics of a GaN *p-i-p-i-n* SAM-APD with a mesa diameter of 30 μm on bulk GaN sustarate (b) Reverse-bias *I-V* characteristics near avalanche breakdown voltage.

The current-voltage (*I-V*) characteristics of the GaN *p-i-p-i-n* SAM-APDs were measured using a Keithley Model 4200 Semiconductor Characterization System under both dark condition and UV illumination with a peak wavelength of λ=340 nm. Figure 5.11 shows the dark-current density, the photocurrent density, and the calculated avalanche gain for the SAM-APD with a large detection area of 5,625 μm^2. Under the dark-current condition, the leakage current of the SAM-APD exhibits a very low I_R ~ 7.0×10^{-14} A that corresponds to a current density $J_{R\_Dark}<1.0\times10^{-9}$ A/cm^2 up to a reverse bias of V_R=40 V. It then monotonically increases until reaching the onset point of V_{BR}~73 V, which is ~20 V lower than that of previously reported GaN *p-i-n* APDs [59]. The values of these experimental results are in close agreement with the value of the simulated results as shown in Figure 5.7. We believe that SAM-APDs with a lower breakdown voltage offer a reduced possibility of microplasma formation, lower DC bias for single-photon detection, and lower power consumption. Beyond this voltage, a sharp increase in the dark current density is observed. This steep V_{BR} implies that the avalanche multiplication process by impact ionization in the multiplication region occurs predominantly under a high electric field, so can lead to higher photon detection efficiency. In addition, after multiple *I-V* scans, no microplasmas or premature junction breakdown from the sidewall were observed at reverse bias voltages over the onset point of V_{BR}.

Under UV illumination at λ=340 nm, the SAM-APD shows a photocurrent density of $J_{Photo}=5.6\times10^{-6}$ A/cm^2, which remains constant up to a reverse bias of V_R=50 V. As the reverse bias increases, the behavior of the photocurrent density exhibits a similar trend to that of the dark-current density. The avalanche gain is calculated by the

difference between the reverse-biased photocurrent and the dark current divided by the difference between the unity photocurrent and dark current, which is taken from the flat portion of the *I-V* curves for a reverse bias up to V_R=50 V. The avalanche gain of the SAM-APD in Figure 5.11 is 7.8×10^3 at the onset point of V_{BR} ~73 V and reaches a maximum avalanche gain higher than 5.0×10^6 at V_R=75 V. This sharp increase in the avalanche gain above the onset point of V_{BR} indicates that the SAM-APD experiences a strong avalanche multiplication process.

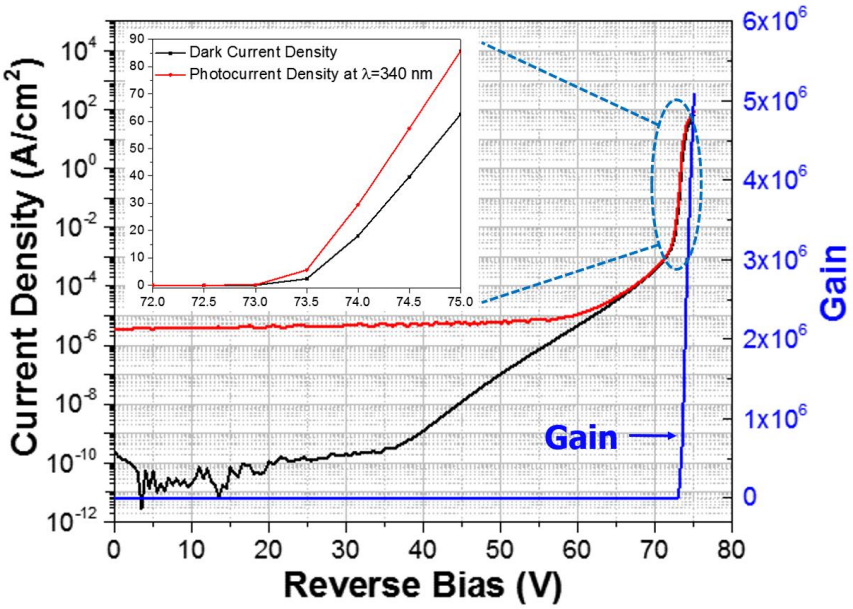

Figure 5.11 Reverse bias *I-V* characteristics of a GaN *p-i-p-i-n* SAM-APD with a mesa area of 75×75 μm² under dark condition and UV-illumination with a peak wavelength of λ=340 nm.

The comparison of the onset point of V_{BR} and the maximum gain properties of the SAM-APDs for various mesa areas from 1963 μm^2 to 10,000 μm^2 are shown in Figure 5.12. The onset points of the V_{BR} of the SAM-APDs with the mesa areas are almost the same in the range between 72.5 V and 73 V. Even though the maximum avalanche gains of the SAM-APDs slightly decrease to 8.0×10^5 as the mesa areas increase to 10,000 μm^2, the maximum avalanche gains are higher than 8.0×10^5 regardless of mesa area. These results are significantly larger than those in previously published reports for GaN APDs with large detection areas, which suggests that the GaN *p-i-p-i-n* SAM-APDs are more sensitive than conventional *p-i-n* APDs [62, 65]. We believe that the uniform onset point of V_{BR} of the SAM-APDs with various large detection areas can be attributed to the homoepitaxial growth with reduced dislocation densities and defects, low etching damage, and high-quality passivation layers on the mesa sidewall. Furthermore, the increased maximum avalanche gain and the reduced V_{BR} of the SAM-APDs suggest that photo-generated electrons are transported to the multiplication region by the increased doping level of the charge layer through impact ionization engineering [107].

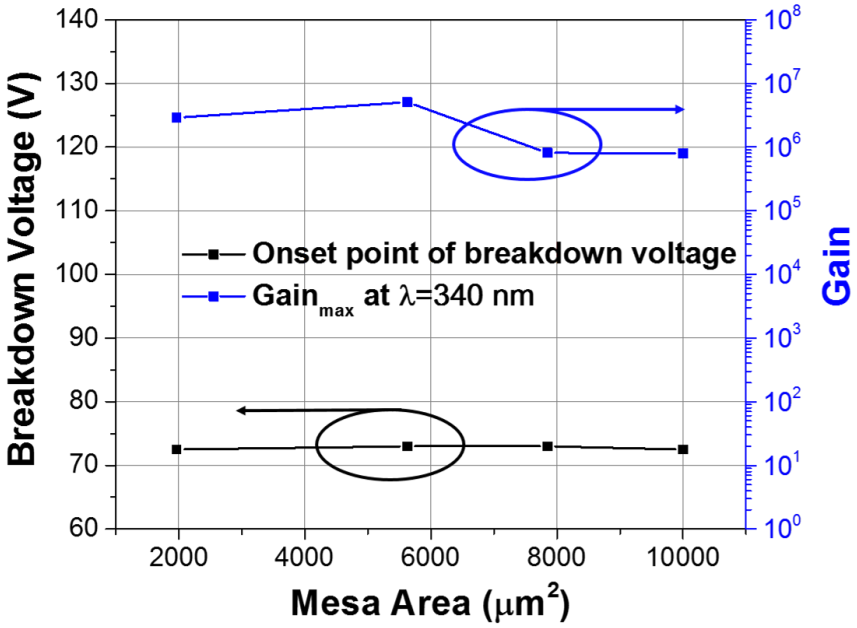

Figure 5.12 Area-dependent onset point of breakdown voltages and maximum avalanche gains.

In order to investigate the mesa size effect and verify the stability of GaN *p-i-p-i-n* SAM-APDs, multiple reverse-bias *I-V* scans of GaN *p-i-p-i-n* SAM-APDs with various mesa sizes and shapes were measured. As shown in Figure 5.13, the SAM-APDs with various mesa areas and shapes show almost identical reverse *I-V* characteristics and onset points of V_{BR}. These results indicate that the SAM-APDs are stable and reliable.

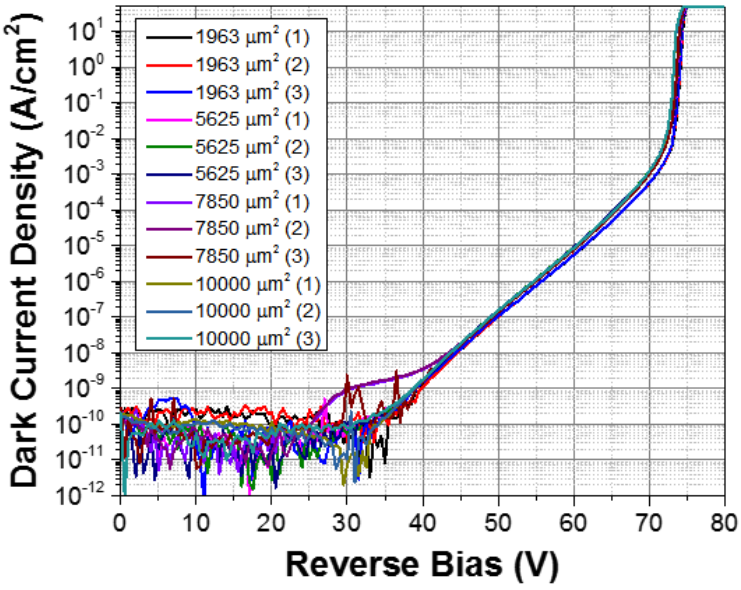

Figure 5.13 Repetition of reverse bias *I-V* characteristics of GaN *p-i-p-i-n* SAM-APDs with various mesa areas and shapes.

The bias-dependent spectral response of the GaN *p-i-p-i-n* SAM-APD with a detection mesa size of 75×75 μm^2 was measured under front illumination by an Oriel xenon lamp attached to a Cornerstone 260 monochromator/chopper system and a lock-in amplifier. The zero-biased photocurrent exhibited a peak responsivity of 42.5 mA/W at λ=366 nm, corresponding to an external quantum efficiency (EQE) of 14% with an absorption edge at 390 nm. At the reverse bias of 70 V, however, the peak responsivity increases to 320 mA/W at λ=376 nm. In addition, with increasing reverse bias, the peak absorption wavelength shifts slightly from 366 nm to 376 nm. Furthermore, compared to SAM-APDs with *p*-type GaN layer [57], the SAM-APD with the *p*-type $Al_{0.05}Ga_{0.95}N$ layer presents relatively narrower responsivity ranges within shorter wavelength regions. This finding confirms that the *p*-type $Al_{0.05}Ga_{0.95}N$ layer serves as the window layer,

resulting in a reduced UV-light in the *p*-type contact layer. Thus, it also results in more photo-generated electrons in the absorption layer. For further enhancement of the responsivity and the EQE of front-illuminated SAM-APDs, we can also use the higher-Al-composition *p*-type $Al_xGa_{1-x}N$ layer, or the thicker absorption layer.

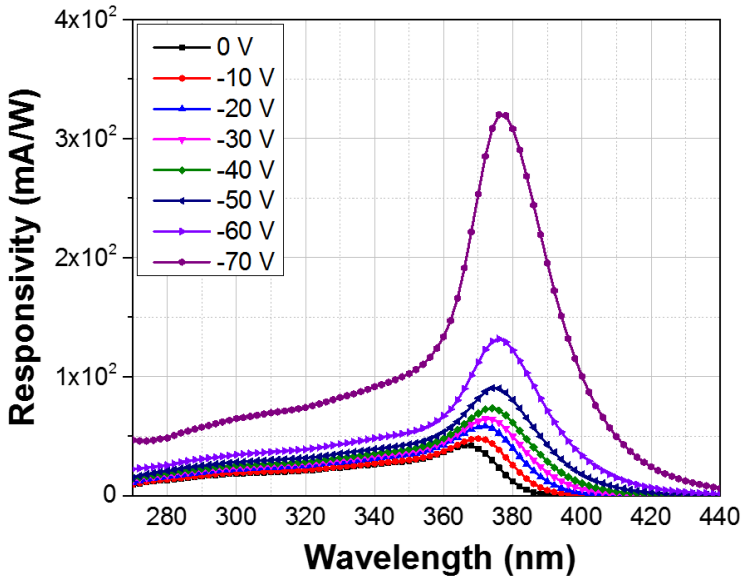

Figure 5.14 Reverse-voltage-dependent spectral response of a GaN *p-i-p-i-n* SAM-APD with a mesa area of 75×75 μm².

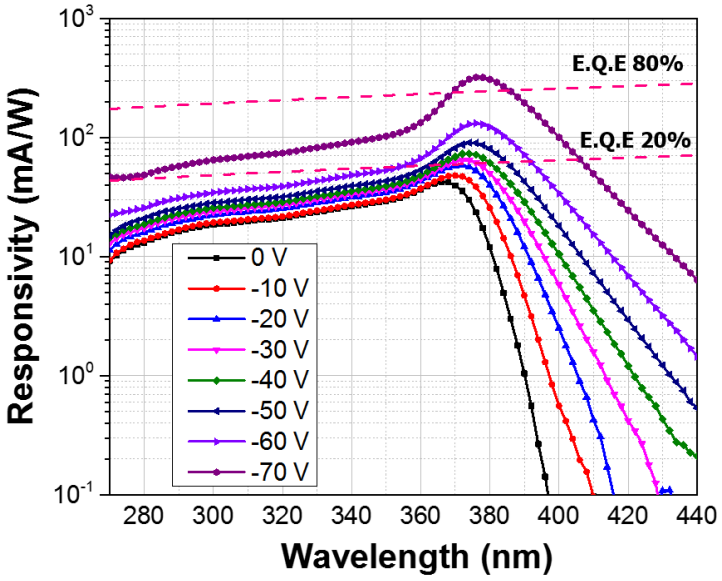

Figure 5.15 Reverse-voltage-dependent spectral response of a GaN *p-i-p-i-n* SAM-APD with a mesa area of 75×75 μm².

5.4 Summary

GaN *p-i-p-i-n* SAM UV-APDs with large detection area grown on low-dislocation-density bulk GaN substrates by MOCVD have been demonstrated. For the front-illuminated SAM-APD structures, a *p*-$Al_{0.05}Ga_{0.95}N$:Mg layer was introduced as a window layer for the reduction of the UV absorption in the *p*-type contact layer. After multiple *I-V* scans, the fabricated SAM-APDs showed stable and low leakage current density J_{R_Dark}<1.0×10^{-9}A/cm² up to the reverse bias of V_R=40 V. Under UV illumination at λ = 340 nm, the SAM-APDs exhibited large avalanche gains greater than 8.0×10^5 at a reverse bias of V_R>72.5 V regardless of mesa areas increasing to 10,000 μm². Moreover, the onset points of the V_{BR} of the SAM-APDs for all mesa areas were around 73 V. We

believe that the lower onset values of V_{BR} and the large avalanche gains of the SAM-APDs are attributed to optimized homoepitaxial growth, sophisticated fabrication processing, and the Mg-graded *p*-GaN charge layer designed by employing impact-ionization engineering.

CHAPTER 6. RESEARCH SUMMARY

For the past decade, III-nitride compound semiconductors have attracted great interest in the most promising electronics and optoelectronic devices such as light-emitting diodes (LEDs), photodiodes (PDs), and avalanche photodiodes (APDs). The large and direct bandgap of III-nitride materials, which provide high breakdown field, high electron drift velocity, and high thermal conductivity as well as structure, chemical, thermal stability, allow them to be excellent candidates for the devices operating at high temperature and in harsh environments. Moreover, because of their potential advantages of high receiver sensitivity, low noise, low dark-current densities, and high optical gain, avalanche photodiodes (APDs) based on III-N materials are useful in detecting light in the ultraviolet (UV) spectral region as replacements for photomultiplier tubes **(**PMT) or Si-based APDs and arrays. However, if these photodiodes are to be considered as replacements for PMTs or Si-based APDs and arrays in many detection applications, they need to achieve high sensitivity, high internal gain, high uniformity, fast response, and Geiger-mode operation for photon-counting applications with stable avalanche breakdown characteristics.

The improvement of high-performance $Al_{0.05}Ga_{0.95}N$ *p-i-n* UV-APDs have been described in this work. The realization of high-performance AlGaN-based UV-APDs is still challenging mainly because of difficulties in growing high-quality AlGaN layers on lattice-mismatched foreign substrates such as sapphire and SiC. The high density of crystalline defects in GaN and AlGaN layers grown by strained heteroepitaxy results in compromised performance characteristics. To address technological issues, the $Al_xGa_{1-x}N$

p-*i*-*n* UV-APDs (*x*=0-0.05) structures were epitaxially grown on a *c*-axis *n*-type free-standing (FS)-GaN substrate with reduced defect densities and GaN/sapphire template by a metalorganic chemical vapor deposition (MOCVD) system. In addition, the effect of strain management layer in *n*-type layers is reported as a way to further minimize additional crystalline defects resulting from the lattice mismatch between GaN and AlGaN. In conclusion, the $Al_{0.05}Ga_{0.95}N$ *p*-*i*-*n* UV-APDs with step-graded *n*-type $Al_xGa_{1-x}N$:Si layer grown on FS-GaN substrate showed low dark current and high avalanche gain higher than 5×10^5 at a reverse bias of V_R>94 V. Also, with multiple times reverse bias *I*-*V* scans, the $Al_{0.05}Ga_{0.95}N$ *p*-*i*-*n* UV-APDs on FS-GaN substrates exhibited stable and constant reverse biased *I*-*V* characteristics without premature microplasma breakdown that was frequently observed on the $Al_{0.05}Ga_{0.95}N$ *p*-*i*-*n* UV-APDs on GaN/sapphire template.

The uniform and reliable 4×4 GaN *p*-*i*-*n* UV-APD arrays with large detection size of 75×75 μm^2 have been discussed in this work. The UV-APD arrays with large detection area have been sought for improving collection efficiency and sensitivity. However, the issues related to high dislocation densities in the epitaxial layers grown on lattice-mismatched substrates become more critical as the detection area of photodiodes increases. In order to reduce the defect densities, the 4×4 GaN *p*-*i*-*n* UV-APD arrays were grown on *n*-type FS-GaN substrates with dislocation densities $<5\times10^6$ cm^{-2}. In order to confirm the uniformity of a 4×4 GaN *p*-*i*-*n* UV-APD arrays, the dark current and photocurrent of individual devices in the array were measured. The dark current density of the UV-APD array is below $(6.5\pm1.8)\times10^{-7}$ A/cm^2 at the reverse bias of V_R=48 V. In addition, the average onset point of breakdown voltages of 16 devices of the array is

96±0.6 V without observation of microplasmas. Furthermore, multiple reverse-bias *I-V* scans were performed for selected devices in the 4×4 GaN *p-i-n* UV-APD array to verify the reliability and stability.

The GaN *p-i-p-i-n* UV-APDs with separate absorption and multiplication (SAM) regions with large detection area have been demonstrated in this work. Recently, SAM-APD structures have been widely investigated in order to achieve the low multiplication noise and high maximum gain. A *c*-axis *n*-type bulk GaN substrate with dislocation densities < 5×10^4 cm^{-2} was used for the high-quality GaN *p-i-p-i-n* SAM-APD structure to reduce defect densities. In addition, for a front-illuminated UV-APD structure, a *p*-$Al_{0.05}Ga_{0.95}N$:Mg layer was introduced as window layer instead of a *p*-GaN:Mg layer for minimization of UV absorption in *p*-type contact layer and a Mg-graded *p*-GaN charge layer was inserted. The onset point of V_{BR} of measured SAM-APD was 73 V, which is a lower V_{BR} than the conventional *p-i-n* UV-APDs and no microplasmas were visually observed after multiple reverse-bias *I-V* scans. In addition, under illumination at λ~340 nm, the UV-APD exhibited a maximum avalanche gain > 8.0×10^5 at the reverse bias of V_R>72.5 V.

REFERENCES

[1] H. Morkoc, Handbook of Nitride Semiconductors and Devices, vol. 1, WILEY-VCH Verlag GmbH & Co. KGaA, Weinheim, ISBN: 978-3-527-40837-5; pp. 1–1311, (2008).

[2] B. M. Shi *et al.*, "Transition between wurtzite and zinc-blende GaN: An effect of deposition condition of molecular-beam epitaxy," *Appl. Phys. Lett.*, vol. 89, pp. 151921-1-151921-3, (2006).

[3] S. V. Novikov *et al.*, "Molecular beam epitaxy as a growth technique for achieving free-standing zinc-blende GaN and wurtzite $Al_xGa_{1-x}N$," *Progress in Crystal Growth and Characterization of Materials*, vol. 63, pp. 25–39, (2017).

[4] H. Morkoc *et al.*, "Large-band-gap SiC, III-V nitride, and II-VI ZnSe-based semiconductor device technologies," *J. Appl. Phys.*, vol. 76, pp.1363-1398, (1994).

[5] A. Belabbes *et al.*, "Electronic properties of polar and nonpolar InN surfaces: A quasiparticle picture," *Phys. Rev. B*, vol. 85(11), pp. 115121, (2012).

[6] W. Paszkowicz *et al.*, "Rietveld-refinement study of aluminum and gallium nitrides," *J. Alloys Compd.*, vol. 382 (1-2), pp. 100–106, (2004).

[7] I. Vurgaftman *et al.*, "Band parameters for III–V compound semiconductors and their alloys," *J. Appl. Phys.*, vol. 89, no. 11, pp. 5815-5875, (2001).

[8] P. G. Moses *et al.*, "Band bowing and band alignment in InGaN alloys," *Appl. Phys. Lett.*, vol. 96, no. 2, pp. 021908-1–3, (2010).

[9] H. M. Manasevit, "Single-Crystal Gallium Arsenide on Insulating Substrates," *Appl. Phys. Lett.* vol. 12, no. 4, pp. 156–159, (1968).

[10] R. D. Dupuis *et al.*, "High-efficiency GaAlAs/GaAs heterostructure solar cells grown by metalorganic chemical vapor deposition," *Appl. Phys. Lett.*, vol. 31, pp. 201, (1977).

[11] R. D. Dupuis *et al.*, “Room-temperature laser operation of quantum-well $Ga_{1-x}Al_xAs$-GaAs laser diodes grown by metalorganic chemical vapor deposition," *Appl. Phys. Lett.*, vol. 32, pp. 295, (1978).

[12] H. Amano *et al.*, “Metalorganic vapor phase epitaxial growth of a high quality GaN film using an AlN buffer layer,” *Appl. Phys. Lett.*, vol. 48, pp. 353-355, (1986).

[13] H. Amano *et al.*, “p-type conduction in Mg-doped GaN treated with low-energy electron beam irradiation (LEEBI),” *Jpn. J. Appl. Phys.*, vol. 28, pp. L2112, (1989).

[14] C. L. Joseph, “Advances in astronomical UV image sensors and associated technologies,” *Proc. SPIE*, vol. 2999, no. 244, pp. 244-258, (1997).

[15] M. P. Ulmer, “Requirements and design considerations of UV and x-ray detectors for astronomical purposes,” *Proc. SPIE*, vol. 2999, no. 259, pp. 259-266 (1997).

[16] P. Peter *et al.*, “Solar-blind UV region and UV detector development objectives,” *Proc. SPIE*, vol. 3629, pp. 230-248, (1999).

[17] R. D. Dupuis and J. C. Campbell, Chapter 9. Ultraviolet photodetectors based upon III-N materials, Wide Energy Bandgap Electronic Devices, Ren, F. and Zolper, J.C. (Ed.), World Scientific Publishing, Singapore, (2003).

[18] G. A. Shaw *et al.*, “Recent progress in short-range ultraviolet communication,” *Proc. SPIE*, vol. 5796, pp. 214-225, (2005).

[19] M. Razeghi *et al.*, “Semiconductor ultraviolet detectors,” *J. Appl. Phys.*, vol. 79 (10), pp. 7433-7473, (1996).

[20] C. L. Joseph *et al.*, “Advances in Astronomical UV Image Sensors and Associated Technologies,” *Proc. SPIE*, vol. 2999, pp. 244-258, (1997).

[21] Hamamatsu photonics K.K, Photomultiplier Tubes-basic and applications, Third edition, (2006).

[22] https://www.thorlabs.com/NewGroupPage9.cfm?objectgroup_id=2909.

[23] https://www.hamamatsu.com/resources/pdf/ssd/si_apd_kapd0001e.pdf (2014).

[24] A. O. Konstantinov *et al.*, "Ionization rates and critical fields in 4H silicon carbide," *Appl. Phys. Lett*, vol. 71, pp. 90, (1997).

[25] F. Yan *et al.*, "4H-SiC visible blind UV avalanche photodiode," *Electron Lett.,* vol. 35, pp. 929-930, (1999).

[26] F. Yan *et al.*, "Demonstration of the first 4H-SiC avalanche photodiodes," *Sol. Stat. Electron.*, vol. 44, pp. 341-346, (2000).

[27] B. K. Ng *et al.*, "Multiplication and Excess Noise Characteristics of Thin 4H-SiC UV Avalanche Photodiodes," *IEEE Photon. Technol. Lett.,* vol. 14, pp. 1342-1344, (2002).

[28] H.-D. Liu *et al.*, "Demonstration of Ultraviolet 6H-SiC PIN Avalanche Photodiodes," *IEEE Photon. Technol. Lett.,* vol. 18, no. 23, pp. 2508-2510, (2006).

[29] H. Liu *et al.*, "4H-SiC PIN Recessed-Window Avalanche photodiode With High Quantum Efficiency," *IEEE Photon. Technol. Lett.*, vol. 20, no. 18, (2008).

[30] X. Cai *et al.*, "4H-SiC SACM Avalanche Photodiode With Low Breakdown Voltage and High UV Detection Efficiency," *IEEE Photon. J.*, vol. 8, no. 5, (2016).

[31] S. Yang *et al.*, "High-performance 4H-SiC p-i-n Ultraviolet Photodiode With p Layer Formed by Al Implantation," *IEEE Photon. Technol. Lett.,* vol. 28, no. 11, (2016).

[32] J. C. Campbell *et al.*, "4H- and 6H- SiC Avalanche Photodiodes," *ECS Trans.*, vol. 3, no. 5, pp. 359-365, (2006).

[33] M. Khan *et al.*, "High-responsivity photoconductive ultraviolet sensors based on insulating single-crystal GaN epilayers," *Appl. Phys. Lett.,* vol. 60, pp. 2917, (1992).

[34] E. Monroy *et al.*, "Si-doped $Al_xGa_{1-x}N$ photoconductive detectors," *Semicond. Sci, Technol.,* vol. 14, pp. 685, (1999).

[35] B. Lim *et al.*, "High responsivity intrinsic photoconductors based on $Al_xGa_{1-x}N$," *Appl. Phys. Lett* 68, pp. 3761, (1996).

[36] M. T. Hirsch *et al.*, "Persistent photoconductivity in n-type GaN," *Appl. Phys. Lett.*, vol. 71, no. 8, pp.1098-1100, (1997).

[37] H. M. Chen *et al.*, "Persistent photoconductivity in n-type GaN," *J. Appl. Phys.*, vol. 82, no. 2, pp. 899-901, (1997).

[38] C. H. Qiu *et al.*, "Deep levels and persistent photoconductivity in GaN thin films," *Appl. Phys. Lett.*, vol. 70, no. 15, pp. 1983-1985, (1997).

[39] C. Johnson *et al.*, "Metastability and persistent photoconductivity in Mg-doped p-type GaN," *Appl. Phys. Lett.*, vol. 68, no. 13, pp. 1808-1810, (1996).

[40] E. Monroy *et al.*, "$Al_xGa_{1-x}N$:Si Schottky barrier photodiodes with fast response and high detectivity," *Appl. Phys. Lett.*, vol. 73, no. 15, (1998).

[41] T. Tut *et al.*, "High bandwidth-efficiency solar blind AlGaN Schottky photodiodes with low dark current," *Solid-State Electronics*, vol. 49, pp. 117, (2005).

[42] F. Xie *et al.*, "Metal–Semiconductor–Metal Ultraviolet Avalanche Photodiode Fabricated on Bulk GaN Substrate," *IEEE Photon. Technol. Lett.,* vol. 32, no. 9, (2011).

[43] C. K. Wang *et al.*, "GaN MSM UV Photodetectors With Titanium Tungsten Transparent Electrodes," *IEEE Trans. Electron Devices*, vol. 53, pp. 38, (2006).

[44] B. Yang *et al.,* "High-performance back-illuminated solar blind AlGaN metal-semiconductor-metal photodetectors," *Electron. Lett.* vol. 36, pp. 1866, (2000).

[45] G. Wang *et al.*, "Performance comparison of front- and back-illuminated AlGaN-based metal–semiconductor–metal solar-blind ultraviolet photodetectors," *J. Vac. Sci. Technol. B*, vol. 31, pp. 011202, (2013).

[46] E. Monroy *et al.*, "AlGaN metal–semiconductor–metal photodiodes," *Appl. Phys. Lett.*, vol. 74, no. 22, pp. 3401-3403, (1999).

[47] Bahaa E. A. Saleh and Malvin Carl Teich, Chap 17 Semiconductor photon detectors, Fundamentals of Photonics, John Wiley & Sons, Inc., (1991).

[48] E. Cicek *et al.*, "Comparison of ultraviolet APDs grown on free-standing GaN and sapphire substrates," *Proc. of SPIE*, vol. 7780, pp. 77801P, (2010).

[49] A. Osinsky *et al.*, "Avalanche breakdown and breakdown luminescence in p-/splpi/-n GaN diodes," *Electron. Lett.*, vol. 34, no. 7, pp. 691-692, (1998).

[50] T. Tanaka *et al.*, "*p*-type conduction in Mg-doped GaN and $Al_{0.08}Ga_{0.92}N$ grown by metalorganic vapor phase epitaxy," *Appl. Phys. Lett.*, vol. 65, no. 5, pp. 593-594, (1994).

[51] A. Saxler *et al.*, "Aluminum gallium nitride short-period superlattices doped with magnesium," *Appl. Phys. Lett.*, Vol. 74, No. 14, pp. 2023-2025, (1999).

[52] A. Yasan *et al.*, "Characteristics of high-quality *p*-type $Al_xGa_{1-x}N$/GaN superlattices," *Appl. Phys. Lett.*, Vol. 80, No. 12, pp. 2108 2110, (2002).

[53] Peter Kozodoy *et al.*, "Polarization-enhanced Mg doping of AlGaN/GaN superlattices," *Appl. Phys. Lett.*, Vol. 75, No. 16, pp. 2444-2446, (1999).

[54] J. C. Lin *et al.*, "Low Dark Current GaN *p-i-n* Photodetectors With a Low-Temperature AlN Interlayer," *IEEE Photon, Technol. Lett.*, vol. 20, pp. 1255, (2008).

[55] P. Suvarna *et al.*, "Design and Growth of Visible-Blind and Solar-Blind III-N APDs on Sapphire Substrates," *J. Electron. Mater.*, vol. 42, pp. 854, (2013).

[56] J. Wang *et al.,* "Effect of *p*-GaN layer doping on the photoresponse of GaN-based *p-i-n* ultraviolet photodetectors," *Proc. of SPIE,* vol. 9620, pp. 96200U-1-96200U-6, (2015).

[57] J.-Y. Zheng *et al.*, "A GaN p–i–p–i–n Ultraviolet Avalanche Photodiode," *Chin. Phys. Lett.*, vol. 29, pp. 067804, (2012).

[58] D. Yoo *et al.*, "$Al_xGa_{1-x}N$ Ultraviolet Avalanche Photodiodes Grown on GaN Substrates," *IEEE Photon. Technol. Lett.,* vol. 19, pp. 1313, (2007).

[59] S.-C Shen *et al.*, "Performance of Deep Ultraviolet GaN Avalanche Photodiodes Grown by MOCVD," *IEEE Photon. Technol. Lett.,* vol. 19, pp. 1744, (2007).

[60] R. D. Dupuis *et al.*, "Growth and fabrication of high-performance GaN-based ultraviolet avalanche photodiodes," *J. Crystal Growth*, vol. 310, pp. 5217, (2008).

[61] Y. Zhang *et al.*, "Low-noise GaN ultraviolet *p-i-n* photodiodes on GaN substrates," *Appl. Phys. Lett.*, vol. 94, pp. 221109, (2009).

[62] Z. Vashaei *et al.*, "GaN avalanche photodiodes grown on m-plane freestanding GaN substrate," *Appl. Phys. Lett.*, vol. 96, pp. 201908, (2010).

[63] J. L. Pau *et al.*, "Geiger-mode operation of back-illuminated GaN avalanche photodiodes," *Appl. Phys. Lett.*, vol. 91, pp. 041104, (2007).

[64] S. Choi *et al.*, "Geiger-Mode Operation of GaN Avalanche Photodiodes Grown on GaN Substrates," *IEEE Photon. Technol. Lett.,* vol. 21, pp. 1526, (2009).

[65] E. Cicek *et al.*, "Geiger-mode operation of ultraviolet avalanche photodiodes grown on sapphire and free-standing GaN substrates," *Appl. Phys. Lett.*, vol. 96, pp. 261107, (2010).

[66] R. McClintock *et al.,* "Hole-initiated multiplication in back-illuminated GaN avalanche photodiodes," *Appl. Phys. Lett.*, vol. 90, pp. 141112, (2007).

[67] K. Minder *et al.,* "Scaling in back-illuminated GaN avalanche photodiodes," *App. Phys. Lett.,* vol. 91, pp. 073513, (2007).

[68] J. L. Pau *et al.,* "Back-illuminated separate absorption and multiplication GaN avalanche Photodiodes," *Appl. Phys. Lett.*, vol. 92, pp. 101120, (2008).

[69] C. Bayram *et al.,* "Performance enhancement of GaN ultraviolet avalanche photodiodes *p*-type δ-Doping," *Appl. Phys. Lett.*, vol. 92, pp. 241103, (2008).

[70] Y. Huang *et al.,* "Back-illuminated separate absorption and multiplication AlGaN solar-blind avalanche Photodiodes," *Appl. Phys. Lett.*, vol. 101, pp. 253516, (2012).

[71] Z. G. Shao *et al.,* "High-Gain AlGaN Solar-Blind Avalanche Photodiodes," *IEEE Elec. Dev. Lett.*, vol. 35, pp. 372, (2014).

[72] G. Yang *et al.,* "Polarization engineering of back-illuminated separate absorption and multiplication AlGaN avalanche photodiodes," *Appl. Phys. A,* vol. 122, pp. 735, (2016).

[73] P. Suvarna *et al.,* "Ion Implantation-Based Edge Termination to Improve III-N APD Reliability and Performance," *IEEE Photon. Technol. Lett.*, vol. 27, pp. 498, (2015).

[74] J. Wanyan *et al.,* "The effect of charge layer separating absorption and multiplication on the performance of GaN avalanche photodiodes," *Solid State comm.,* vol. 189, pp. 28-31, (2014).

[75] M. Hou *et al.,* "Study of AlGaN P-I-N-I-N Solar-Blind Avalanche Photodiodes with $Al_{0.45}Ga_{0.55}N$ Multiplication Layer," *Electron. Mater. Lett.*, vol. 11, no. 6, pp. 1053-1058, (2015).

[76] I. H. Oğuzman *et al.,* "Theory of hole initiated impact ionization in bulk zincblende and wurtzite GaN," *J. Appl. Phys.,* vol. 81, pp. 7827, (1997).

[77] Z. Huang *et al.,* "AlGaN Solar-Blind Avalanche Photodiodes with Enhanced Multiplication Gain Using Back-illuminated Structure," *Appl. Phys. Exp.,* vol. 6, pp. 054101, (2013).

[78] A. Krost, G. Bauer, and J. Woitok, Optical Characterization of Epitaxial Semiconductor Layers, G. Bauer and W. Richter (Eds.), pp. 287-421, Springer, Berlin, Germany, (1995).

[79] G. Binnig *et al.*, "Atomic force microscope," *Phys. Review Lett.*, vol. 56, pp. 930-933, (1986).

[80] https://www.britannica.com/technology/scanning-electron-microscope

[81] L. J. Van der Pauw, "A method of measuring specific resistivity and Hall effect of discs of arbitrary shape," *Philips Research Report*, 13: 1-9, (1958).

[82] E. H. Hall, "On a new action of the magnet on electric currents", *American J. Mathematics*, vol. 2, No. 3, pp. 287–292, (1879).

[83] Yun Zhang, "Development of III-Nitride Bipolar Devices: Avalanche Photodiodes, Laser Diodes, and Double-Heterojunction Bipolar Transistors (Doctoral dissertation)," *Georgia Institute of Technology*, Retrieved from https://smartech.gatech.edu/bitstream/handle/1853/42703/zhang_yun_201112_PhD.pdf, (2011).

[84] A. Osinsky *et al.*, "Avalanche breakdown and breakdown luminescence in p-π-n GaN diodes," *Electron. Lett.*, vol. 34, no. 7, pp. 691-692, (1998).

[85] B. Yang *et al.*, "Low dark current GaN avalanche photodiodes," *IEEE J. Quantum. Electron.*, vol. 36, pp. 1389, (2000).

[86] C. J. Eiting *et al.*, "P- and N-Type Doping of GaN and AlGaN Epitaxial Layers Grown by Metalorganic Chemical Vapor Deposition," *J. Elec. Mater.*, vol. 27, No. 4, (1998).

[87] H. Yu et al., "MOCVD growth and electrical studies of *p*-type AlGaN with Al fraction 0.35," *J. Crystal Growth*, vol. 289, pp. 419-422, (2006).

[88] M. Imura *et al.*, "Mg-doped high-quality $Al_xGa_{1-x}N$ (x=0-1) grown by high-temperature metal-organic vapor phase epitaxy," *Phys. Stat. Sol. (c)*, No. 7, pp. 2502-2505, (2007).

[89] J. B. Limb *et al.,* "GaN ultraviolet avalanche photodiodes with optical gain greater than 1000 grown on GaN substrates by metal-organic chemical vapor deposition," *Appl. Phys. Lett.,* vol. 89, pp. 011112, (2006).

[90] M. Liang *et al.*, "Low threading dislocation density in GaN films grown on patterned sapphire substrates," *J. Semicond.,* vol. 33, pp. 113002, (2012).

[91] S. Choi *et al.,* "Actual temperatures of growing surfaces of III-nitride-based materials depending on substrates and forced convection conditions in metal organic chemical vapor deposition," *J. Appl. Phys.*, vol. 106, pp.073512, (2009).

[92] J. Li *et al.*, "Optical and electrical properties of Mg-doped *p*-type $Al_xGa_{1-x}N$," *Appl. Phys. Lett.*, vol. 80, no. 7, (2002).

[93] I. Akasaki *et al.*, "Crystal growth of column-III-nitride semiconductors and their electrical and optical properties," *J. Crystal Growth,* vol. 163, pp. 86-92, (1996).

[94] M. L. Nakarmi *et al.*, "Enhanced *p*-type conduction in GaN and AlGaN by Mg-δ-doping," *Appl. Phys. Lett.,* vol. 82, no.18, (2003).

[95] J. C. Carrano *et al.*, "GaN avalanche photodiodes," *Appl. Phys. Lett.*, vol. 76, pp. 924-926, (2000).

[96] J. C. Zolper *et al.*, "A review of junction field effect transistors for high-temperature and high-power electronics," *Solid-State Electronics*, vol. 42, pp. 2153-2156, (1998).

[97] A. Nishikawa *et al.,* "High critical electric field of $Al_xGa_{1-x}N$ *p-i-n* vertical conducting diodes on *n*-SiC substrates," *Appl. Phys. Lett.,* vol. 88, pp. 173508, (2006).

[98] W. B. Liu *et al.,* "Stable multiplication gain in GaN *p-i-n* avalanche photodiodes with large device area," *J. Phys. D: Appl. Phys.,* vol. 42, pp. 015108-1, (2009).

[99] F. Yan *et al*., "Demonstration of 4H-SiC avalanche photodiodes linear array," *Solid-State Electronics*, vol. 47, pp. 241–245, (2003).

[100] H.-D. Liu *et al.,* "Demonstration of Ultraviolet 6H-SiC PIN Avalanche photodiodes," *IEEE Photon. Technol. Lett.,* vol. 18, no. 23, pp. 2508–2510, (2015).

[101] Gary A. Shaw *et al*., "Deep UV photon-counting detectors and applications," *Proc. of SPIE*, vol. 7320, (2009).

[102] X. Wu *et al*., "High Uniformity, Stability, and Reliability Large-Format InGaAs APD Arrays," *Proc. of CLEO/QELS*, (2007).

[103] S. Nikzad *et al.,* "Single Photon Counting UV Solar-Blind Detectors Using Silicon and III-Nitride Materials," *Sensors,* vol. 16, no. 927, (2016).

[104] A. Sciuto *et al.,* "Fully Planar 4H-SiC Avalanche Photodiodes With Low Breakdown Voltage," *IEEE Sensors J.*, vol. 17, no. 14, (2017).

[105] http://www.ioffe.ru/SVA/NSM/Semicond/

[106] H. Xing *et al.,* "Memory Effect and Redistribution of Mg into Sequentially Regrown GaN Layer by Metalorganic Chemical Vapor Deposition," *Jpn. J. Appl. Phys.*, vol. 42, pp. 50-53, (2003).

[107] X. Wang *et al.,* "Study of gain and photoresponse characteristics for back-illuminated separate absorption and multiplication GaN avalanche photodiodes," *J. Appl. Phys.*, vol. 115, pp. 013103, (2014).